P&E report number 2929

Experiments and Modelling of Gas-Liquid Flow in a Vertical Annulus

By

Jesil John Kurian

in partial fulfilment of the requirements for the degree of

Master of Science
in Mechanical Engineering

at the Delft University of Technology,
to be defended publicly on Tuesday November 27, 2018 at 10:00 AM.

Supervisor:	Prof. dr. ir. R. A. W. M. Henkes	
Thesis committee:	Dr. ir. M. J. Tummers,	TU Delft
	Dr. ir. B. W. van Oudheusden,	TU Delft
	Dr. ir. J. van't Westende,	TNO

This thesis is confidential and cannot be made public until December 31, 2018.

TU Delft

Abstract

The climate change agreements require large investments in renewable energies. However, with the increasing demand for energy, immediately stopping the production and use of fossil fuels is not realistic. Natural gas is twice as clean as coal and hence could be considered as a transition fuel, which can help to find a balance between the requirements of fighting climate change and producing more and cleaner energy.

The high-pressure, underground reservoirs supply natural gas which is usually wetted with liquid hydrocarbons and water. Natural gas is lifted through a production tubing to the surface, with a relatively high velocity and the drag between the gas and liquid will also bring the oil (or condensate) and water to the surface. However, over time the gas supply from the reservoirs will deplete, which gives a decreasing gas velocity, until liquid starts to fall. This is known as liquid loading, which can finally lead to the killing of the gas production. One of the solutions to operate such aging reservoirs is to reduce the cross-sectional area of the production tubing through making use of an annulus (which actually is the space in between an outer pipe and an inner pipe).

Liquid loading is noticed to occur when the flow regime changes from annular flow to churn flow. A good understanding of this multiphase flow behaviour in an anulus is desired. Therefore, this Master Thesis project was devoted to obtaining new experimental data and to develop a model for upward gas-liquid flow in a vertical annulus. Experiments with air and water were carried out in the small-scale flow loop of TNO in Delft. The air and water throughputs were varied, and both concentric and eccentric pipe-in-pipe configurations were measured. Both the pressure drop and liquid holdup were measured.

The model is able to predict the pressure gradient and holdup for a range of superficial gas and liquid velocities, using different eccentricities in the annulus configuration. The model predicted the pressure gradient within 10% of the experimental values at high superficial liquid velocities (>0.5 cm/s). However, for a superficial liquid velocity of 0.5 cm/s, the model was overpredicting the pressure drop by 100%, which could be attributed to the partial dry-out on the tube walls. To determine the superficial gas velocity, for a given pressure drop and holdup, a modified version of the Wallis correlation was used for the interfacial friction factor. The gas velocity was predicted within 5 to 10% at low holdups (< 0.075). For higher holdups the gas velocity was overpredicted by about 40%. The primary modifications made to the model for the eccentric cases are based on applying a number of grid cells in circular direction allowing for the inclusion of a closure for the variation of the circular film thickness both at the inner and at the outer pipe wall. A verification of the closure of the amplitude or of the closure of the film thickness variation is required to confirm the dependency between this parameter, the eccentricity and the holdup. However, with the applied closure of the amplitude the pressure gradient with respect to the holdup was predicted within 6% accuracy for the eccentric cases.

Acknowledgement

My Master Thesis project would not have been realized without the help and guidance of many people. First and foremost, I would like to thank Prof. R. A. W. M. Henkes for providing this opportunity and for diligently supervising me throughout the thesis tenure. The patience and wisdom he expressed in all our meetings, and finally the review of this report, was always encouraging.

I am grateful to Dr. J. van ’t Westende at TNO, who has always been a strong pillar of support. His constant counsel was immensely contributing to the progress of this thesis project. I also thank TNO and their employees, for their guidance in using their project equipment. I would also like to extend my gratitude to Dr. M. J. Tummers and Dr. B. W. van Oudheusden for kindly consenting to be part of my defence committee.

I would like to thank my friends – both nearby and abroad – for their moral support through all the hardships I had to face. Last, but not the least, the love and sacrifice of my parents and sister was integral to all the successes I have in my life, and words will not suffice to describe their care and affection for me.

Jesil John Kurian
Delft, November 2018

Contents

List of figures

Nomenclature

Roman symbols

a	Amplitude
A	Area of the annulus
A^+	Van Driest parameter (sec. 6.6.1.1)
A_c	Area of the gas core
A_f	Area of the liquid film
A_{fi}	Inner film area
A_{fo}	Outer film area
A_{yi}	Inner film area at a distance y from the wall (eq. (48))
A_{yo}	Outer film area at a distance y from the wall (eq. (45))
A_γ	A parameter for γ (eq. (19))
B_γ	A parameter for γ (eq. (19))
C_γ	A parameter for γ (eq. (19))
d	Annular radius
D	Pipe diameter
D_h	Hydraulic diameter
D_{hg}	Hydraulic diameter for the grid
D_i	Inner pipe diameter
D_o	Outer pipe diameter
D_{yi}	Diameter at distance y from the inner wall (eq. (46))
D_{yo}	Diameter at distance y from the outer wall (eq. (43))
e	Eccentricity
E	Distance between pipe centres (eq. (22))
f_1	Liquid sub-model
f_2	Gas sub-model
f_3	Full model
f_4	Superficial gas velocity function, U_{SG} (eq. (7))
f_i	Interfacial friction factor
f_{ii}	Interfacial friction factor for inner pipe
f_{iig}	Grid interfacial friction factor for inner pipe
f_{io}	Interfacial friction factor for outer pipe
f_{iog}	Grid interfacial friction factor for outer pipe
f_{iw}	Interfacial friction factor with ‘wetted-perimeter’ weighting
f_{SG}	superficial gas-phase friction factor (eq. (37))
g	Acceleration due to gravity
h	Height of the measuring station

I	Dimensionless interfacial friction factor (eq. (36))
K	Diameter ratio
K_0	Second model parameter
K_{0g}	Second model parameter for the grid
n_g	Number of grids/cells
P	Pressure
P_{bottom}	Pressure at the bottom of the measuring station
P_{top}	Pressure at the top of the measuring station
Q_G	Gas flow rate
$Q_{L,i}$	Liquid flow rate along the inner tube
$Q_{L,o}$	Liquid flow rate along the outer tube
Re_{SG}	Superficial gas-phase Reynolds number
S	Distance/perimeter along the film boundary
S_{ii}	Inner interfacial perimeter
S_{io}	Outer interfacial perimeter
S_{wi}	Inner wall perimeter
S_{wo}	Outer wall perimeter
S_{yi}	Inner film perimeter at a distance y from the wall
S_{yo}	Outer film perimeter at a distance y from the wall
T	Film thickness ratio
T_g	Film thickness ratio for the gird
u	Velocity within the film
u_{ii}	Interfacial inner film velocity
u_{io}	Interfacial outer film velocity
u^*	Friction velocity (eq. (12))
U_G	Gas velocity
U_{SG}	Superficial gas velocity
U_{SL}	Superficial liquid velocity
$U_{SL,i}$	Superficial liquid velocity for the inner film
$U_{SL,o}$	Superficial liquid velocity for the outer film
V	Liquid holdup in volume (eq. (2))
y	Distance from the tube wall
z	Axial distance

Greek symbols

α_L	Liquid holdup fraction
$\alpha_{L,i}$	Liquid holdup fraction for the inner film
$\alpha_{L,o}$	Liquid holdup fraction for the outer film

δ_f	Film thickness
δ_{fi}	Inner film thickness
δ_{fo}	Outer film thickness
δ_{vo}	Viscous length for the outer film (sec. 6.6.1.1)
γ	A modified Wallis' correlation parameter (eq. (19))
κ	Von Kármán constant (sec. 6.6.1.1)
μ_{eff}	Effective viscosity
μ_G	Dynamic viscosity of gas
μ_L	Dynamic viscosity of liquid
$\mu_{\tau o}$	Eddy viscosity for the outer film
ν_l	Kinematic viscosity of the liquid
ρ_G	Density of the gas
ρ_L	Density of the liquid
τ_i	Interfacial shear stress
τ_{ii}	Inner film interfacial shear stress
τ_{iig}	Inner film interfacial shear stress for the grid
τ_{io}	Outer film interfacial shear stress
τ_{iog}	Outer film interfacial shear stress for the grid
τ_w	Wall shear stress
τ_{wi}	Inner wall shear stress
τ_{wig}	Inner wall shear stress for the grid
τ_{wo}	Outer wall shear stress
τ_{wog}	Outer wall shear stress for the grid
τ_y	Shear stress within the liquid film at a distance y from the tube wall
τ_{yi}	τ_y for the inner film
τ_{yo}	τ_y for the outer film

Abbreviations

IPR	Inflow Performance Relation
IRENA	International Renewable Energy Agency
REmap	Renewable Energy roadmap
TPC	Tubing Performance Curve

1. Introduction

1.1. Energy and environment

“The Paris Agreement central aim is to strengthen the global response to the threat of climate change by keeping a global temperature rise this century well below 2 degrees Celsius above pre-industrial levels and to pursue efforts to limit the temperature increase even further to 1.5 degrees Celsius.” [1].

The nations that have committed to this Paris Agreement have to make an enormous effort to cut down the carbon emissions over the next few decades. The International Renewable Energy Agency (IRENA) has put forward a renewable energy roadmap (REmap) that shows a much larger contribution of renewables like wind and solar energy in the total energy mix to target lower CO_2 emissions by 2050 (Figure 1). However, a complete shift to clean energy by that time will not be feasible considering its economic consequences and the constant demand for energy. Figure 1 shows the extent to which renewable energies will possibly contribute to the energy supply while maintaining the contribution by natural gas and reducing the contributions from coal and oil. For the same amount of CO_2 emissions, natural gas can produce twice as much energy as coal can. Hence natural gas can be considered as a transition fuel which may form a good balance between the requirements of fighting climate change and providing the requested energy supply.

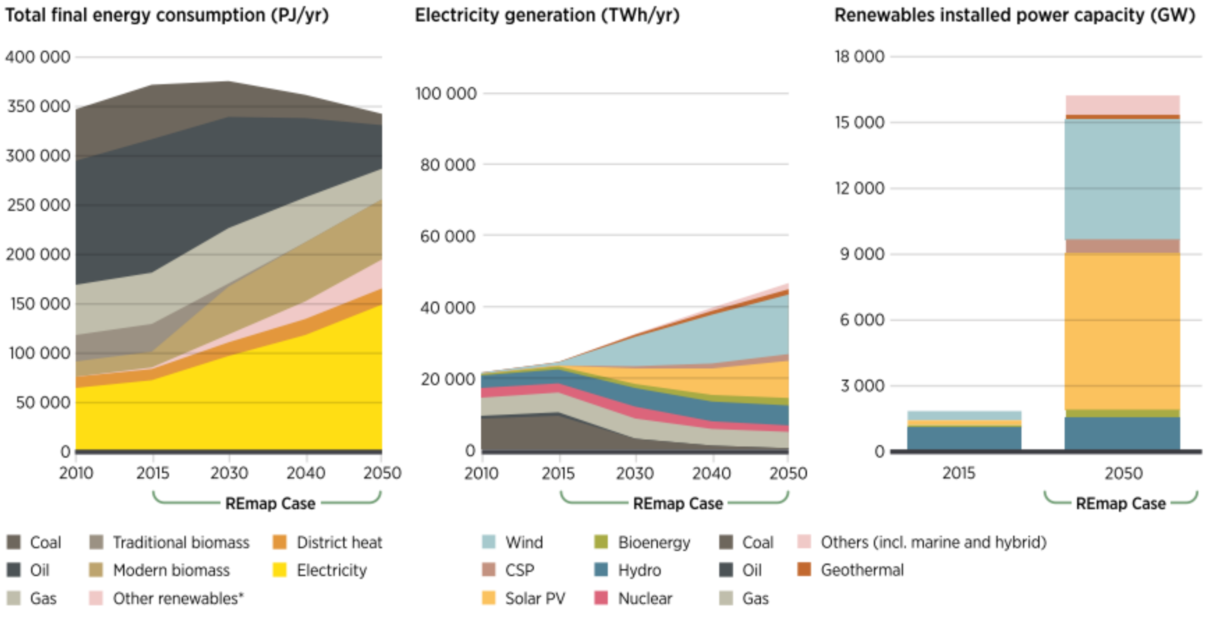

*includes solar thermal, geothermal heat and hydrogen

Figure 1: The increasing importance of electricity derived from renewable energy [32]. *Natural gas will still remain important in year 2050 to compensate for the reduction in coal and oil production.*

1.2. Natural gas

Apart from its reduced CO_2 emissions, natural gas has the below benefits when compared to other fossil fuels (i.e. oil and coal):

- Lower nitrous oxide and negligible sulphur dioxide emissions (these gases contribute to the problems of acid rain [2]).
- Can easily be stored and transported (in liquified form) and is considered to be safe.
- Ash and other particulates generated after burning are almost zero.

Despite all these advantages, natural gas production is technically challenging. The major component of natural gas is methane (70 - 90%) which has a higher GWP (greenhouse warming potential) than carbon dioxide. Therefore, leakage of the gas, even in small quantities, can outrun the benefits of the potential reduction of greenhouse gases which was targeted in the first place. Apart from this, the exploration techniques, which include usage of seismic surveys, magnetometers, logging, etc. [3], require high investments.

Natural gas is extracted from underground reservoirs under high pressures of 300-400 bar ([4], Figure 2). The reservoirs supply natural gas which is usually wetted with liquid hydrocarbons or oil seeping from the porous rocks, in addition to water which could also be produced at a later stage during extraction. Both the natural gas and its associated liquids are driven up from the reservoir to the surface through production tubings in wells.

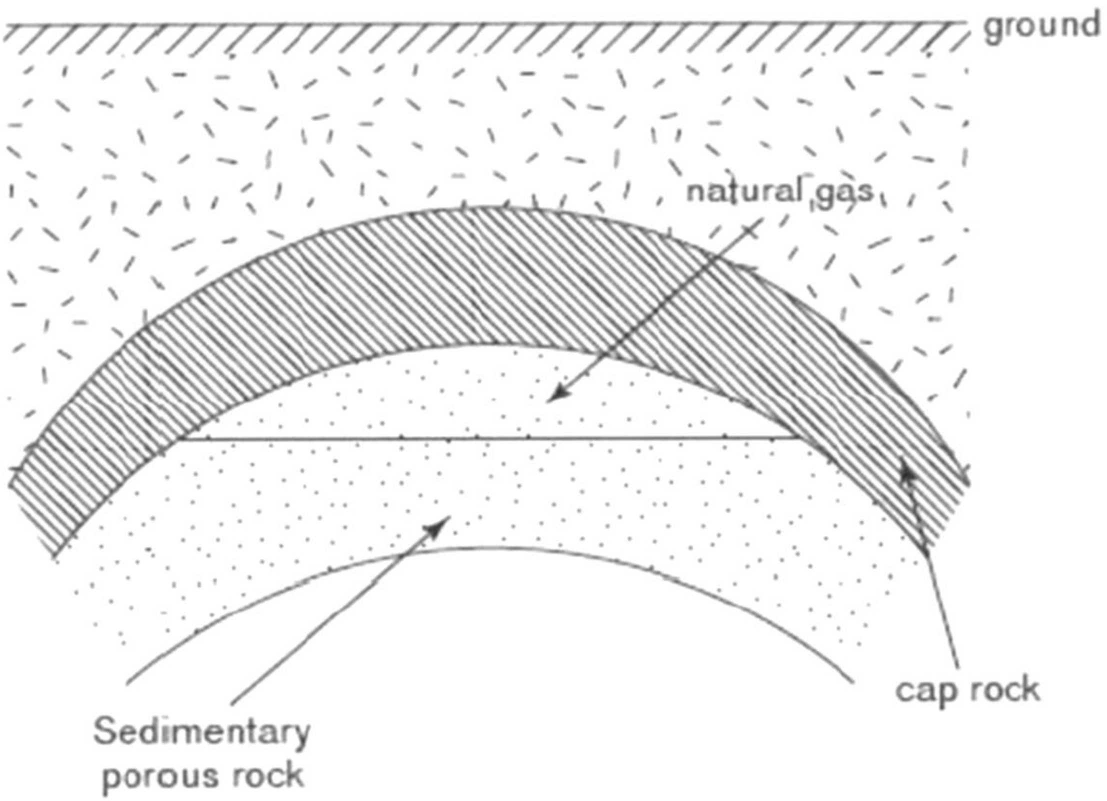

Figure 2: Natural gas reservoir. Often, the natural gas would be wetted by liquid hydrocarbons and water seeping from the porous rocks. [3]

In the early life of a reservoir, when its pressure is still high, natural gas is flowing through the production tubing with a high velocity. The drag imposed by the gas on the liquids will be sufficient to bring the condensate and water to the surface. Over time, however, the gas supply from the reservoir will deplete, due to the decreasing reservoir pressure. With the decreasing gas velocity, there is a threat of a falling liquid film, which is a phenomenon known as liquid loading (sec. 2.5). This can lead to blockage of the production tubing, which will stop the gas production. To understand this, it is useful to compare the Tubing Performance Curve (TPC)

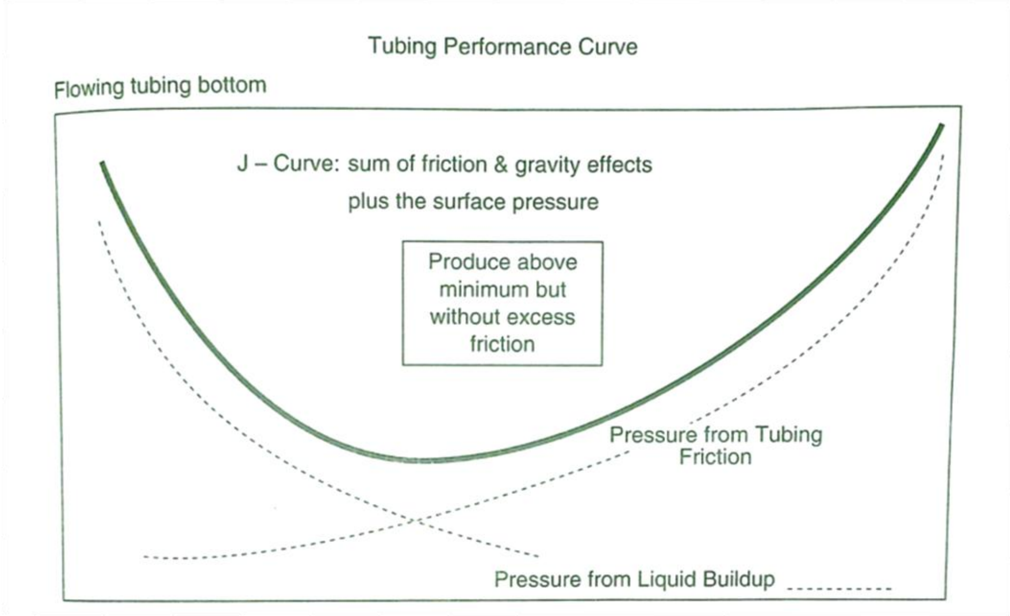

Figure 3: Standard shape of a Tubing Performance Curve (TPC) [5]*. A minimum occurs due to the different behaviours of the two contributions (namely for the hydrostatic head and for the wall friction).*

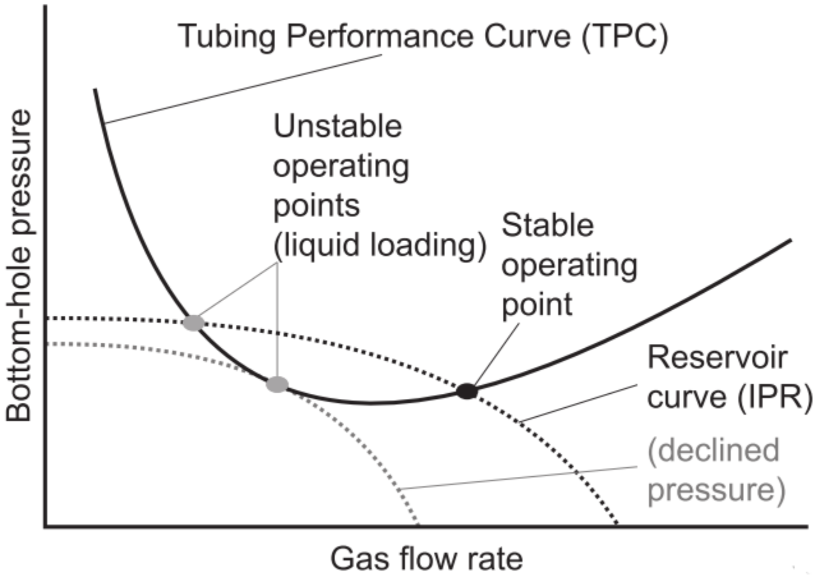

Figure 4: Schematic of the IPR and the TPC of a gas well. Both the stable and the unstable operating points are shown. Unstable operating points lead to liquid loading. [6]

with the Inflow Performance Relation (IPR). The TPC shows the combined effect of the pressure drop due to friction (tubing friction) and due to gravity (liquid build-up) against the gas flow (Figure 3). The IPR is the bottom-hole pressure against the gas flow rate, taking into account the drawdown when the fluids are transported from the reservoir (at the reservoir pressure) through the perforation to the bottom hole location in the production tubing. The operating point is determined by comparing the TPC against the IPR, as is shown in Figure 4. The stable point lies on the right side of the minimum in the TPC. If a slight perturbation is given to the unstable or metastable points, the gas flow rate would reduce leading to liquid loading [5]. The IPR marked as 'declined pressure' is the limiting case in which the reservoir pressure would have fallen far enough to give zero production.

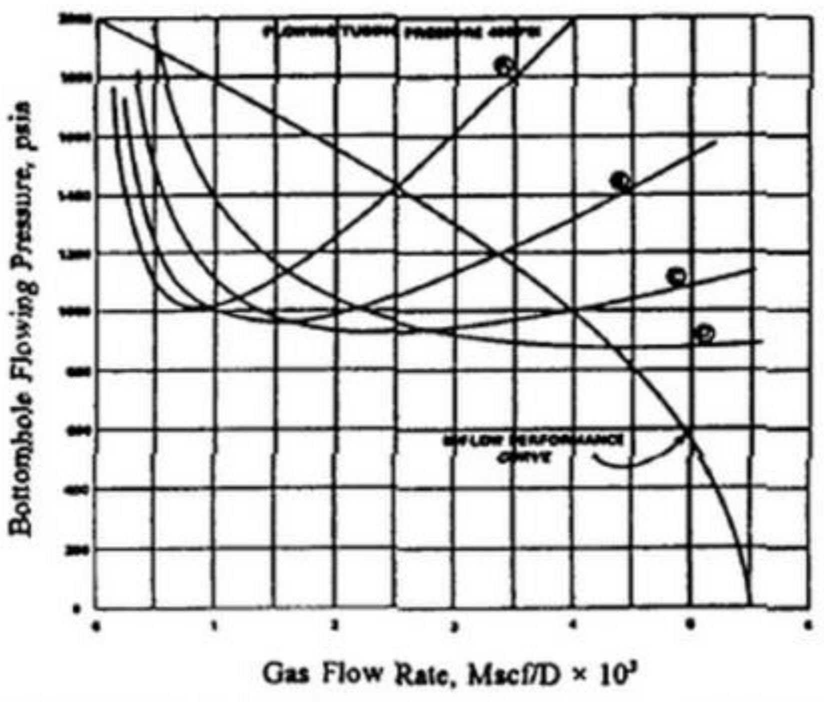

Fig. 4.19—Effect of tubing size on tubing performance curves (after Greene[36]).

Figure 5: Examples of TPCs for different tubing sizes, along with the IPR [5]. *By decreasing the flow cross-sectional area, the TPC is shifted to the left. This moves the intersection point with the IPR more towards the right of the minimum, which enhances the stability of the operating point.*

Among the different solutions, like using a surfactant [6], to operate aging reservoirs and to prevent the wells from reaching a state with liquid loading, there is an option to reduce the cross-sectional area of the extraction pipe. A reduction in the tubing size increases the pressure loss due to wall friction (Figure 3) which will move the final TPC towards the left, as is shown in Figure 5. This moves the intersection point with the IPR more towards the right of the minimum, which enhances the stability of the operating point. Instead of replacing the production tubing by one with a smaller diameter, one can also use the annulus between the production tubing and the casing of the well [7]. An annulus thus is the space between two circular pipes with different diameters, i.e. the smaller one (with ‘inner diameter’, D_i) is inserted into the larger one (with ‘outer diameter’, D_o). The cross-sectional area of the annulus would then be smaller than the outer pipe area. The superficial gas velocity (sec. 2.1) will increase with a decreased flow area, which will thus enhance the liquid transport capability of the two-phase flow.

The liquid loading point will occur at the transition from the annular flow regime (sec. 2.1) to the churn flow regime (sec. 2.3). For a proper recognition of this phenomenon in an annulus it is worthwhile to measure and model these flows.

1.3. Problem statement

The objectives of the present Master Thesis project are:

- To identify the various parameters (eccentricity, superficial gas and liquid velocities, pressure gradient, liquid holdup) characterizing the gas-liquid annular flow and churn flow regimes in an annulus.
- To incorporate the influence of these parameters in a model.
- To make a comparison of the experimental results and the model results.

1.4. Report structure

The structure of the report is depicted in Figure 6. Chapter 2 summarizes the previous research that was done on multiphase flow in annuli. Chapter 3 describes the flow loop experiment, and Chapter 4 presents a first impression of the obtained experimental results. Based on previous work, the model for concentric annulus flow will be described in Chapters 5 and 6, and the

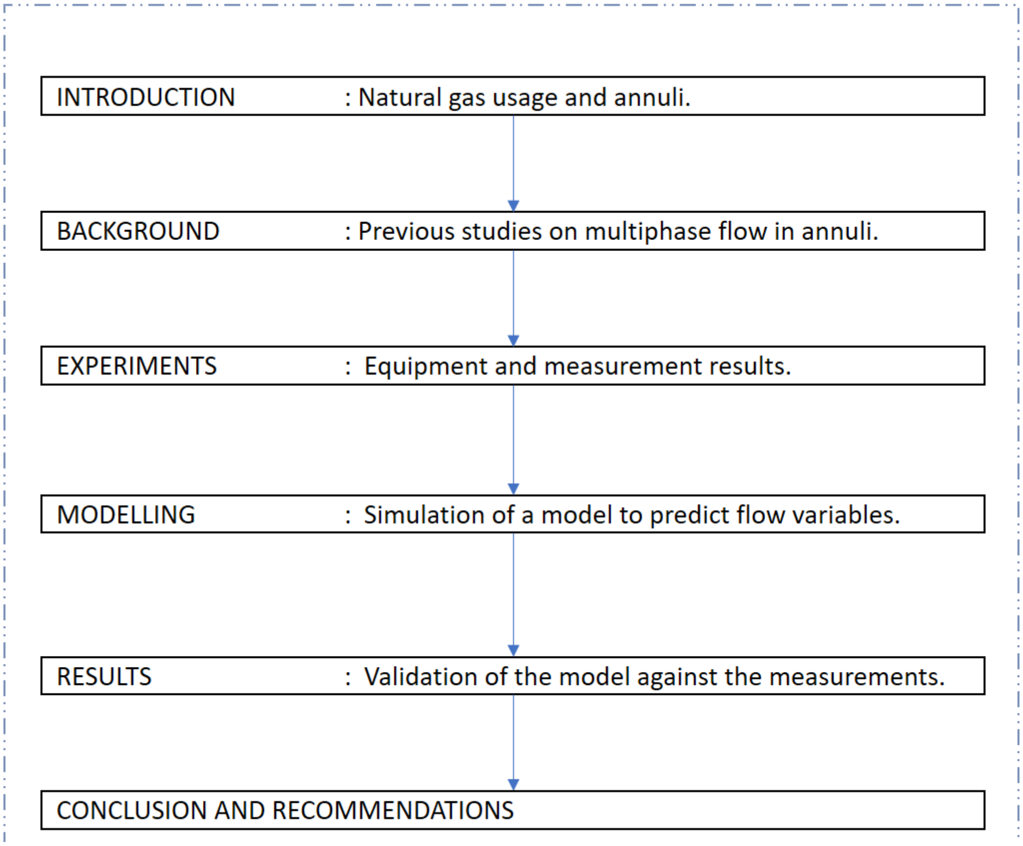

Figure 6: Flow of the report.

experimental and modelling results for that configuration are given in Chapter 7. The model for eccentric annulus flow is described in Chapter 8, and the experimental and modelling results are presented in Chapter 9. Finally, Conclusions and Recommendations will be provided in Chapter 10.

2. Multiphase flow in annuli

The two-phase gas-liquid upward flow in a vertical annulus configuration is discussed in this chapter.

2.1. Relevant terminology

The superficial velocity of a fluid is the hypothetical velocity that the fluid would have if it would have flown as a single phase along a conduit. In other words, it is the volumetric flow rate divided by the cross-sectional area of the conduit (sec. 6.2). The superficial gas velocity, U_{SG}, and the superficial liquid velocity, U_{SL}, are common terms used in multiphase flow. In the annular flow regime, the liquid films along the walls are thin, and hence the bulk of the conduit will be occupied by gas. In this flow regime, the bulk gas velocity and the superficial gas velocity will be close to each other.

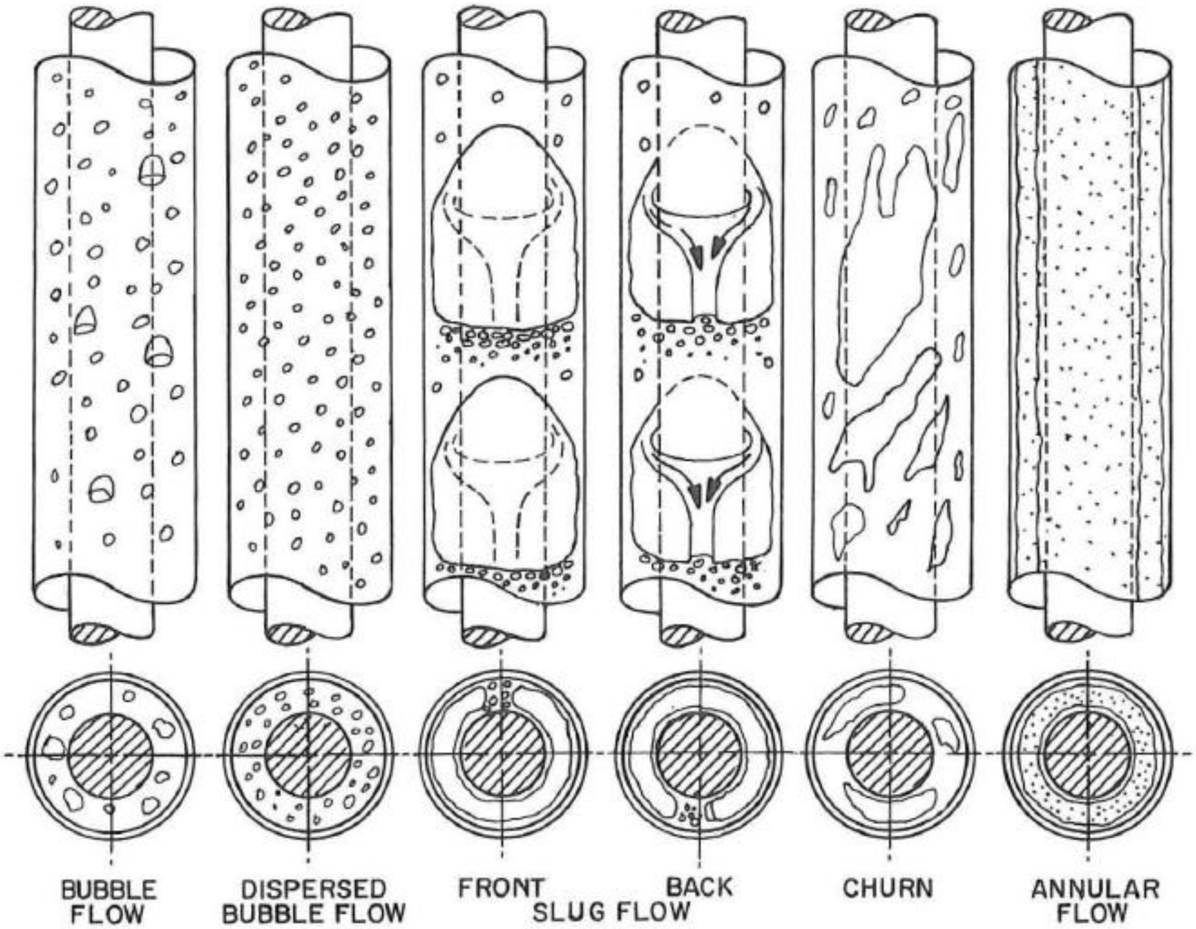

Figure 7: Flow patterns in upward vertical flow through a concentric annulus [7]. *Both the gas and liquid move upward unless indicated otherwise by the arrows in the figures.*

The annulus can have different configurations. A concentric annulus has the same centre for the inner and outer pipes. In contrast to this, for an eccentric annulus the centre of the inner pipe is different from that of the outer pipe. The liquid holdup fraction, α_L, is the fraction of the total volume in the pipe that is occupied by liquid (sec. 6.5).

2.2. Flow pattern map

The gas-liquid flow in a vertical concentric or eccentric annulus can be classified into 5 major flow patterns, namely bubble, dispersed bubble, slug, churn and annular (Figure 7, [7]). The different flow patterns depend on a number of parameters, such as the superficial gas and liquid velocities. An example of a flow pattern map for a vertical annulus is shown in Figure 8. Caetano [7] has described the characteristics of each of these flow patterns, which will be briefly summarized in the next few sub-sections.

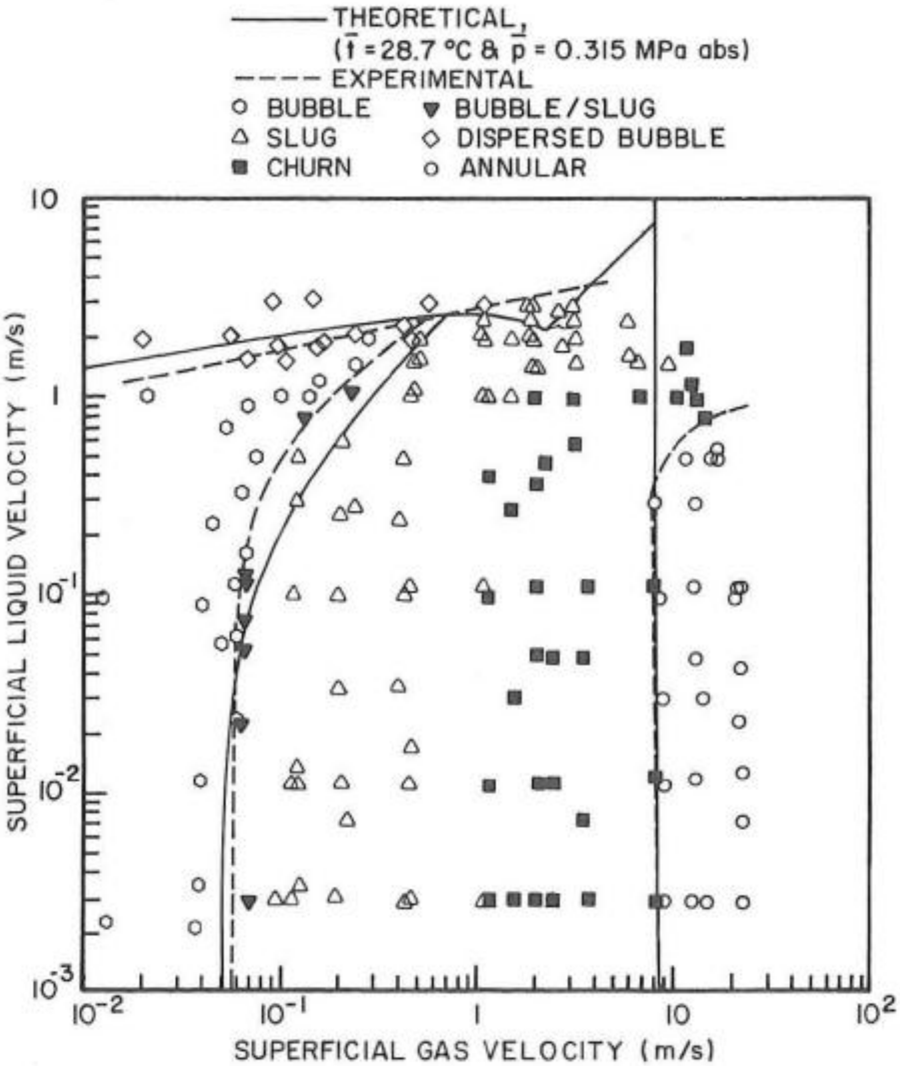

Figure 8: Flow pattern map for an air-water system for a concentric annulus [7]. *The flow pattern transitions were derived through modelling and comparison with experiments.*

2.1. Annular flow

The annular flow is a co-current gas-liquid flow in an annulus (or in a pipe) which is characterized by liquid films flowing up along the walls (annular flow in Figure 7). For an annulus, the films are formed on both the inner and the outer pipe walls. The film layers are flowing upwards with the gas. Waves can be formed at the liquid/gas interface. The gas core between the two films entrains liquid droplets which will account for the transport of a fraction of the total liquid flow. Entrainment is a process where the gas phase/core captures liquid in the form of droplets from the liquid phase/films in a gas-liquid annular flow or churn flow (sec. 2.3). Atomisation is the process of liquid getting sprayed or atomised from the films into the gas core to get entrained. Deposition is the process in which entrained liquid droplets in the core are transported back into the liquid films.

For an eccentric annulus accumulation of liquid occurs near the narrow gap. This is probably due to the locally lower gas velocities [7]. The different flow patterns for an eccentric annulus are given in Appendix F: Fully eccentric flows.

2.2. Slug flow

When the gas velocity is decreased transition to first churn flow and then to slug flow will occur. Liquid is transported upward in the form of slugs (liquid pockets) separated by Taylor bubbles (slug flow of Figure 7). There is a preferential channel or path between the top and bottom of the Taylor bubble through which the liquid flows back. Therefore, the Taylor bubble is only symmetric along one vertical plane. The channel will exist along the narrow edge for an eccentric pipe (see Appendix F: Fully eccentric flows).

2.3. Churn flow

This regime exists between annular flow and slug flow. It is characterized by the breakup of Taylor bubbles and the chaotic movement of liquid. The transition from slug flow to churn is explained by Caetano et al. [7] as follows:

> *“The Taylor bubble becomes narrow and its shape is destroyed. The continuity of the liquid in the liquid slug between successive Taylor bubbles is also repeatedly destroyed by a high local gas phase concentration. As this happens, the liquid in the slug falls backward, accumulates, forms a temporary bridge and is again lifted upward by the gas. This alternating direction for the liquid movement is a typical characteristic of churn flow. This flow pattern is also independent of the annuli configuration.”*

2.4. Bubble flow and dispersed bubble flow

The gas phase in the bubble flow regime is transported into two ways: as smaller spherical bubbles or as larger cap bubbles. The spherical ones follow a zig zag path while the cap bubbles move upward in a straight direction. For eccentric annuli, the bubbles tend to move towards the wider gap.

The dispersed bubble flow regime is found at higher superficial liquid velocities than the bubble flow regime. Dispersed bubble flow is characterized by spherical bubbles, which move in a straight upward direction. This flow pattern behaves in the same way for concentric and eccentric annuli.

2.5. Liquid loading and flooding

In the annular flow regime gas and liquid are transported co-currently. With decreasing gas velocity, the liquid films will become thicker. Below a certain ‘critical’ gas velocity, some liquid starts to fall below the liquid injection points (sec .3 and sec. 2.6) and marks the onset of liquid

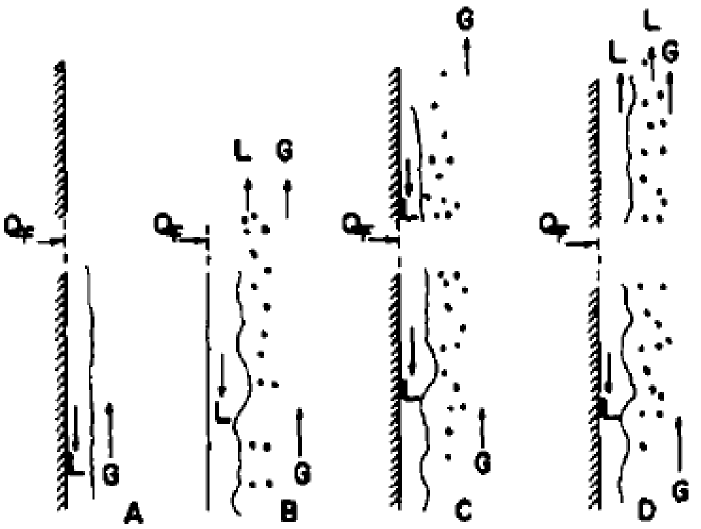

Figure 9: Development of flooding [12]. *The liquid feed (*Q_F*) is split at the onset of flooding or liquid loading and only a part of the liquid feed moves upward.*

loading. With even smaller gas velocities, the same liquid flow rate cannot be maintained in the annular flow regime. Graph D of Figure 9 depicts such a condition where the gas cannot lift all the liquid feed (Q_F) upwards. At a particular stage all the liquid will start to flow down (graph A of Figure 9). On the other side, by increasing the gas velocity from zero, the liquid flow will shift

Figure 10: Experiments done at a $U_{SL} = 1\ cm/s$*. The left graph is at a* $U_{SG} = 10.6\ m/s$ *and the right one is at a* $U_{SG} = 8.5\ m/s$ *which is close to the onset of liquid loading. The roughness and the chaotic nature of the liquid structures are more pronounced in the second case and therefore marks the start of churn flow.*

from total downflow (counter-current flow, graph A of Figure 9) to a stage where liquid droplets would start to get sprinkled in the upward direction beyond the liquid and gas injection points. This condition is called flooding (Image B of Figure 9, [1]).

The occurrence of flooding can be defined as the point at which a complete transition from annular flow to churn flow has been established [4]. However, most of the lab tests in the present project are conducted near the annular regime and they therefore occur near the liquid loading point, rather than near the flooding point. From visual observation, it is seen that the chaotic nature will start to occur at the liquid loading conditions (Figure 10), and hence this can be considered as the trigger for the transition from the annular flow regime to the churn flow regime.

2.6. Flow experiments

Two-phase flows have been studied extensively due to its application in, among others, the nuclear industry and the oil and gas industry (sec. 1.2) [6], [8]–[16]. The present project is focussed on the flow of wet gas in annuli. Some authors have taken the test data directly from operating gas fields [8], but most of the experimental data were obtained under controlled settings in the lab [7], [9], [12], [15], using air or nitrogen to represent the gas in gas-liquid flows. In the experiments available in the literature, mostly water is used as the liquid in multiphase flow lab tests, with a few exceptions [11]. The experiments conducted in the present study use tap water for the liquid and dry air for the gas.

Considerable experimental work has also been done for gas-liquid flows in (circular) pipes.

2.6.1. Co-current flows

Caetano et al. [7] have conducted experiments with varying gas and liquid velocities (Figure 8). The net movement of both the phases are in the direction of the gas (upwards) (Figure 7). This is ensured by preventing the backflow of liquid at all conditions and maintaining the required U_{SL} by using check valves or by employing appropriate pressure drops (Experimental Program of [7]). Such a setup would be ideal for studying flows around the liquid loading point, but not at the flooding point. Several researchers have also done experiments in a similar fashion [8], [9], [11], [16]. Co-current flows and liquid loading are studied in relation to the two-phase flows in the oil and gas industry.

2.6.2. Free flows

Some experimentalists have not 'forced' the liquid to rise along with the gas. This could result in experiments to turn into either co-current or counter-current and can exhibit both flooding and liquid loading (Figure 9, Figure 11). The phenomenon and mechanism of shifting from co-current to counter-current and vice versa is explained in sec. 2.5.

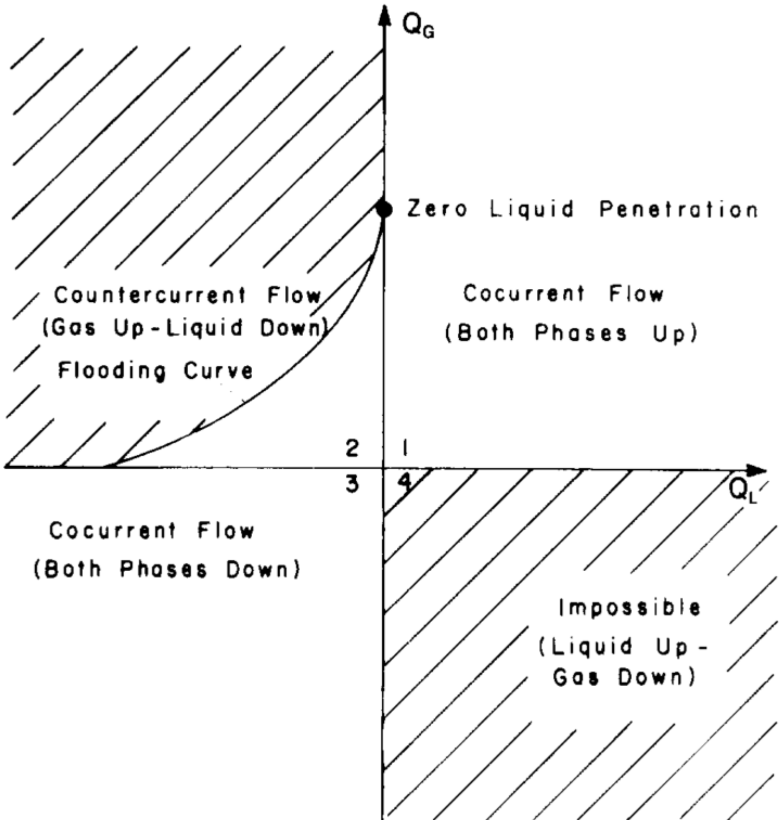

Figure 11: Two-phase flow in vertical conduits. The second quadrant represents counter-current flow. Richter [14] *has focused on flooding in tubes and annuli. A 'liquid loading' curve should also exist in the first quarter.*

Maron et al. [13] have modelled and experimentally verified the two phase flow by solving the steady, laminar, one-dimensional momentum equation for the liquid films by considering them as an incompressible, Newtonian fluid. They have considered the entire spectrum encompassing a total downflow ($U_{SG} = 0$) and one with a very high U_{SG} (very thin films). A few others have also looked into both the co-current flows as well as the counter-current flows [10], [12], [14], [15]. Studies on free flows and flooding have been conducted mainly for the design of nuclear reactor core cooling systems [14].

A point, however, to be noted is that annular flows are exhibited in the same fashion irrespective of whether the experiments are conducted in the co-current or free manner. Annular flows require very high gas velocities ($U_{SG} > 9\ m/s$ for concentric and $U_{SG} > 6\ m/s$ for eccentric annuli) to ensure that the liquid films are lifted.

2.7. Modelling

The physical descriptions of the two-phase flows have been employed in the past to model the various flow patterns [10], [11], [13], [14], [16]–[18]. Successful attempts included the creation of flow pattern maps to recognize different flow patterns. Apart from this, modelling specific for the flow patterns has also been done to better understand and derive the various flow parameters like pressure gradient, holdup. etc. (sec. 6.4).

2.7.1. Flow pattern map

A typical flow pattern map is shown in Figure 8. Taitel et al. [17] are among the first researchers to represent a gas-liquid flow with physically realistic mechanisms to determine a theoretical distinction between various flow patterns in a horizontal/near-horizontal pipe. Caetano et al. [7] extended the concept to derive a flow pattern map for two-phase flows in an annulus, for both concentric and fully eccentric ones. Das et al. [18], Kelessidis et al. [16] and Lage et al. [8] also used the same concept to verify their experiments for a vertical concentric annulus.

2.7.2. Flow-specific modelling

Specific modelling is required for the different flow types, as the flows differ substantially from each other. Caetano et al. [11] used the principles proposed by Taitel et al. [17] for the modelling of each of the principal flow regimes separately, as occurring in an annulus. Various others also attempted to create flow pattern maps and flow-specific modelling in pipes and annuli [19], [20].

The primary aim of this project is to model the annular flow with suitable modifications to accommodate the churn flow also (sec. 1.3). Since the idea revolves around the annular flow, inputs from researchers on both the co-current flows and the free flows (sec. 2.6) could be used.

2.8. Film distribution in annular flow in an annulus

Two phase annular flow in a circular pipe consists of a thin liquid film flowing along the inside wall of the pipe and a gas core in the centre ('Annular' of Figure 50). However, for an annulus there would be two films and a gas core as depicted in Figure 19, thus making the modelling and measurement slightly complicated.

During extraction of the natural gas from the reservoirs, the liquid gets mixed up from different directions (sec. 3.1). Liquid could be transported in varying proportions along the inner wall (inner liquid film) and along the outer wall (outer liquid film). To simplify the study, the term liquid film thickness ratio, T, will be defined as the ratio between the inner and the outer liquid film thicknesses [7].

The gas and liquid extracted from the reservoirs travel a few kilometres before it reaches the surface. The entrance length or development length in an annulus is approximated to be at $150D_h$ [21]. Therefore, within the first kilometre the flow can be assumed to have reached a fully developed and stable state for natural gas extraction pipes. Most researchers have attempted to model the flow for such fully developed conditions, which means that the ratio T is assumed to be constant over the length of the pipeline (Table 1). Caetano et al. [11] used the principle of atomisation, entrainment and deposition to arrive at a film ratio as a function of the eccentricity (sec. 8.2) and diameter ratio (K= $\frac{D_i}{D_o}$) (see Appendix A: Sub-model for film thickness ratio). Bangtang et al. [22] even extended this concept for the liquid films to a slug flow. Other authors preferred to stick to a constant of 1 for simplicity.

Table 1: Summary of values of T being used by different authors. Most of them prefer a unit ratio for model simplicity.

Author	Year	T
Caetano et al.[11]	1992	Variable (0.4-1.0)
Kelessidis et al. [16]	1989	1
Lage et al. [8]	2000	1
Richter [14]	1981	1
Bangtang et al. [22]	2014	Variable (0.4-1.0)

As mentioned before the flow will only get fully developed after some distance from the reservoir. The exact length of the development length is not part of this study. The setup of this project also has the option to inject liquid along the inner and outer pipes separately (sec. 3.1). High definition video cameras are placed next to the pressure sensors at the top to record the experiments.

To make a qualitative assessment, for the same superficial liquid velocity, liquid was injected in extreme ratios along the inner and outer walls. It was noticed that at high gas velocities the mixing of liquid films becomes minimum for such a short setup. As it approaches churn flow (low gas velocities) the redistribution of the liquid flow between inner and outer films would occur rapidly.

The model developed as part of this work applies the following input for the throughput: one gas flow rate and two liquid flow rates for the two films. Since the minimum mixing between the films occurs at high superficial gas velocities ($\approx 31\ m/s$), the corresponding results could be compared for the model with varying ratios of the film flow rates (sec. 7.3).

3. Experimental setup

3.1. Description

Figure 12: The experimental setup as built for the project. The equipment is designed to conduct tests with varying eccentricities, flow rates and even inclinations.

The equipment is primarily designed for co-current (sec. 2.6.1) churn flow and annular flow. The basic schematic is shown in Figure 13 and can be compared against Figure 19 for a better understanding. The gas and liquid flow rates are regulated using flowmeters and are supplied at the base. The gas would lift the liquids up to the measuring station. The discussion as to whether the measuring station would encounter a fully developed flow was dealt with in sec. 2.8.

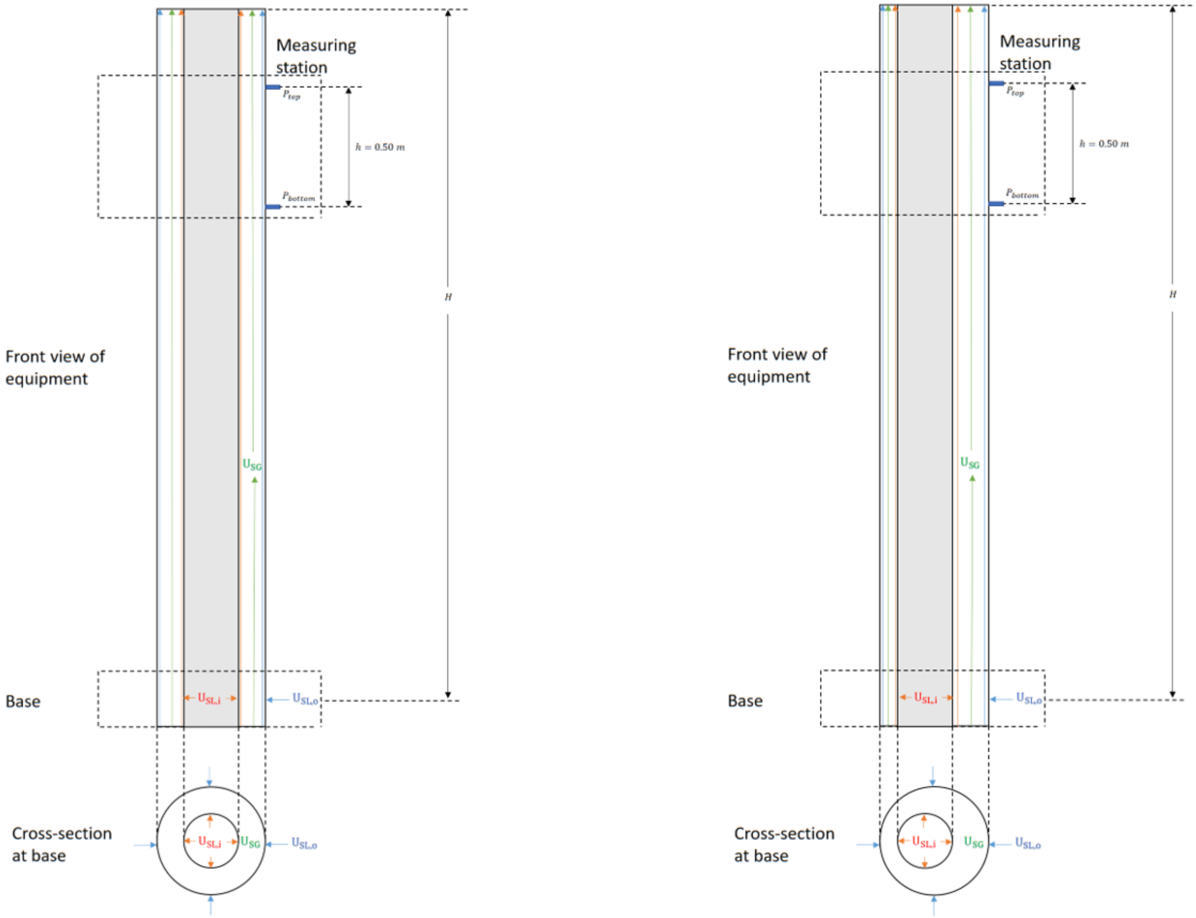

Figure 13: A schematic representation of the equipment (not to scale). The concentric and the eccentric configurations are shown on the right and the left sides of the figure. The gas and liquid inlets are given at the base. At the measuring station we have pressure sensors mounted on the outer wall and there is a high-speed camera that is kept at a distance.

Two measurements are primarily taken for a set of flow rates/gas and liquid superficial velocities:

- Pressure gradient, $-\Delta_z P$ (eq. (39))
- Liquid holdup, α_L (sec. 6.5)

The pressures at the top and bottom of the measuring station are measured using pressure sensors separated at a distance, h, equal to 0.50 m. The sensors are shown in the schematic (Figure 13); these measure the pressures denoted as P_{top} and P_{bottom}. The pressure gradient is thus:

$$-\Delta_z P = -\frac{P_{top} - P_{bottom}}{h} \tag{1}$$

The measurement of the holdup is not direct. Once the pressure gradient is recorded the gas and liquid flows are stopped simultaneously with the help of quick closing valves. The liquid films, waves or slugs present within the equipment would flow down, as there is no more gas to lift them up; the liquid accumulates near the base. The total volume of liquid (V) thus measured near the base of the equipment corresponds to the liquid hold up during the operation for a set of flow rates for the entire length of the annulus pipe (H). The value of H depends on whether the flow was operated at liquid loading conditions. The liquid holdup, α_L, is thus measured as:

$$\alpha_L = \frac{V}{A \times H} \tag{2}$$

where A is the annulus area (sec. 6.5).

The holdup measured has an error of less than 1% for annular flows and 3% for churn flows.

3.2. Limitations

The main limitations of the equipment are:

- The short length (2.630 m) of the equipment. The study of fully developed flows at high superficial gas velocities is hence restricted (sec. 2.8).
- The separator at the top of the setup removes the gas and liquid. It can interfere with churn flows, where flow reversal happens due to its chaotic nature, causing exit effects. Flow reversals are a part of the churn flow. Since the separator removes the liquid at the exit the flow reversal is halted, and dry patches would start to appear.
- The flowmeters and the water source used were not stable enough to regulate a constant liquid flow. This could have affected the experiments.

4. Experimental results

A total of approximately 400 tests were conducted with superficial liquid velocities, U_{SL}, of:

- $0\ cm/s$
- $0.5\ cm/s$
- $1\ cm/s$
- $2\ cm/s$
- $4\ cm/s$

and eccentricities, e, of:

- 0 (concentric)
- 0.50
- 0.75

For each combination of U_{SL} and e the superficial gas velocity, U_{SG}, was varied from $3\ m/s$ to $30\ m/s$ to get approximately 11 to 14 data points. Three primary graphs with the measurement results for a vertical annulus with an outer diameter, $D_o = 60\ mm$ and an inner diameter $D_i = 40\ mm$ will be provided:

- Pressure gradient versus holdup, i.e. $-\Delta_z P$ (Pa/m) vs. α_L (-).
- Pressure gradient versus superficial gas velocity, i.e. $-\Delta_z P$ (Pa/m) vs. U_{SG} (m/s).
- Holdup versus superficial gas velocity, i.e. α_L (-) vs. U_{SG} (m/s).

4.1. First impression of the results

The graphs for all the superficial liquid velocities for eccentricities of 0 and 0.75 are provided in this section.

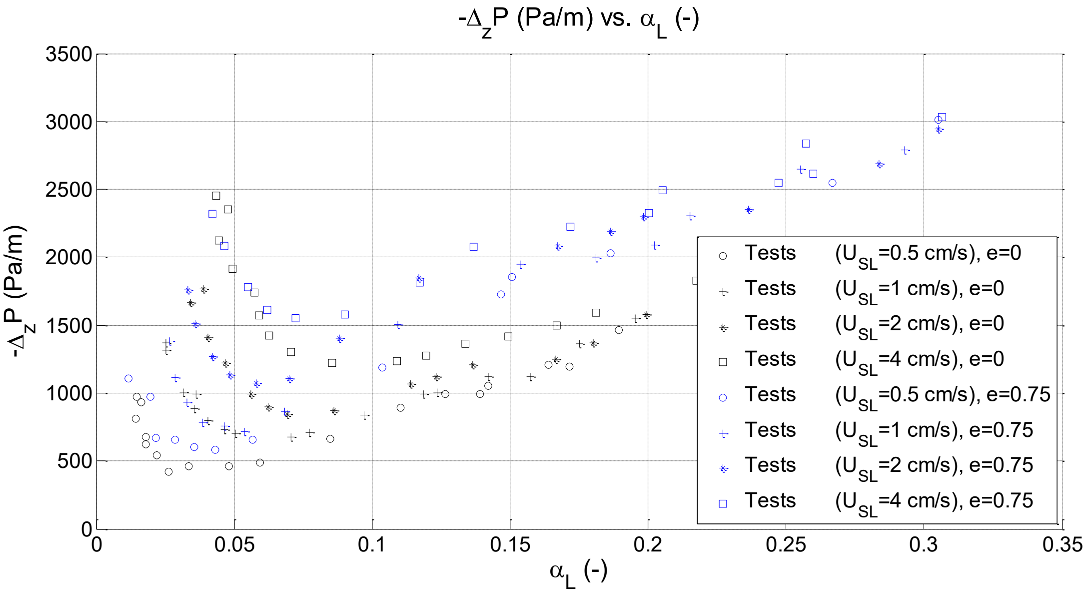

Figure 14: Pressure gradient versus holdup. For the higher holdup values, the pressure drop increases with increasing eccentricity.

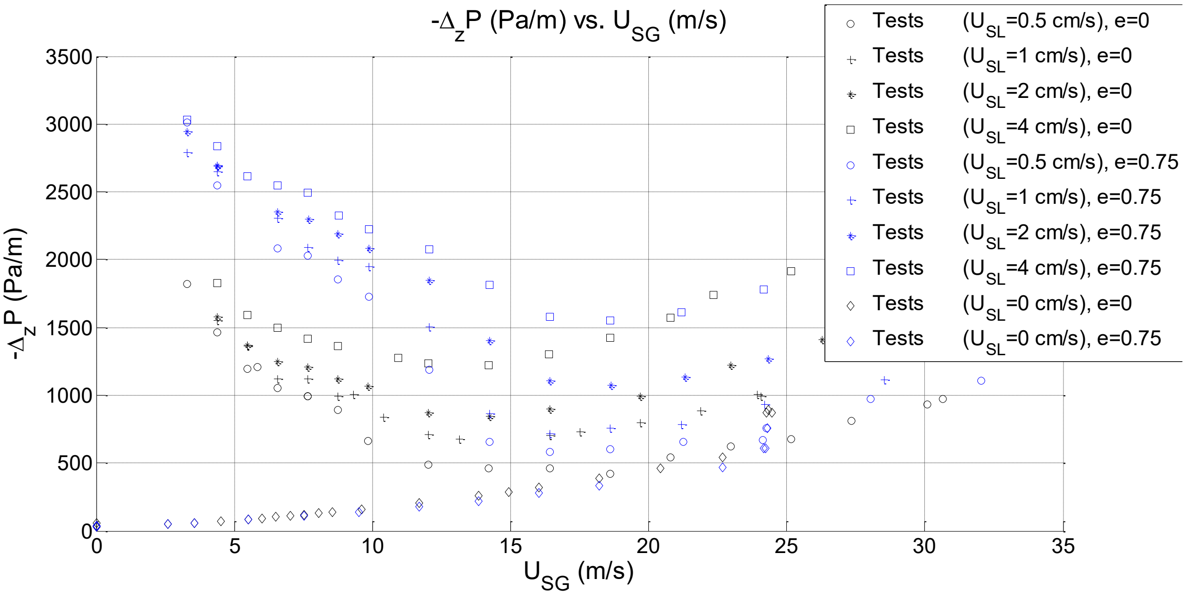

Figure 16: Pressure gradient versus the superficial gas velocity. The pressure gradient increases with increasing eccentricity.

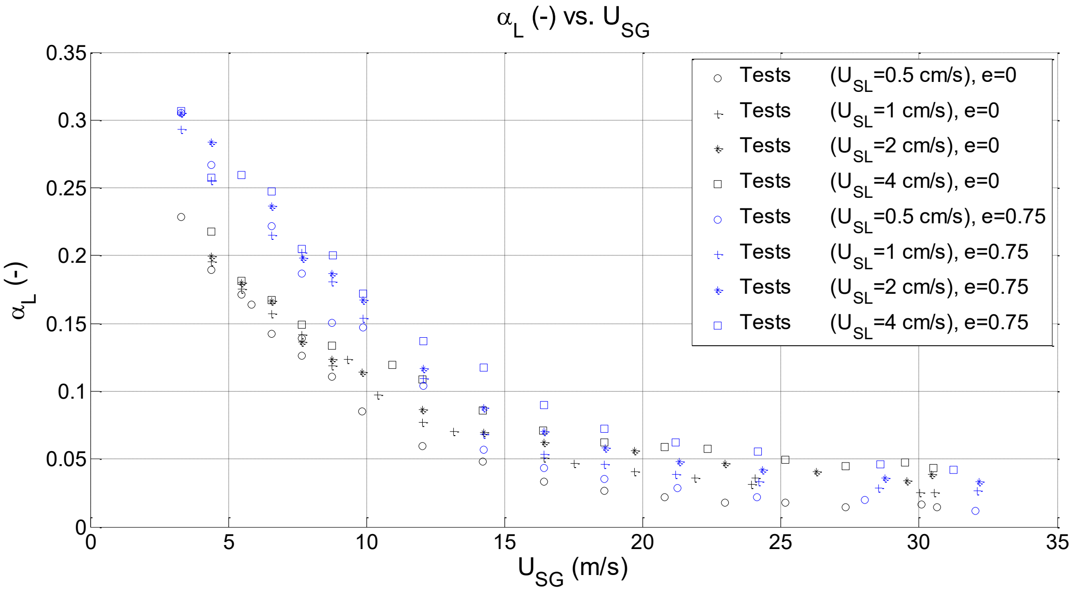

Figure 15: Holdup versus superficial gas velocity. The holdup increases with increasing eccentricity.

The first observations are the following:

- For the higher holdup values, the pressure drop increases with increasing eccentricity (Figure 14).
- At lower superficial gas velocities, the pressure gradient is much higher for two-phase flow than for a single-phase flow (Figure 16). This can be explained with the help of the Wallis correlation for the interfacial friction factor (eq. (16)). At a lower gas velocity, the holdup and therefore the film thickness is very high which can increase the film 'roughness'. This in turn would lead to a higher pressure gradient.

- The holdup increases with eccentricity (Figure 15). However, the relation between the holdup and the superficial gas velocity is less clear for varying superficial liquid velocities.

For a proper understanding of the experiments, various combination of U_{SL} $(1\ cm/s$ and $4\ cm/s)$ and eccentricities (0, 0.5 and 0.75) will be selected for comparison with model predictions. The results will be presented in the later chapters.

5. Film flow on a wall

5.1. Introduction

The objective of this project is to understand certain regimes of multiphase flow in an annulus. In this chapter the modelling of the liquid film flow along a wall [10] will be explained, as a precursor for the better understanding of the modelling of gas-liquid annular flows in annuli. Figure 17 shows the schematic representation of a film flow on a wall. The modelling for a pipe is discussed in Appendix G: Modelling of pipe. The comparison between the pipe and the annulus is shown in Table 4.

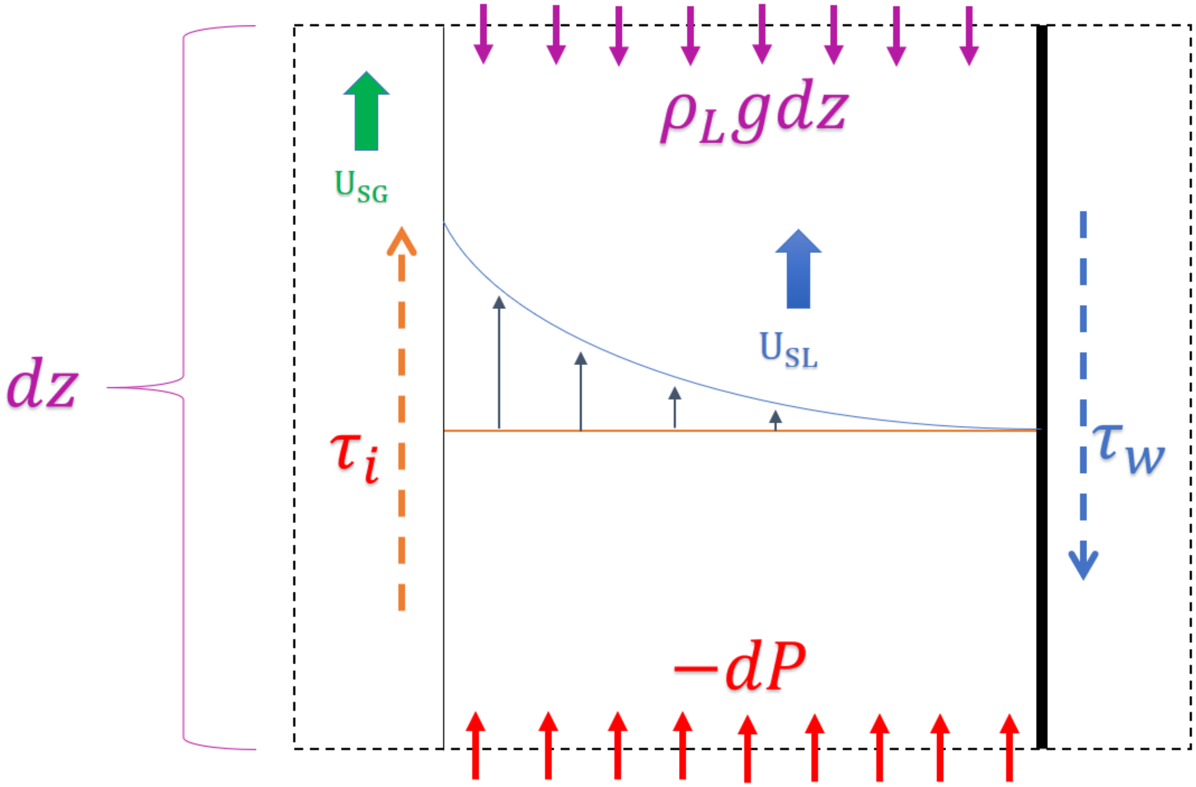

Figure 17: Film flow on a wall with a differential height of dz. In the figure, the film velocity profile is shown. The film is forced up with the drag caused by the gas and the pressure gradient. The resisting forces are gravity and wall shear.

5.2. Momentum balance

The liquid film is shown in Figure 18. A momentum balance on the film is considered, involving the pressure, gravity, interfacial and wall shear stresses. The control volume is bounded by the film surface and the wall surface within a differential element dz:

$$\tau_i dz \times S - \tau_w dz \times S + (-dP) \times A_f - \rho_L g dz \times A_f = 0$$

where,

S is the width of the film, and $A_f = S\delta_f$ is the film area, in which δ_f is the thickness of the film. The control volume considered in Figure 18 is a part of an infinite film spread across an infinite flat plate. Hence the length, S, across the wall and the interface is the same, unlike the one for a pipe or an annulus.

The wall shear stress is hence given by,

$$\tau_w = \frac{\left[\left(\left[-\frac{dP}{dz}\right] - \rho_L g\right) A_f + \tau_i S\right]}{S} \tag{3}$$

The shear stress can be derived for any point at a distance y from the wall in a similar way:

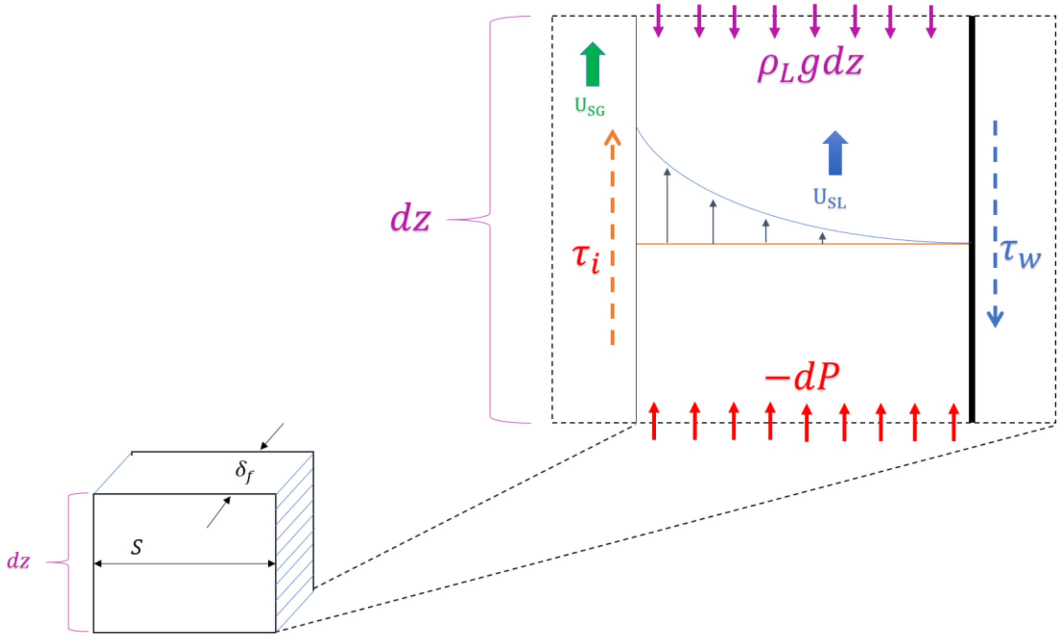

Figure 18: The liquid film and the forces acting on it. A momentum balance on the film is considered, with the pressure, gravity, interfacial and wall shear stresses.

$$\tau_y = \frac{\left[\left(\left[-\frac{dP}{dz}\right] - \rho_L g\right) A_y + \tau_i S\right]}{S} \tag{4}$$

where the variables with the subscript y correspond to the variables given in eq. (3).

Since the shear stress at each point is now known, the velocity gradient can also be expressed though using the viscosity for a Newtonian flow:

$$\frac{du}{dy} = \frac{\tau_y}{\mu_{eff}} \tag{5}$$

It is worthwhile to note that the effective viscosity $\mu_{eff} = \mu_L$ in eq. (29), assuming laminar flow in the film [13]. The next chapter deals with flows in annuli; there turbulence sub-modelling is explained along with the laminar flow (sec. 6.6.1). With appropriate boundary conditions, the velocity profile can be determined and therewith the superficial liquid velocity, U_{SL},at a given pressure gradient,$\left[-\frac{dP}{dz}\right]$ and holdup, α_L which is a function of film thickness, δ_f.

This part of the modelling will be referred to as the **Liquid sub-model**, and it can be summarized as follows:

$$\left[-\frac{dP}{dz}\right] = f_1(U_{SL}, \delta_f) \tag{6}$$

The superficial gas velocity, U_{SG}, can be expressed as a function of $\left[-\frac{dP}{dz}\right]$ and of the interfacial friction factor, f_i:

$$U_{SG} = f_4(\left[-\frac{dP}{dz}\right], f_i) \tag{7}$$

Where f_i is the interfacial friction factor for which many correlations are available, which will be discussed in section on the modelling for annuli (sec. 6.6.2). f_i is generally a function of the film thickness, δ_f.

Eq. (7) can now be summarized as follows, which will be referred to as the **Gas sub-model**.

$$\left[-\frac{dP}{dz}\right] = f_2(\delta_f, U_{SG}) \tag{8}$$

In essence, the pressure gradient can be calculated if the superficial gas velocity (**Gas sub-model**) or the superficial liquid velocity (**Liquid sub-model**) is given along with the holdup. The **Liquid sub-model** gives the pressure gradient at a specified U_{SL} and α_L. These calculated values of the pressure drop and the liquid holdup can be used in the **Gas sub-model** to obtain the value for U_{SG}. Therefore, the **Liquid sub-model** and the **Gas sub-model** can be combined to the **Full Model** as defined below:

$$\left[-\frac{dP}{dz}\right] = f_3(U_{SL}, \delta_f, U_{SG}) \tag{9}$$

The modelling of the liquid flow along the walls of an annulus (sec. 6) is just an extension of the modelling for the film flow along a pipe wall. Table 2 summarizes the comparison of the models for the two configurations.

Table 2: Summary of sub-models used for a film flow along a pipe wall and along annulus walls. An additional closure is required for the annulus for the thickness ratio between the inner and outer films.

	Film flow on a pipe wall	**Film flow along annulus walls**
Liquid sub-model	$\left[-\frac{dP}{dz}\right] = f_1(U_{SL}, \alpha_{\mathrm{L}})$	$\left[-\frac{dP}{dz}\right] = f_1(U_{SL,o}, U_{SL,i}, \alpha_{\mathrm{L,o}}, \alpha_{\mathrm{L,i}})$
Gas sub-model	$\left[-\frac{dP}{dz}\right] = f_2(\alpha_{\mathrm{L}}, U_{SG})$	$\left[-\frac{dP}{dz}\right] = f_2(\alpha_{\mathrm{L,o}}, \alpha_{\mathrm{L,i}}, U_{SG})$
Full model	$\left[-\frac{dP}{dz}\right] = f_3(U_{SL}, \alpha_{\mathrm{L}}, U_{SG})$	$\left[-\frac{dP}{dz}\right] = f_3(U_{SL,o}, U_{SL,i}, \alpha_{\mathrm{L,o}}, \alpha_{\mathrm{L,i}}, U_{SG})$
Turbulence/laminar sub-model	Yes	Yes
Interfacial friction factor	Yes	Yes
Other closures	No	Film thickness ratio - T (sec. 6.5)

6. Modelling of annulus flow

6.1. Introduction

The gas-liquid annular/churn flow in a vertical concentric annulus is simulated and explained in this chapter [13]. In an annulus flow (Figure 19), there is:

- A liquid film on the inside of the outer tube (casing), known as the outer film (casing film).

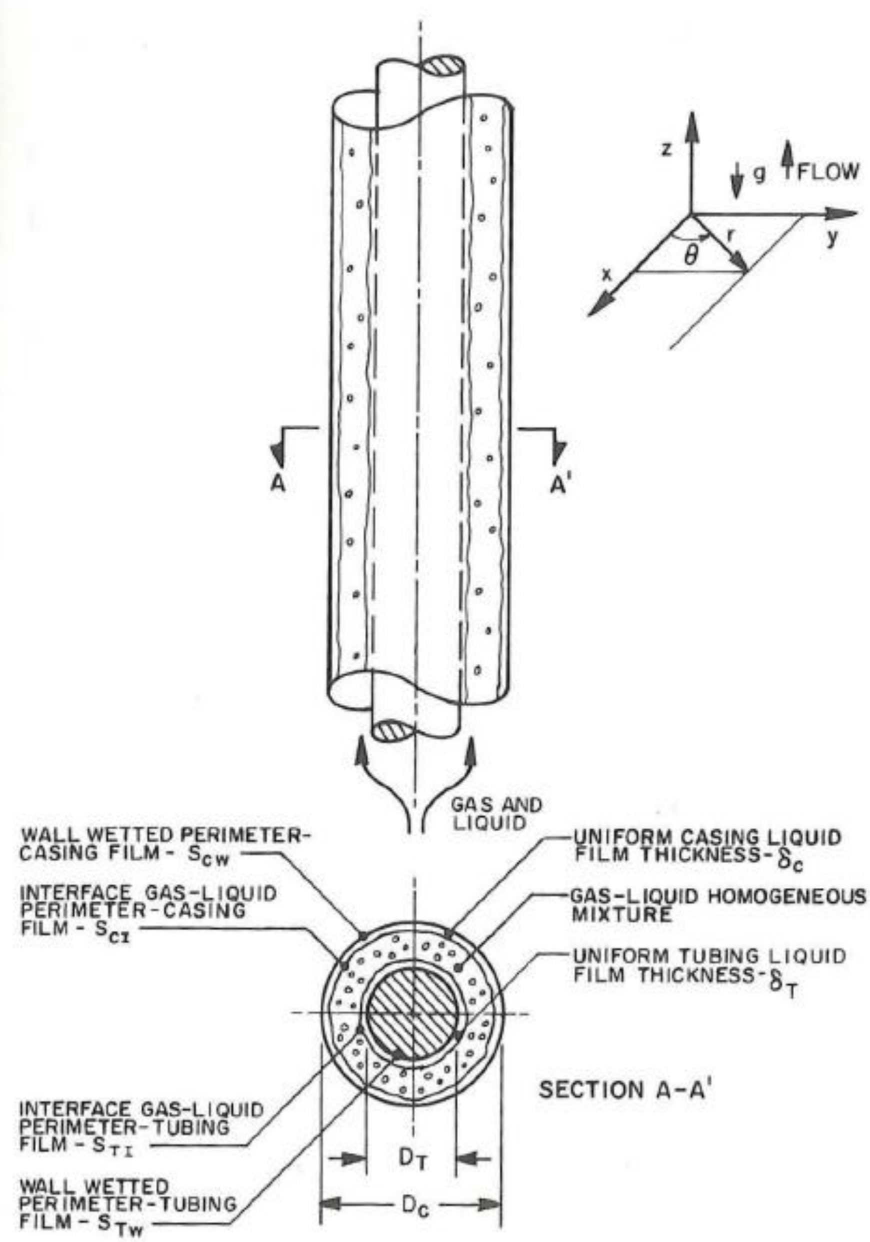

Figure 19: Annular flow in a vertical concentric annulus [2]. Note the presence of two liquid films and gas core with entrained liquid droplets. The net movement of both the gas and liquid is upwards.

- A liquid film on the outside of the inner tube (tubing), known as the inner film (tubing film).

- A gas-liquid core between the liquid films.

The following assumptions have been made in the film model:

- The liquid films are non-aerated.
- The entrainment of liquid droplets in the gas core is zero. Zabaras et al. [12] have reported an entrainment rate of approximately 15% of the total liquid flow rate for annular flows in pipes [12]. Caetano et al. [11], however, have accommodated the entrainment, as shown in Figure 19, for their analysis.
- Constant thickness of the liquid films along the axis as well as around the circumference. The presence of waves is thus averaged out as part of the mean thickness [13]. Schubring et al. [23], however, have considered the wave characteristics for his model.
- The flow is stable and incompressible. The effects of atomization and deposition are negligible.
- There is a pressure gradient (negative) only in the direction of the flow (z direction).

The liquid films will be frequently referred to as just films and the gas core as core. The subscript o for a variable corresponds to the outer pipe and i to the inner pipe. For example, $U_{SL,o}$ refers to the superficial liquid velocity along the outer pipe. To refer to the inner or the outer film, we will use a subscript o/i, as in $\delta_{fo/i}$ for the film thicknesses.

6.2. Throughputs

The main variables which are controlled throughout the experiments are the liquid and gas flow rates.

Liquid flow rate along the outer tube, $Q_{L,o}$.

Liquid flow rate along the inner tube, $Q_{L,i}$.

Gas flow rate within the annulus, Q_G.

To be consistent with the commonly used flow variables, the flow rates will be expressed through superficial velocities:

Superficial liquid velocity for the outer tube, $U_{SL,o} = \frac{Q_{L,o}}{A}$.

Superficial liquid velocity for the inner tube, $U_{SL,i} = \frac{Q_{L,i}}{A}$.

Superficial gas velocity within the annulus, $U_{SG} = \frac{Q_G}{A}$.

Since superficial velocities and flow rates are closely related (there is a fixed multiplication factor between them), both terms will be used interchangeably.

6.3. Full model

The full model for the annuli is summarized below and the flow chart is depicted in Figure 20 and eq. (10). The full model is comprised of the liquid and gas sub-models and the name of a few upcoming sections and sub-sections specify to which sub-model it is most associated. The last chapter defined the liquid sub-model and the gas sub-model and established them as independent functions. The inputs to the function f_3 (eq. (10)) are the liquid superficial velocities ($U_{SL,o}, U_{SL,i}$), the gas superficial velocities (U_{SG}) and the holdups ($\alpha_{L,o}, \alpha_{L,i}$). The targeted outputs are the pressure gradient ($\left[-\frac{dP}{dz}\right]$) from which all other flow variables could be calculated. These outputs may appear as a necessary information for some of the modelling equations even before they are calculated. In such cases a 'guess' for such variables is taken initially and then 'refined' through iterations. The exact process is described in Appendix I: Flow chart/programming.

$$\left[-\frac{dP}{dz}\right] = f_3(U_{SL,o}, U_{SL,i}, \alpha_{\mathrm{L,o}}, \alpha_{\mathrm{L,i}}, U_{SG}) \tag{10}$$

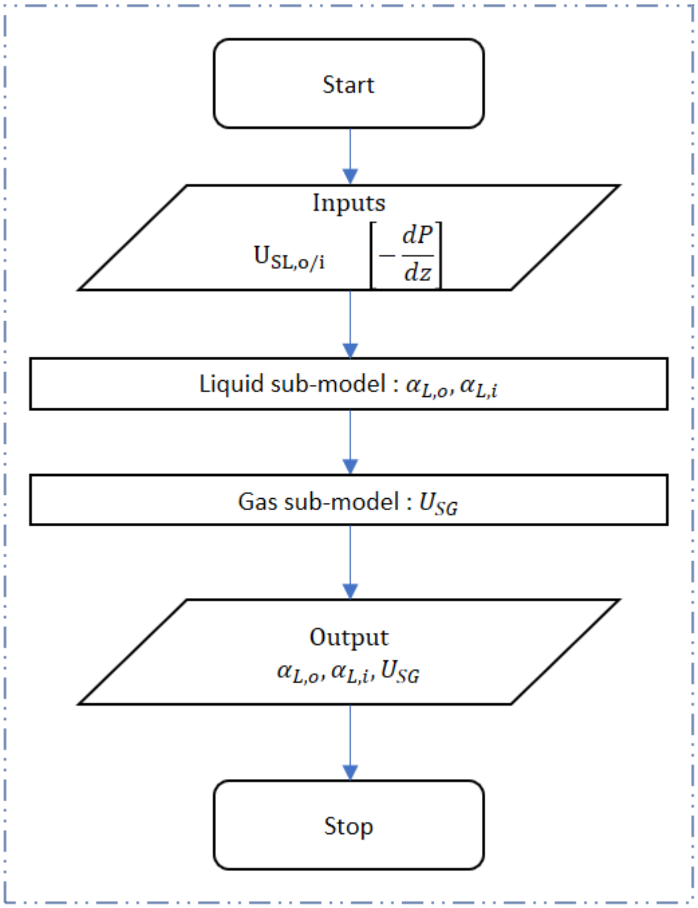

Figure 20: Flow chart for the full model of an annulus. The superficial gas and liquid velocities are 'independent' of each other and are functions of the pressure gradient and holdups.

6.4. Modelling structure (liquid sub-model)

The different modelling domains of the liquid sub-model are the following:

- Geometry - The length scales of the flow, like film thicknesses, interfacial perimeters, etc. are defined as in [24].
- Force - The shear stresses, pressure gradients, etc. are defined as in [24].

The descriptions are given in the following section and Appendix H: Force balance for annulus. The summary of the modelling can be formulated as follows:

$$\left[-\frac{dP}{dz}\right] = f_1(U_{SL,o}, U_{SL,i}, \mathrm{\alpha_{L,o}}, \mathrm{\alpha_{L,i}}) \tag{11}$$

6.5. Geometry (liquid and gas sub-models)

The basic geometry of the films and the core is described below and will be used both in the liquid and gas sub-models:

Inner film thickness, δ_{fi} .

Outer film thickness, δ_{fo}.

Inner tube diameter, D_i.

Outer tube diameter, D_o.

Annular radius, $d = \frac{D_o - D_i}{2}$.

Inner wall perimeter, $S_{wi} = \pi D_i$.

Outer wall perimeter, $S_{wo} = \pi D_o$.

Inner interfacial perimeter, $S_{ii} = \pi(D_i + 2\delta_{fi})$.

Outer interfacial perimeter, $S_{io} = \pi(D_o - 2\delta_{fo})$.

Inner film area, $A_{fi} = \frac{\pi}{4}[\,(D_i + 2\delta_{fi})^2 - (D_i)^2\,]$.

Outer film area, $A_{fo} = \frac{\pi}{4}[\,(D_o)^2 - (D_o - 2\delta_{fo})^2\,]$.

Annulus area, $A = \frac{\pi}{4}(D_o^2 - D_i^2)$.

Gas core area, $A_c = \frac{\pi}{4}[\,(D_o - 2\delta_{fo})^2 - (D_i + 2\delta_{fi})^2\,]$.

Inner film holdup, $\alpha_{L,i} = \frac{A_{fi}}{A}$.

Outer film holdup, $\alpha_{L,o} = \frac{A_{fo}}{A}$.

Total liquid holdup, $\alpha_L = \alpha_{L,i} + \alpha_{L,o}$.

Ratio of inner to outer film thicknesses, $T = \frac{\delta_{fi}}{\delta_{fo}}$ [11].

The calculation of the shear stresses for an annulus is similar to the one explained for film flow on a wall (sec. 5.2). The derivation is provided in Appendix H: Force balance for annulus.

6.6. Closures

Two primary closures are used in the model. These are described in this section.

6.6.1. Velocity profile (liquid sub-model)

The computation of the velocity profiles within the films is necessary to find the superficial liquid velocities and to compare them against the throughputs given as inputs (sec. 6.4). More of this will be discussed in Appendix I: Flow chart/programming. For the velocity distribution, two different closures are studied to determine the velocity distribution and these are discussed below.

6.6.1.1. Turbulent flow

The turbulence model studied here is based on the mixing length theory with a Van Driest parameter, $A^{+} = 150$ [24], [25].

For the film (outer), the friction velocity is

$$u^{*} = \sqrt{\left|\frac{\tau_{wo}}{\rho_L}\right|} \tag{12}$$

and the velocity profile is derived as

$$\frac{du}{dy} = \frac{\tau_{yo}}{\mu_l + \mu_{\tau o}} \tag{13}$$

with an eddy viscosity that can be expressed as

$$\mu_{\tau o} = \rho_l \kappa y u^{*}(1 - e^{-\frac{y}{\delta_{vo} A^{+}}}) \tag{14}$$

with the viscous length $\delta_{vo} = \frac{\nu_l}{u^*}$ and the Von Kármán constant $\kappa = 0.41$. ν_l is the kinematic viscosity of the liquid.

A no-slip boundary condition is used for the film velocity at the wall. The expression for the inner film is same as that for the outer film.

6.6.1.2. Laminar flow

A film with laminar flow is also modelled and compared against the turbulence sub-models [13]. Eq. (13) is used with

$$\mu_{\tau o} = 0 \tag{15}$$

to define the velocity profile along the wall with the no-slip boundary condition.

6.6.2. Interfacial friction factor (liquid and gas sub-models)

A closure for the dimensionless interfacial friction factor I is required (eq. (36)). The Wallis (1969) correlation is as shown below:

$$I = 1 + 300\frac{\delta_{fo/i}}{D_h} \tag{16}$$

in which the hydraulic diameter can be expressed as $D_h = D_o - D_i$, for an annulus.

In hindsight a pre-factor of 600 will be used, instead of 300, to match the test results better. Using this correlation, it can be seen that the friction increases with the film thickness. The thicker the films, the larger the waves at the liquid-gas interface will be, which increases the effective roughness experienced by the gas which thus leads to a higher interfacial shear stress.

We have thus used the following expression:

$$I = 1 + 600\frac{\delta_{fo/i}}{D_h} \tag{17}$$

This relation, however, could still not accurately reproduce the superficial gas velocities when the flow approaches the churn flow regime (see Appendix D: Modified Wallis). Thus, the following correlation was finally used in the current model [26]:

$$I = 1.5 + 100\frac{\delta_{\mathrm{fo}/i}}{D_h} + \gamma\frac{\delta_{fo/i}^2}{D_h^2} \tag{18}$$

where,

$$\gamma = A_\gamma D^2 + B_\gamma D + C_\gamma \tag{19}$$

with $A_\gamma = 1.5 \times 10^7\ m^{-2}$, $B_\gamma = -6.7 \times 10^{5a}\ m^{-1}$ and $C_\gamma = 2.0 \times 4\ \ m^{-1}$.

All the model results described in the upcoming chapters used this relation unless mentioned differently.

There are also various other studies conducted with regards to the suitability of the interfacial friction factors specific to annular flows [27], [28].

6.7. Gas sub-model

The gas sub-model is straightforward and can be derived as below:

$$\left[-\frac{dP}{dz}\right] = 4\mathrm{f_{iw}}\frac{\frac{1}{2}\rho_\mathrm{L}\mathrm{U_{SG}^2}}{\mathrm{D_h}}$$

$$\mathrm{U_{SG}} = \sqrt{\frac{\left[-\frac{dP}{dz}\right]\mathrm{D_h}}{4\mathrm{f_{iw}}\frac{1}{2}\rho_\mathrm{L}}} \tag{20}$$

where f_{iw} is the interfacial friction factor with ‘wetted-perimeter’ weighting [24] and is given as:

$$f_{iw} = \frac{S_{ii}f_{ii} + S_{io}f_{io}}{S_{ii} + S_{io}}$$

The sub-model can be thus summarized as:

$$\left[-\frac{dP}{dz}\right] = f_2(\alpha_{\mathrm{L,o}}, \alpha_{\mathrm{L,i}}, U_{SG}) \tag{21}$$

It is to be noted that the friction factors are functions of the film thicknesses (eq. (18)) and thus of the holdups. The flow chart for the programming of this model is provided in Appendix I: Flow chart/programming.

7. Results – Part 1

Three primary graphs with the results for a vertical concentric annulus with an outer diameter of $D_o = 60\ mm$ and an inner diameter of $D_i = 40\ mm$ will be provided:

- Pressure gradient versus holdup ($-\Delta_z P$ (Pa/m) vs. α_L (-)) – from the liquid sub-model.
- Pressure gradient versus superficial gas velocity ($-\Delta_z P$ (Pa/m) vs. U_{SG} (m/s)) – from the full model.
- Holdup versus superficial gas velocity (α_L (-) vs. U_{SG} (m/s)) – from the full model.

7.1. Modelling results

This section discusses the results of the modelling described in chapter 6. The turbulence (sec. 6.6.1.1) and laminar (sec. 6.6.1.2) closures were used to simulate the velocity profiles in the liquid films. The same model will be displayed as two different curves representing the two velocity distribution closures.

The expected trend for the pressure gradient versus the holdup will be the one described by Maron et al. [13], which is shown in Figure 22. The relation between the dimensionless film thickness and the dimensionless interfacial shear stress was derived by solving the equation for steady, laminar, one-dimensional flow for an incompressible Newtonian fluid at a constant liquid flow rate. The dimensionless film thickness and the dimensionless interfacial shear stress are physically analogous to the holdup (sec. 6.5) and pressure gradient (eq. (39)), respectively.

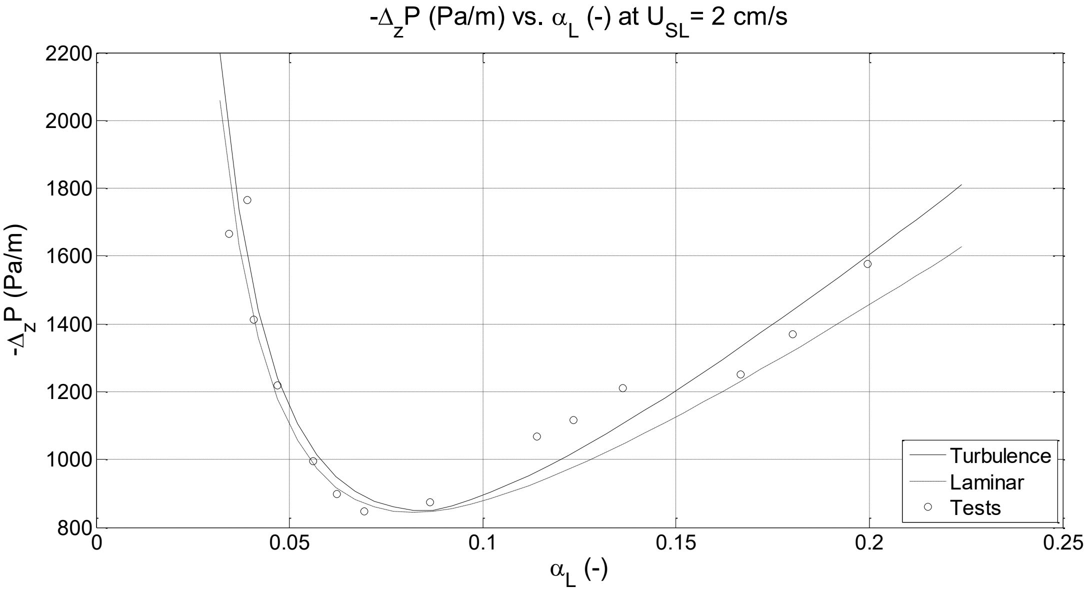

Figure 21: Pressure gradient versus holdup. The model performance under two different velocity profile closures are shown for a U_{SL} of 2 cm/s. The trend is as expected and was previously explained by Maron et al. [13].

Figure 22 includes sketches of the velocity profiles at various points in the liquid film. From point E to U in that figure the pressure gradient decreases and so does the interfacial shear stress. To match the same liquid flow rate, the film thickness, and thereby the holdup, would increase. For further increase in the thickness, the film has to accommodate up-flow with recirculation as shown in the velocity profile between U and C. Due to the recirculation a part of the film would travel down and therefore to maintain the same liquid flow rate, a higher interfacial shear stress than the one at U would be required.

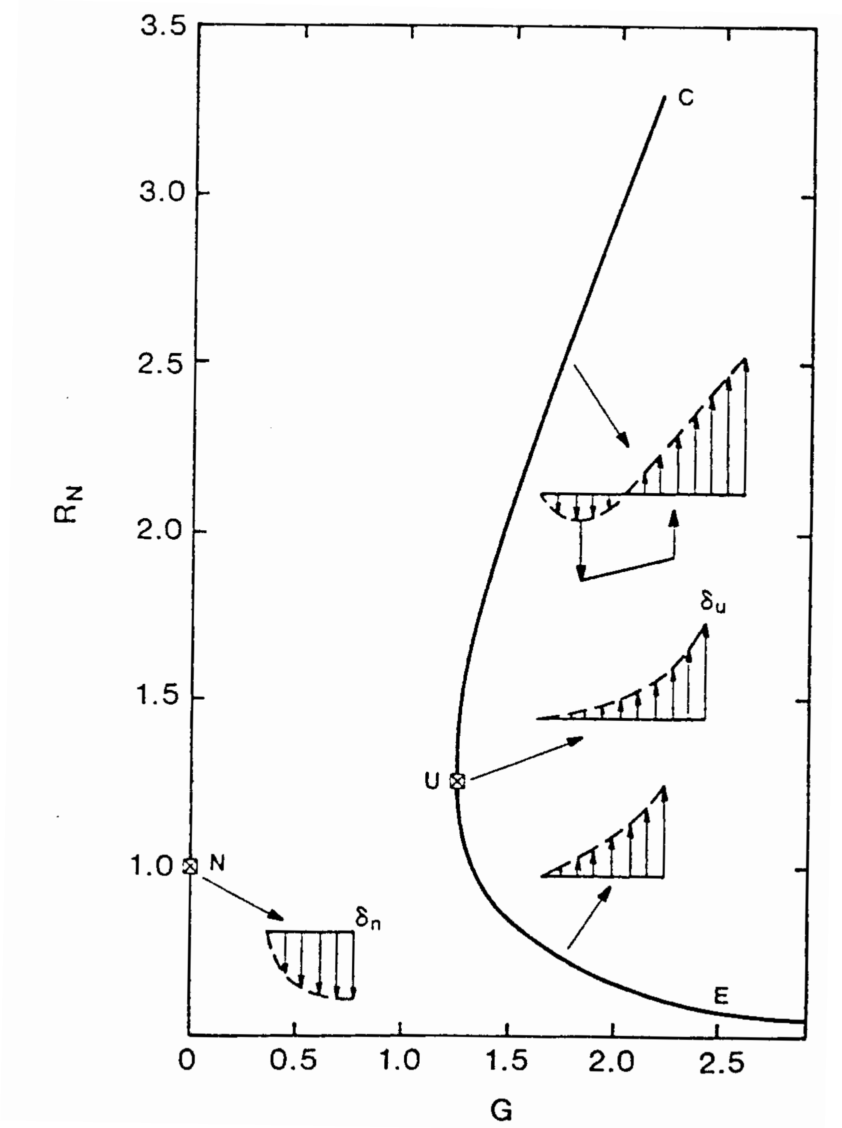

Figure 22: Variation of dimensionless film thickness (R_N) with dimensionless interfacial shear stress (G) [12]*. The increase in the interfacial shear stress (or pressure gradient) from point U to C is to accommodate the negative velocities within the profile to match the liquid flow rate.*

The relation between the holdup and the superficial gas velocity is straightforward. To make the film thinner, the gas flow rate should be increased; the trend of the thickness of the velocity profile can be seen for points C to U to E in Figure 22. The same behaviour is found in Figure 24, which shows how the holdup decreases with increasing superficial gas velocity. Figure 23 shows the pressure gradient against the superficial gas velocity. The observed trends are as expected based on the findings from Figure 22 and Figure 24.

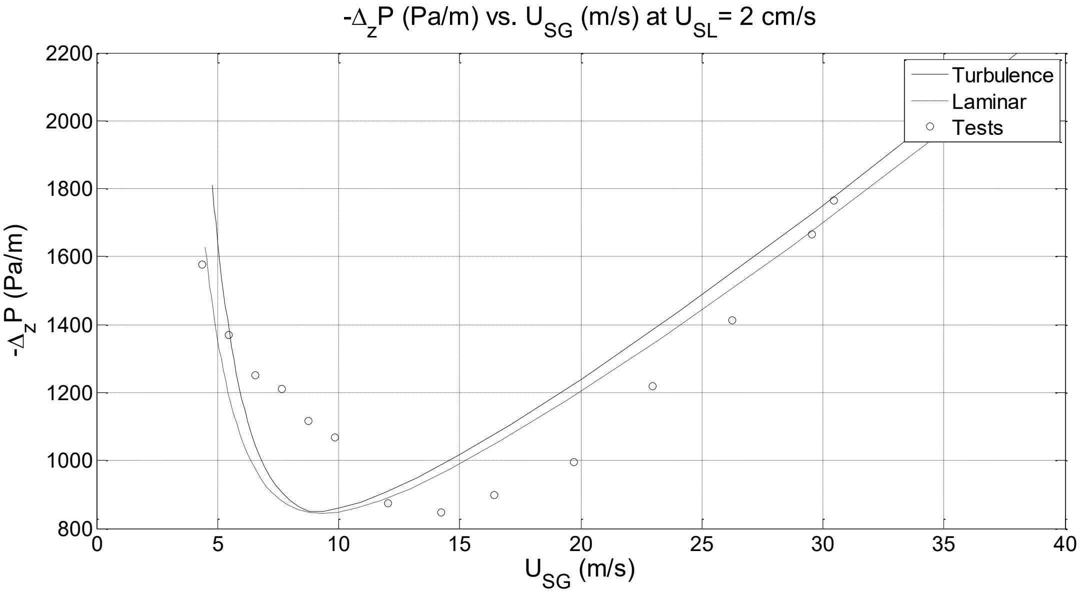

Figure 24: Pressure gradient versus superficial gas velocity. The model performance for two different velocity profile closures are shown for U_{SL}= 2 cm/s.

It was found that applied closure for the turbulence velocity profile was the best one in matching the obtained experimental results. In the next chapters the model will include this sub-model, unless explicitly described differently.

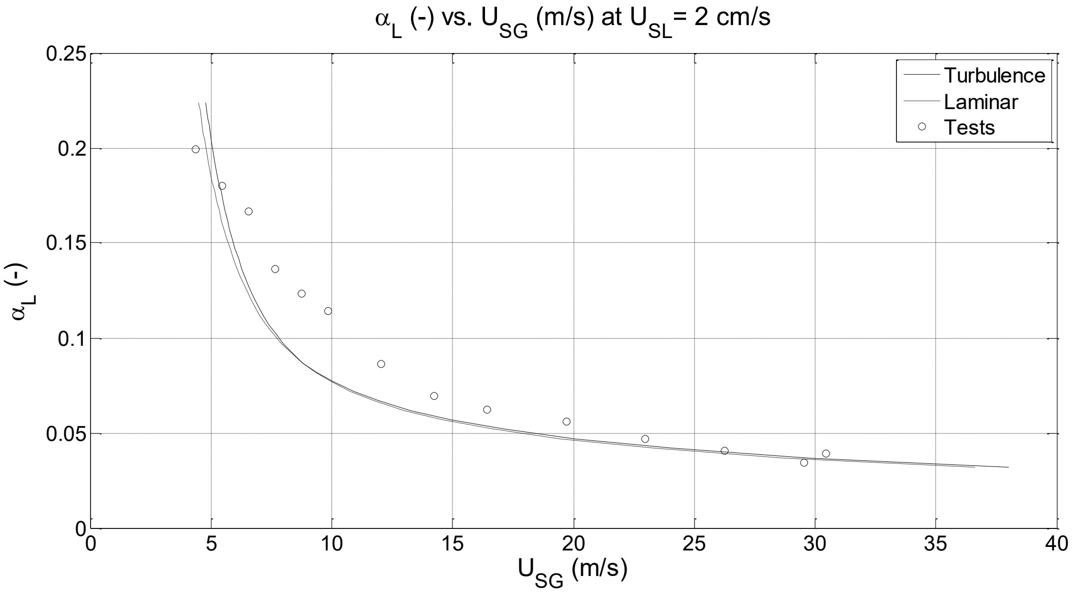

Figure 23: Holdup versus superficial gas velocity. The model performance under two different velocity profile closures are shown for U_{SL} = 2 cm/s. The film becomes thinner with increasing gas flow rate. Thus, we see a decreasing holdup against an increasing superficial gas velocity.

7.2. Model predictions versus experiments

The model was successful in capturing the experiment results (Figure 25) at higher superficial liquid velocities. The observations and anomalies noticed are:

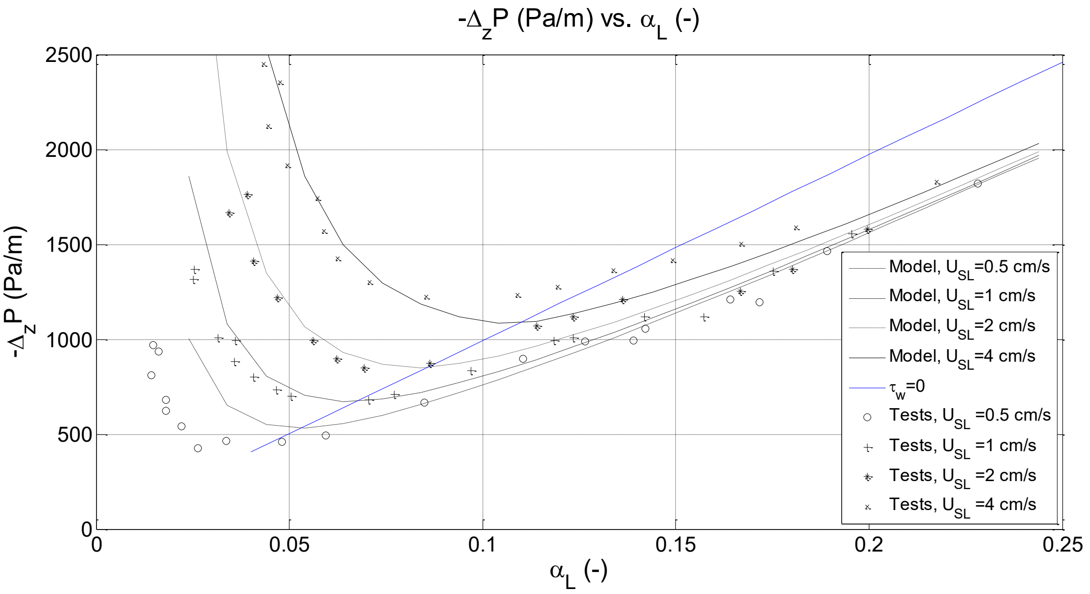

Figure 25: Pressure gradient versus. holdup for the modelling and experimental results at different superficial liquid velocities. The annular regime (lower holdups) is well captured by the model, except for the lowest superficial liquid velocity ($U_{SL} = 0.5\ cm/s$).

- At the highest U_{SL} of 4 cm/s the model starts to underpredict the experimental results tests near the churn regime, i.e. where the higher holdups are found. The underprediction is also noticed, though at significantly lower levels, for lower U_{SL}.
- At the lowest U_{SL} of 0.5 cm/s, the model overpredicts the experimental results. One of the possible reasons could be the partial dry-out, i.e., the walls of the tubes were not wetted completely during the experiments. During dry-outs, the walls become smooth and offers zero roughness due to the absence of waves – hence this reduces the pressure gradient.
- Zabaras et al. [12] showed similar results for their model for vertical upward gas-liquid annular flow in an 50.8 mm cylindrical pipe (Figure 26). The experiments were seen to match the model at higher gas velocities or lower mean film thicknesses ($\bar{\delta}$)/holdups. When the conditions approached the flooding point, however, the experiments started to follow the locus of U points. These U points correspond to the flow conditions where the wall shear stress (τ_w) becomes zero (Figure 22). The blue line in Figure 25 also represents the locus where the wall shear stress becomes zero. In comparison to the experiments obtained by Zabaras et al., our experimental results deviate from this locus. One of the possible reasons could be the difference in the flow conditions: free flow in the experiments by Zabaras et al. and co-current flow in our experiments, as discussed in sec. 2.6.

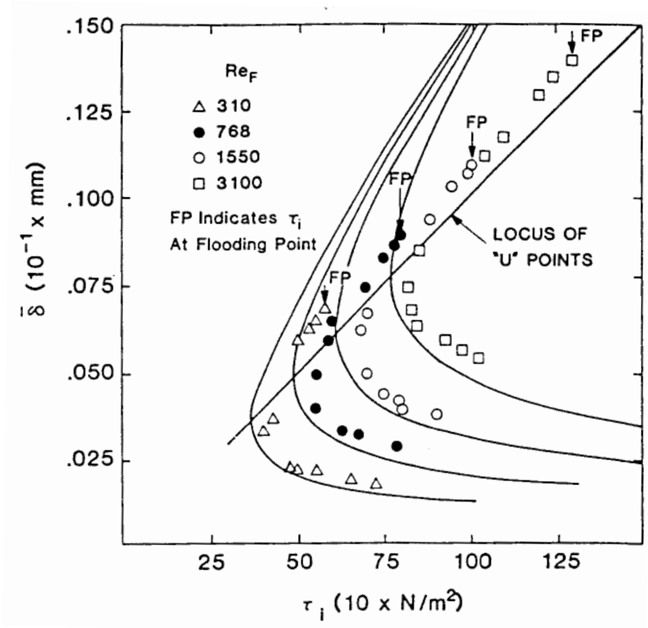

Figure 26: Mean film thickness versus the interfacial shear stress for the predictions with the Zabaras model versus the experimental results [12]. *The experimental results follow the location of the U points, and the model predictions do not, at higher values of the mean film thickness.*

A similar performance is found for the remaining parameter comparisons, which is shown in Appendix C: Holdup versus gas velocity.

7.3. Film distribution performance

The distribution of liquid flow rates in annular flows was discussed in sec. 2.8. The characterisation of the flow in an annulus includes the distribution of the liquid flow among the inner and outer films. The sensitivity of the model predictions for the pressure drop and holdup against this distribution needs to be investigated.

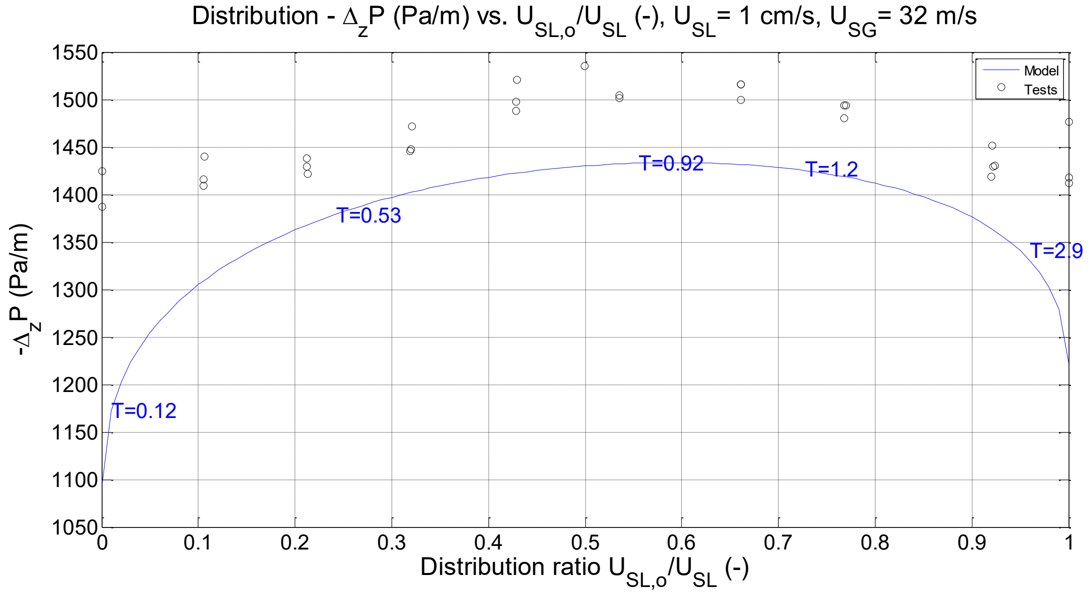

Figure 27: Pressure gradient versus the distribution ratio for the model predictions and the experiments at a $U_{SL} = 1\ cm/s$ and $U_{SG} = 31\ m/s$. The values of the model parameter, T, are specified at various locations near the model.

The distribution ratio ($=\frac{U_{SL,o}}{U_{SL}}$) is defined as the fraction of the liquid injected along the outer pipe out of the total liquid input. Figure 27 shows the pressure gradient versus the distribution ratio graph for the model with a Wallis interfacial friction factor correlation with a pre-factor of 600 (eq. (17)) at the highest superficial gas velocity of 32 m/s, for which the least mixing between the films occur. At the extreme ratios, the pressure gradient decreases as one of the walls becomes dry and will therefore no longer provide a roughness in the form of waves at the interface to the gas core. The model predictions do not precisely match the experiments. To further analyse the model the following can be done:

- The experiments should be reproduced better by the equipment. With the current fluctuations in the flow rates in the equipment one might not be able to reproduce results within a resolution of 5 Pa/m.
- Pressure sensors with better accuracy should be used in the experiments.
- The test facility should be upgraded for the use of higher gas (sec. 2.8) and liquid velocities.

Figure 28 shows the holdup variations against the distribution ratio. The performance is similar to what has been discussed above. The model shows a peak near a distribution ratio of 0.60 since the same volume of liquid occupies different film thicknesses on the inner and outer pipes because of the difference in diameters. It also interesting to see the performance of the models at lower gas velocities, which will be discussed in Appendix E: Film distribution.

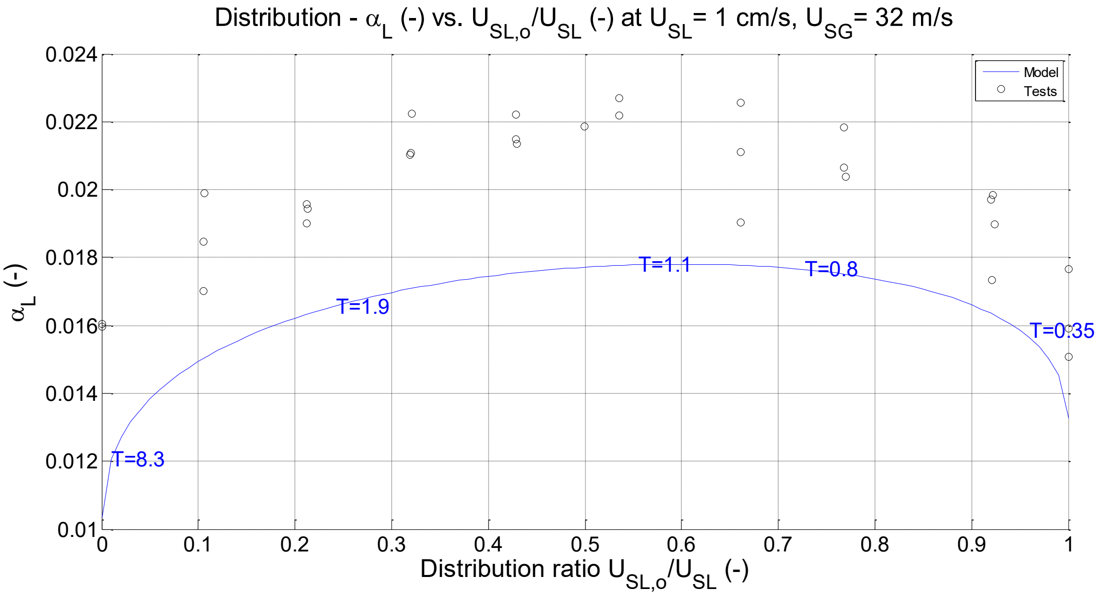

Figure 28: Holdup versus distribution ratio for the model predictions and the experiments at a $U_{SL} = 1\ cm/s$ and $U_{SG} = 31\ m/s$.

8. Modelling of the eccentricity

8.1. Introduction

The modelling discussed in the previous chapters focused on a concentric annulus. During natural gas production, however, we rarely encounter cases of perfectly concentric annuli for extraction. This chapter attempts to modify the previously defined model for eccentric cases.

8.2. Eccentricity

The eccentricity of an annulus is defined as:

$$e = \frac{E}{\frac{D_o - D_i}{2}} \tag{22}$$

where E is the distance between the centre of the outer pipe and the centre of the inner pipe. The maximum possible displacement is $\frac{D_o - D_i}{2}$, which corresponds to a fully eccentric pipe. Figure 29 shows a few possible configurations for an annulus. Note that E in eq. (22) is equal to the DBC in Figure 29.

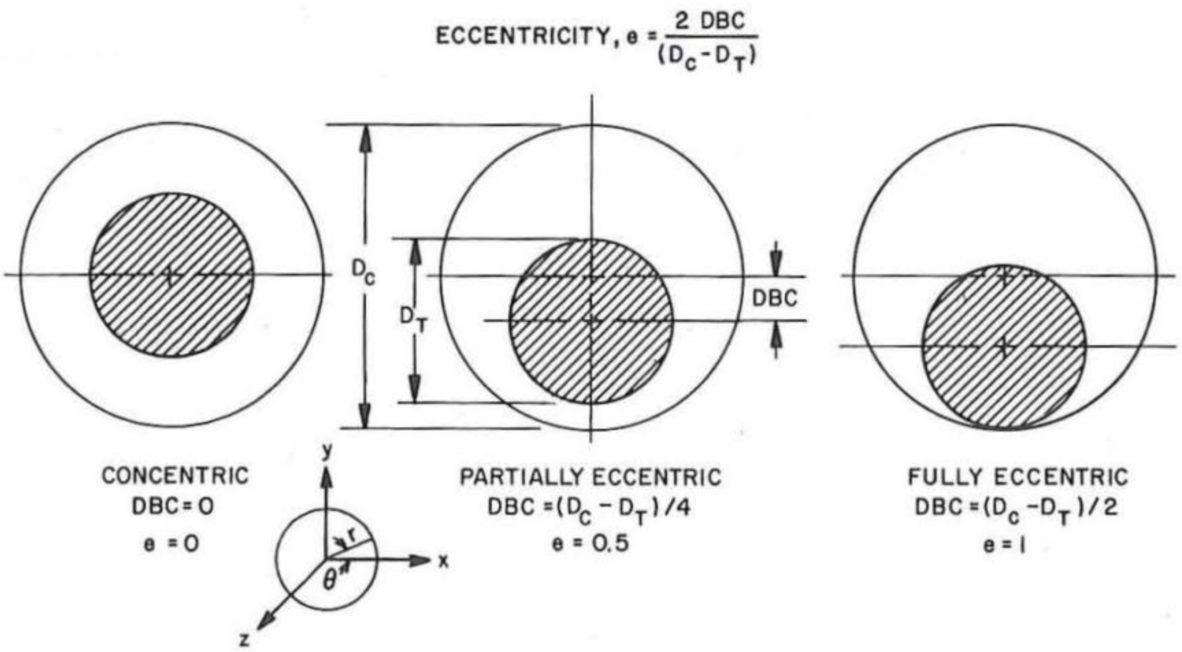

Figure 29: Annulus configurations [7]. *The eccentricity varies between 0 for a concentric annulus to 1 for a fully eccentric annulus.*

8.3. Modelling modifications – geometry

The primary difference which has to be accommodated for eccentricity is the variation in the geometrical parameters which is explained in Figure 30. For instance, consider the gas core force balance for the concentric annulus, as given below:

$$PA_c - (P + dP)A_c - \tau_{ii}S_{ii}dz - \tau_{io}S_{io}dz - \rho_G g A_c dz = 0$$

The momentum balance equation assumes a constant interfacial shear stress around the interfacial film circumferences. In eccentric annuli, due to the lack of symmetry, the gap between the films would vary, and hence the effective 'local' core area would also vary. This would also

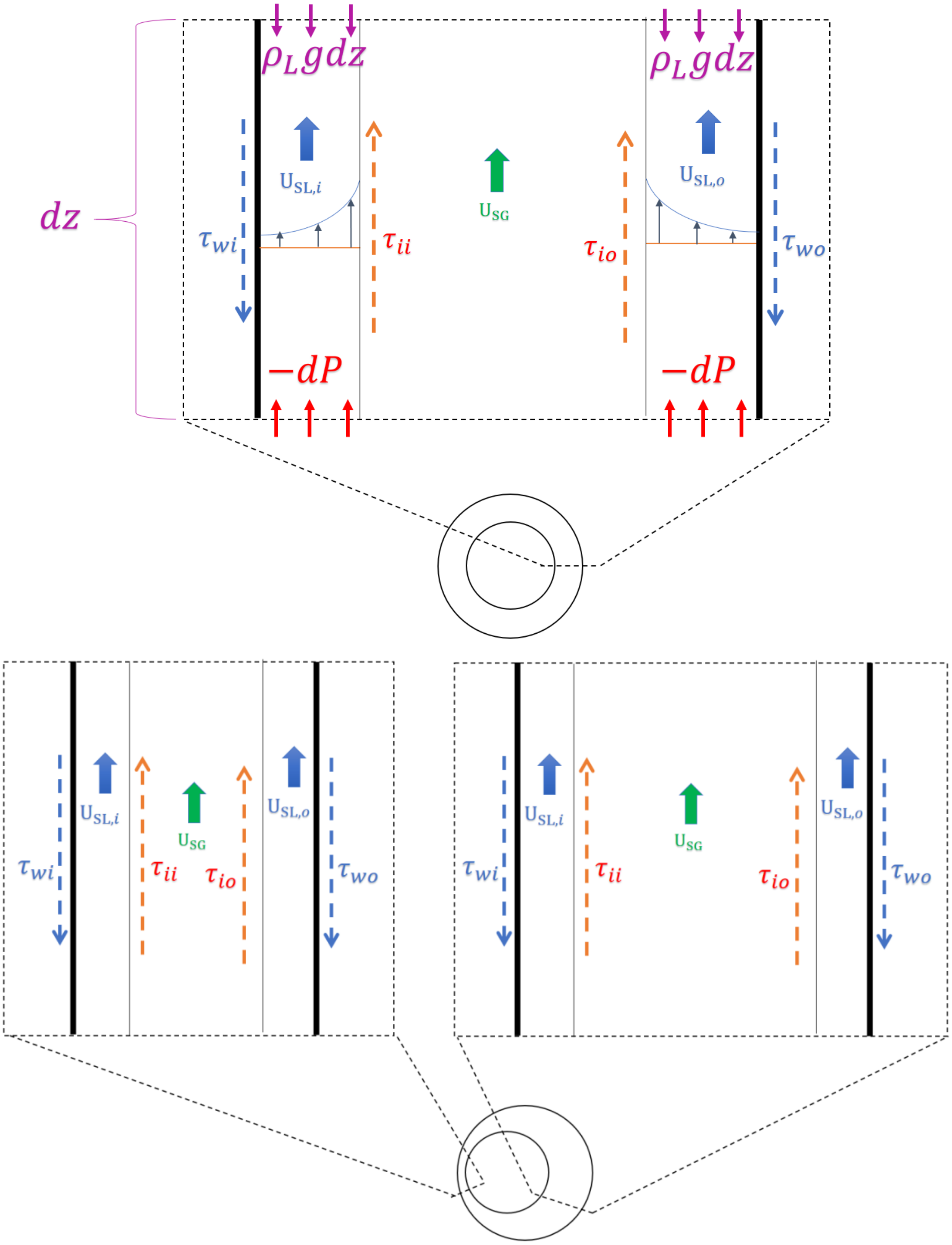

Figure 30: The modelling for the concentric case is summarized at the top. The modelling for the eccentric one is shown at the bottom. The variation in the 'local' geometric parameters like hydraulic diameter, core area, etc. for the eccentric annuli requires a model modification.

impose a shear stress distribution instead of a constant shear stress as in the case of concentric annuli. Hence the above force balance cannot be justified for an eccentric case, and this thus requires modification. As a first step for a one-dimensional modelling, instead of a CFD approach, is to conceive an eccentric annulus in the form of many flow cells or grid cells as shown in the figure below [29].

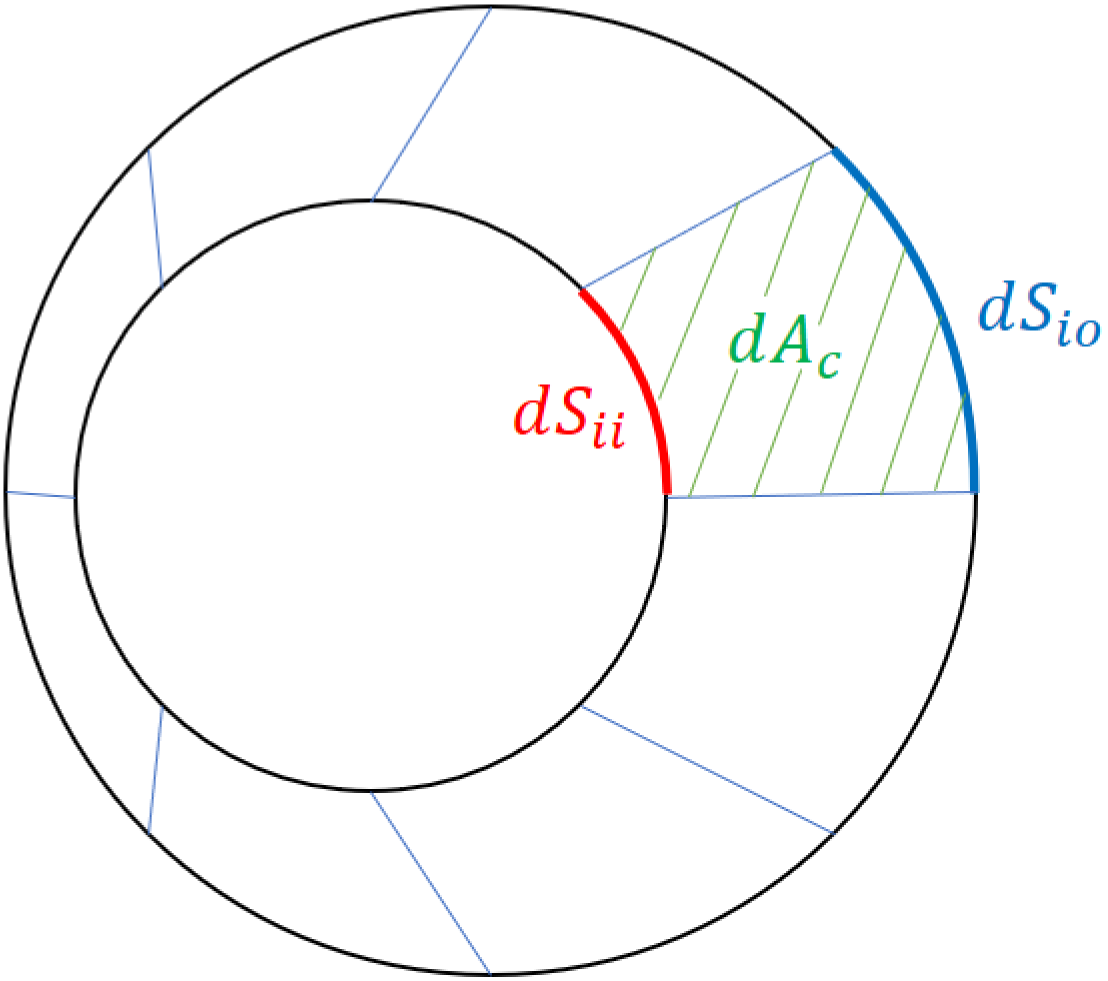

Figure 31: An eccentric annulus is divided into many flow cells or grid cells. Each flow cell is treated individually and is assumed to have constant stresses. The various flow parameters like flow rates are then integrated across all the grid cells to arrive at the total flow rate.

A grid can be considered as an area where liquid flow occurs between two parallel plates driven by a pressure gradient. The grid cells can be constructed in different ways. For simplicity, the outer and inner walls are divided into a certain number of cells (n_g), and the end points of the dividing circumferences (dS_{ii} or dS_{io}) are connected in a hierarchy to form grid core areas (dA_c). The modelling equations can now be modified, as is shown in Table 3. The following assumptions are considered for a grid cell:

- Constant shear stress along the walls and the film interfaces.

- Constant film thicknesses.
- Negligible shear stresses or other influences between the grid cells.

Table 3: Comparison of modelling equations between a concentric annulus and a grid cell of an eccentric annulus. It is shown that all modifications are due to the change in geometric definitions.

	Concentric (constant)	**Eccentric (for the grid)**
Inner interfacial shear stress	$\tau_{\mathrm{ii}} = \frac{\left(\left[-\frac{dP}{dz}\right] - \rho_G g\right) A_c}{\mathrm{K}_0 S_{io} + S_{ii}}$	$\tau_{\mathrm{iig}} = \frac{\left(\left[-\frac{dP}{dz}\right] - \rho_G g\right) dA_c}{\mathrm{K}_{0\mathrm{g}} dS_{io} + dS_{ii}}$
Outer interfacial shear stress	$\tau_{\mathrm{io}} = \mathrm{K}_0 \tau_{ii}$	$\tau_{\mathrm{iog}} = \mathrm{K}_{0\mathrm{g}} \tau_{iig}$
Outer wall shear stress	$\tau_{wo} = \frac{\left(\left[-\frac{dP}{dz}\right] - \rho_L g\right) A_{fo} + \tau_{io} S_{io}}{S_{wo}}$	$\tau_{wog} = \frac{\left(\left[-\frac{dP}{dz}\right] - \rho_L g\right) dA_{fo} + \tau_{iog} dS_{io}}{dS_{wo}}$
Inner wall shear stress	$\tau_{wi} = \frac{\left[\left(\left[-\frac{dP}{dz}\right] - \rho_L g\right) A_{fi} + \tau_{ii} S_{ii}\right]}{S_{wi}}$	$\tau_{wig} = \frac{\left[\left(\left[-\frac{dP}{dz}\right] - \rho_L g\right) dA_{fi} + \tau_{iig} dS_{ii}\right]}{dS_{wi}}$
Hydraulic diameter	$D_h = \frac{4A_c}{S_{wo} + S_{wi}} = D_o - D_i$	$D_{hg} = \frac{4dA_c}{dS_{wo} + dS_{wi}}$
Film thickness ratio	$T = \frac{\delta_{fi}}{\delta_{fo}}$	$T_g = \frac{\delta_{fig}}{\delta_{fog}}$
Second model parameter	$K_0 = \frac{f_{io}}{f_{ii}}$	$K_{0g} = \frac{f_{iog}}{f_{iig}}$

8.4. Modelling modifications – film thickness variation

Sec. 2.8 discussed the film thickness ratio which can be achieved in an annulus. Appendix A: Sub-model for film thickness ratio defined a sub-model which includes the ratio of the mean film thicknesses, T, and also the thickness variation around the circumference (Figure 41). It was

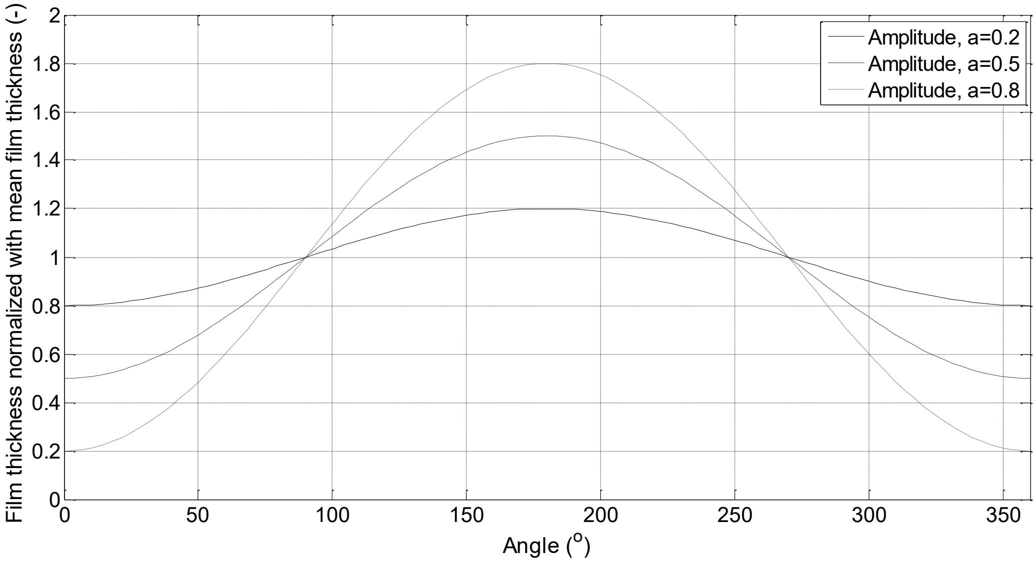

Figure 32: Film thickness variation around the circumference of the films as a function of the eccentricity. A sine wave function was used for simplicity (Figure 41).

decided to incorporate a function to vary the film thickness around the circumference while maintaining a constant mean film thickness ratio of $T = 1$. Hence the assumption of a constant film thickness that we initially considered in the model for (sec. 6.1) will be abandoned. For simplicity a sine wave with a constant $(= 1)$ offset (with a positive minimum) would be used for both the films. The amplitude (a) of the wave determines the sharpness of the distribution, i.e., the difference between the maximum and minimum in the film (Figure 33) – with higher amplitudes for higher eccentricities. The amplitude is varied to suitably fit the experimental results. To summarize, the following new additional closures are imposed:

- Same amplitude for both the films.
- Amplitude increased with eccentricity to fit the experiments.
- Amplitude varied also as function of holdup, which will be discussed in sec. 9.2.

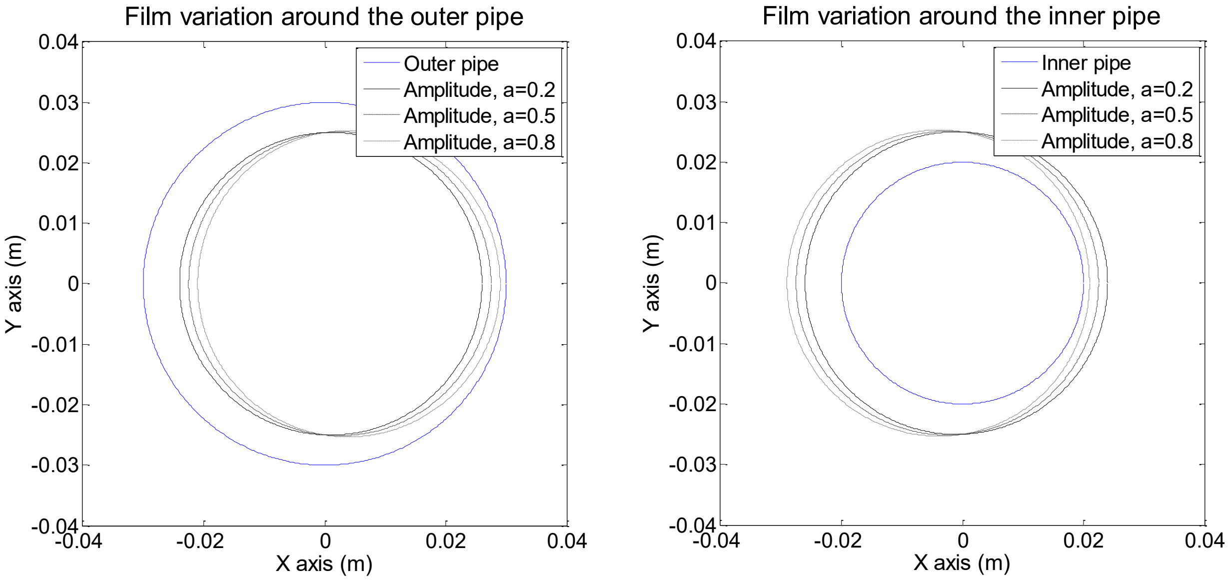

Figure 33: Depiction of film thickness variation around the circumference of the pipe. An exaggerated mean film thickness of 5 mm is considered for $D_o = 60\ mm$ and $D_i = 40\ mm$ for clarity. With increasing amplitude, the film in the wide gap (near the right side of the pipe) becomes thicker and the film in the narrow gap (near the left side of the pipe) becomes thinner.

9. Results – Part 2

Three primary graphs for the results in a vertical eccentric annulus with an outer diameter, $D_o = 60\ mm$, and an inner diameter, $D_i = 40\ mm$, will be presented:

- Pressure gradient versus holdup ($-\Delta_z P$ (Pa/m) vs. α_L (-)) – from the liquid sub-model.
- Holdup versus superficial gas velocity (α_L (-) vs. U_{SG} (m/s)) – from the full model.
- Pressure gradient versus superficial gas velocity ($-\Delta_z P$ (Pa/m) vs. U_{SG} (m/s)) – from the full model.

9.1. Modelling results

The modifications made to the modelling to accommodate eccentricity was discussed in the previous chapter and the results are given below.

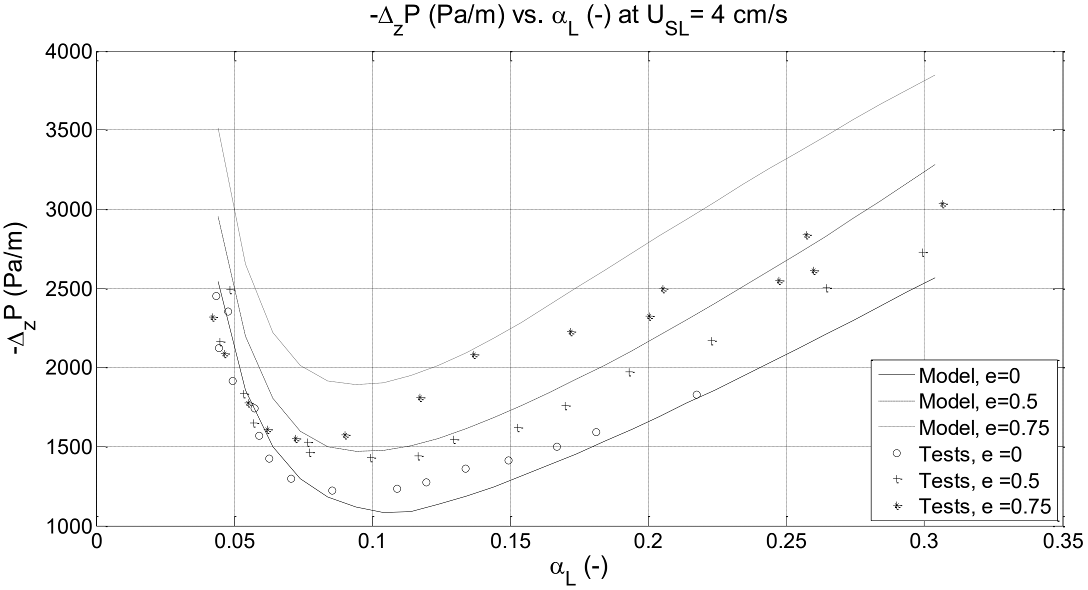

Figure 34: Pressure gradient versus holdup. The model performance of three different eccentricities are shown for a U_{SL} of 4 cm/s. The model is overpredicting the results near the annular regime (lowest holdups) and far into the churn regime (highest holdups).

The main observations are:

- The model was fitted by varying the amplitude, a, hence forming a closure.
- The model overpredicts the results at the highest and lowest holdups, and this will be discussed in the next sub-section.
- Figure 35 and Figure 36 show the results for the full model. The interfacial friction factor discussed in sec. 6.6.2 was used here.

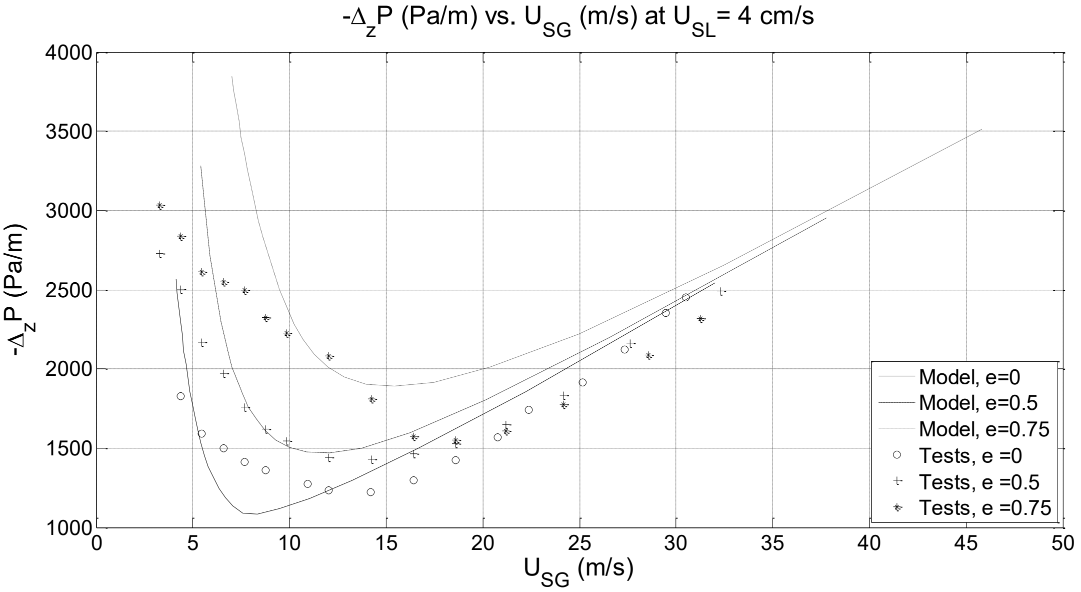

Figure 36: Pressure gradient versus superficial gas velocity. The model performance of three different eccentricities are shown for a U_{SL} of 4 cm/s.

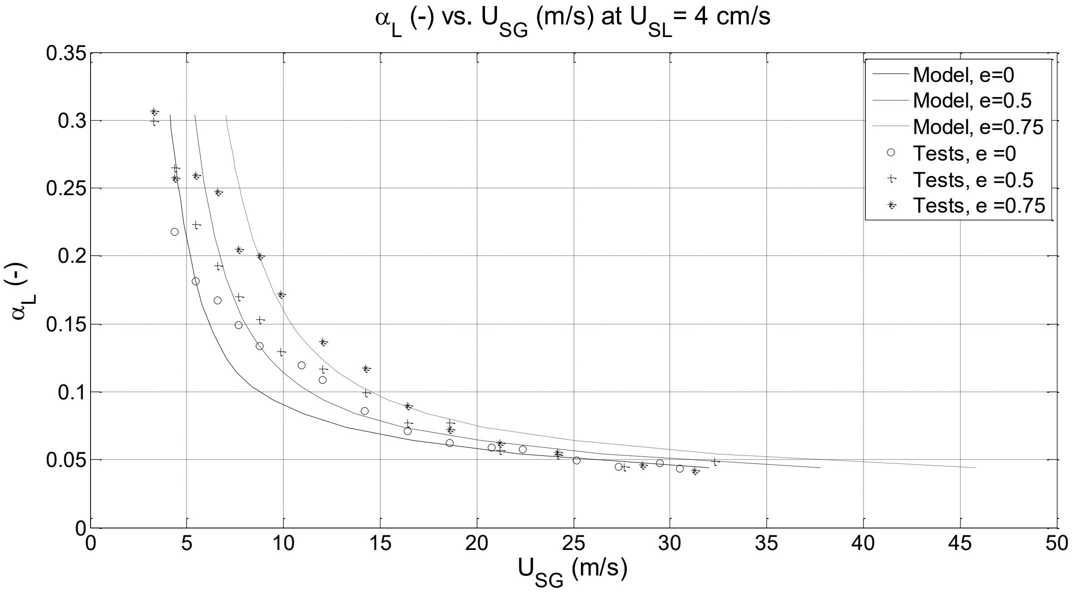

Figure 35: Superficial gas velocity versus holdup. The model performance of three different eccentricities are shown for a U_{SL} of 4 cm/s.

9.2. Amplitude study

Figure 34 shows that the model was successful in predicting the pressure gradient as a function of holdup and eccentricity. The additions in the model to accommodate eccentricity are the geometric or gird considerations (sec. 8.3) and a closure for the film variation (sec. 8.4). The exact amplitude, a, forming part of the film variation, was determined based on obtaining the best fit with the experiments.

However, for the highest and the lowest holdups we see a deviation between the model predictions and the experimental results. Therefore, it is worthwhile to see how the amplitude should be varied exactly to fit the curves. An attempt was made to see the amplitude 'demanded' by the experimental points for the model to match. Out of the many trial and errors, it was found that the calculated amplitude showed the best correlation for the holdup. Figure 37 shows the reverse-calculated amplitude against the holdup for all the considered U_{SL} values for an eccentricity of 0.75. The following observations can be made:

- The variation of the amplitude with the holdup is not a strong function of U_{SL}.
- The lowest amplitude is seen near the smallest holdup values (or the highest superficial gas velocities). One of the possible reasons could be the lower atomization and deposition rates as discussed in sec. 2.8 which could account for the delayed amplitude build-up.
- The maximum amplitude is noticed near a holdup of 0.125 – which is close to the liquid loading point or the start of the transition to churn flow. After the maximum the flow regime moves to the churn pattern where the movement of fluid starts to become chaotic and starts to 'lose information' about the amplitude.
- A negative amplitude is calculated at the lowest holdups, which is unphysical. However, the model was already overpredicting the pressure gradient slightly for the concentric case due to the choice of the turbulence correlations and other closures (Figure 25). Therefore, for the model to match the experimental results a negative amplitude was demanded. With a better investigation of the closures, a physically viable variation of amplitude can be derived.

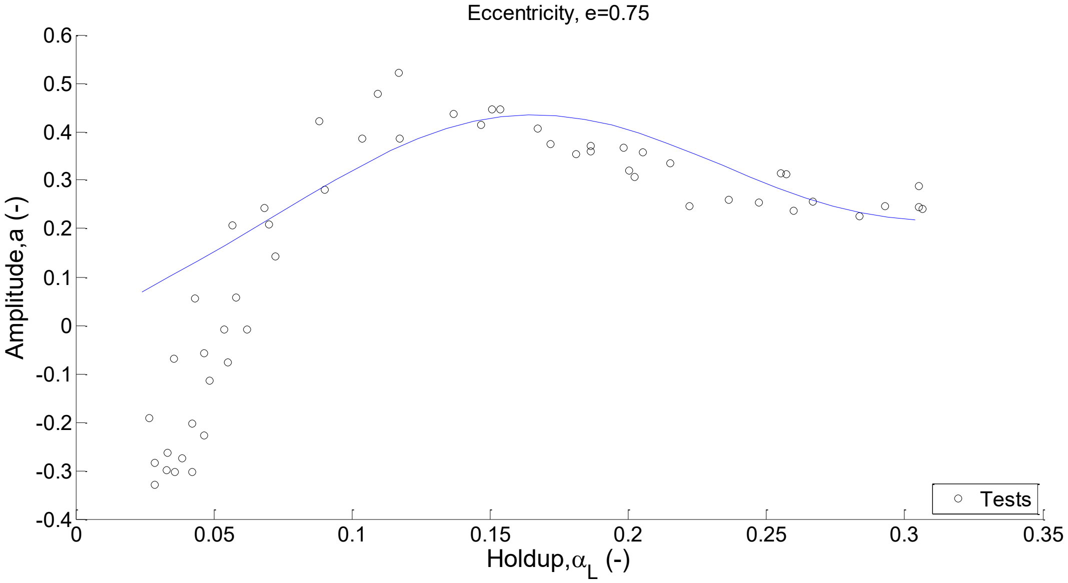

Figure 37: Amplitude (reverse-calculated from the model to match the tests) versus holdup. The blue line is a fit to the experimental results.

A realistic function fit was made for the results in Figure 37 (blue line). An amplitude function is imposed in the model and its performance is shown in Figure 38. Using the new amplitude function, the model gives a better prediction of the pressure.

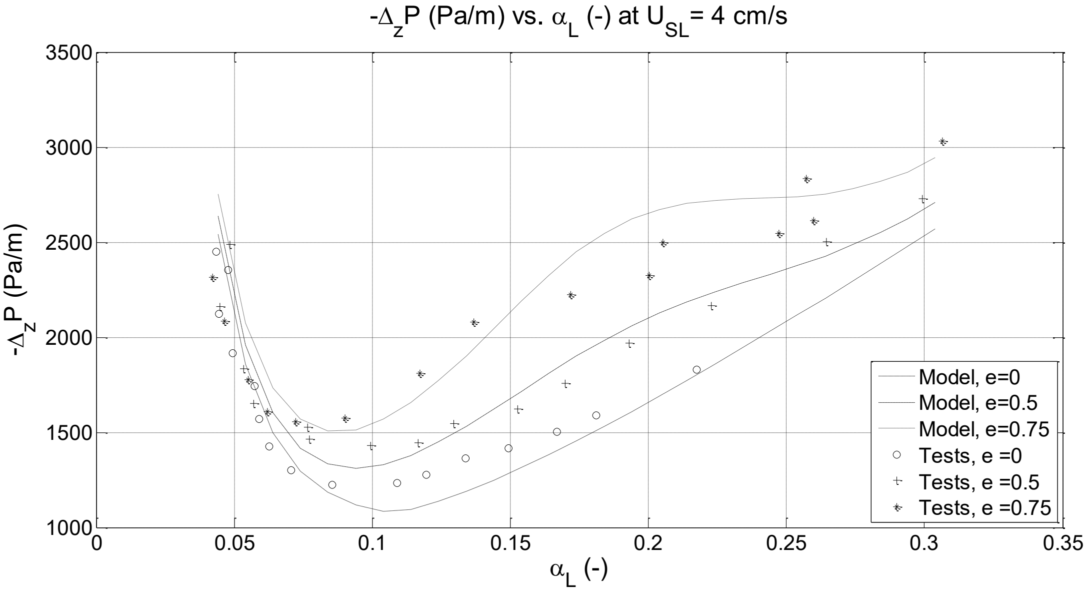

Figure 38: Pressure gradient versus holdup with the new amplitude function. The model is now better predicting the pressure gradient in comparison to Figure 34 at the extreme holdups.

10. Conclusions and recommendations

In the present Master Thesis project experiments were carried out for the upward air-water flow in the annulus of a small-scale vertical flow loop in the TNO lab in Delft. Furthermore, a flow model was developed, and the model predictions were compared with the new experiments.

From the combined experimental/modelling study the following conclusions can be drawn:

- The model was able to predict the pressure gradient and holdup for a range of superficial gas and liquid velocities, using different eccentricities in the annulus configuration. The model predicted the pressure gradient within 10% of the experimental values at high superficial liquid velocities (>0.5 cm/s). However, for a superficial liquid velocity of 0.5 cm/s, the model was overpredicting the pressure drop by 100%, which could be attributed to the partial dry-out on the tube walls.
- To determine the superficial gas velocity, for a given pressure drop and holdup, a modified version of the Wallis correlation was used for the interfacial friction factor. The gas velocity was predicted within 5 to 10% at low holdups (<0.075). For higher holdups the gas velocity was overpredicted by about 40%. The accuracy of the model can be improved by testing different closures for the turbulence sub-model and for the interfacial friction factor.
- The primary modifications made to the model for the eccentric cases are based on applying a number of grid cells along the circular film (sec. 8.3) allowing for the inclusion of a closure for the variation of the circular film thickness both at the inner and at the outer pipe wall (sec. 8.4). A verification of the closure for the amplitude (a) or of the closure of the film thickness is required to confirm the dependency between the eccentricity, the film amplitude, and the holdup. However, with the applied closure for the amplitude, the prediction of the pressure gradient is within 6% accuracy for the eccentric cases.
- The pressure gradient and holdup of an annulus is only a weak function of the film thickness ratio T (sec. 7.3) for most of the values for this ratio ($0.4 < T < 3$). For simplicity a value $T = 1$ is used. Based on this finding, the flow modelling in an annulus does not seem to require a closure for the film thickness ratio.

The following recommendations can be made for further research on the multiphase flow in an annulus:

- During the natural gas extraction, the flow will obtain a fully developed state for most of its transport from the reservoir to the surface. To mimic the same behaviour, researchers use long setups – as high as 13.7 m [7] – to ensure that the measuring stations are far from the injection points. Therefore, for a better understanding of the flow in an annulus longer setups than used in the present study should be preferred, especially to verify the sub-models for the film thickness ratio (Appendix A: Sub-model for film thickness ratio).
- The modelling explained in this report assumes that the films are spread across the circumferences of the tubes without any gap or dry-outs. In the experiments, however, we encountered cases, especially at low liquid and high gas flow rates, where the liquid is smeared only on a part of the tube. This could expose the tube wall to the gas directly which could result in very low ‘interfacial’ shear stress, which in turn will affect the

modelling. A closer look at this effect could help to improve the model performance at low superficial liquid velocities.

- The dry gas used in the experiments was stored in tanks compressed at 6 to 7 bar, with constant new supply using a compressor. The superficial gas velocity U_{SG} required for the experiments was sufficiently stable. The water, however, was taken from the lab tap which was subjected to variations in conditions as the source was used for multiple purposes. Though the output was controlled by the flowmeters, it strongly depended on the inlet pressure and the flow rates were only just stable enough. These uncertainties might have affected some of the experiments. In future, liquid supplied from tanks with a constant pressure can better equip the experimentalist to control the superficial liquid velocity U_{SL}.
- It is recommended to use film thickness measurement sensors in the experiments. As explained in sec. 2.8 the primary parameter in the modelling for the two-phase flow in an annulus is the film thickness ratio, T. A closure in the model for the film variation around the circumference was also developed to accommodate the eccentricity in the modelling. Therefore, it would be meaningful to invest in equipment measuring the film thickness of the inner and outer tubes separately. The various film thickness measurement techniques available were discussed by Clark [23], [30].

Bibliography

[1] "The Paris Agreement | UNFCCC." [Online]. Available: https://unfccc.int/process-and-meetings/the-paris-agreement/the-paris-agreement. [Accessed: 01-Sep-2018].

[2] J. Speight, *Origin and Properties of Natural Gas*, 2007.

[3] J. Speight, *Origin and Production of Natural Gas*, 2007.

[4] R. V. A. Oliemans, *Applied Multiphase Flow*. 2001.

[5] Z. J. G. Gromotka, "The Stability Region of the Tubing Performance Relation Curve."

[6] A. T. van Nimwegen, L. M. Portela, and R. A. W. M. Henkes, "Modelling of upwards gas-liquid annular and churn flow with surfactants in vertical pipes," *Int. J. Multiph. Flow*, vol. 105, pp. 1–14, 2018.

[7] E. F. Caetano, O. Shoham, and J. P. Brill, "Upward vertical two-phase flow through an annulus—Part I: Single-phase friction factor, Taylor bubble rise velocity, and flow pattern prediction," *J. Energy Resour. Technol.*, vol. 114, no. 1, p. 1, 1992.

[8] A. C. V. M. Lage and R. W. Time, "Mechanistic model for upward two-phase flow in annuli," *SPE Annu. Tech. Conf. Exhib.*, no. 1, pp. 1–11, 2000.

[9] G. Das, P. K. Das, N. K. Purohit, and A. K. Mitra, "Gas liquid upflow througl vertical concentric annuli — Part I : Experimental," *J. Fluids Eng. ASME*, vol. 121, no. December 1999, pp. 2–8, 1999.

[10] W. H. Henstock and T. J. Hanratty, "The interfacial drag and the height of the wall layer in annular flows," *AIChE J.*, vol. 22, no. 6, pp. 990–1000, 1976.

[11] E. F. Caetano, O. Shoham, and J. P. Brill, "Upward vertical two-phase flow through an annulus—Part II: Modeling bubble, slug, and annular Flow," *J. Energy Resour. Technol.*, vol. 114, no. 1, p. 14, 1992.

[12] G. Zabaras, A. E. Dukler, and D. Moalem-Maron, "Vertical upward cocurrent gas-liquid annular flow," *AIChE J.*, vol. 32, no. 5, pp. 829–843, 1986.

[13] D. Moalem Maron and A. E. Dukler, "Flooding and upward film flow in vertical tubes-II. Speculations on film flow mechanisms," *Int. J. Multiph. Flow*, vol. 10, no. 5, pp. 599–621, 1984.

[14] H. J. Richter, "Flooding in tubes and annuli," *Int. J. Multiph. Flow*, vol. 7, no. 6, pp. 647–658, 1981.

[15] A. E. Dukler, L. Smith, and A. Chopra, "Flooding and upward film flow in tubes-I. Experimental studies," *Int. J. Multiph. Flow*, vol. 10, no. 5, pp. 585–597, 1984.

[16] V. C. Kelessidis and A. E. Dukler, "Modeling flow pattern transitions for upward gas-liquid flow in vertical concentric and eccentric annuli," *Int. J. Multiph. Flow*, vol. 15, no. 2, pp. 173–191, Apr. 1989.

[17] Y. Taitel and A. E. Dukler, "A model for predicting flow regime transitions in horizontal and near horizontal gas-liquid flow," *AIChE J.*, vol. 22, no. 1, pp. 47–55, 1976.

[18] G. Das, P. K. Das, N. K. Purohit, and a. K. Mitra, "Flow pattern transition during gas

liquid upflow through vertical concentric annuli—Part II: Mechanistic models," *J. Fluids Eng.*, vol. 121, no. 4, p. 902, 1999.

[19] B. Ozar, J. J. Jeong, A. Dixit, J. E. Juliá, T. Hibiki, and M. Ishii, "Flow structure of gas-liquid two-phase flow in an annulus," *Chem. Eng. Sci.*, vol. 63, no. 15, pp. 3998–4011, 2008.

[20] N. P. Ekberg, S. M. Ghiaasiaan, S. I. Abdel-Khalik, M. Yoda, and S. M. Jeter, "Gas - liquid two-phase flow in narrow horizontal annuli," *Nucl. Eng. Des.*, vol. 192, no. 1, pp. 59–80, 1999.

[21] J. E. Julia, B. Ozar, A. Dixit, J.-J. Jeong, T. Hibiki, and M. Ishii, "Axial development of flow regime in adiabatic upward two-phase flow in a vertical annulus," *J. Fluids Eng.*, vol. 131, no. 2, p. 21302, 2009.

[22] B. Yin, X. Li, B. Sun, and H. Zhang, "Hydraulic model of steady state multiphase flow in wellbore annuli," *Pet. Explor. Dev.*, vol. 41, no. 3, pp. 399–407, 2014.

[23] D. Schubring and T. A. Shedd, "A model for pressure loss, film thickness, and entrained fraction for gas-liquid annular flow," *Int. J. Heat Fluid Flow*, vol. 32, no. 3, pp. 730–739, 2011.

[24] J. van 't Westende, "KIP Annulus Flow - liquid loading," TNO, 2628CA Delft, 2016.

[25] A. C. Ashwood, S. J. Vanden Hogen, M. A. Rodarte, C. R. Kopplin, D. J. Rodríguez, E. T. Hurlburt, and T. A. Shedd, "A multiphase, micro-scale PIV measurement technique for liquid film velocity measurements in annular two-phase flow," *Int. J. Multiph. Flow*, vol. 68, pp. 27–39, 2015.

[26] J. M. C. Van Westende, F. Vercauteren, and E. Nennie, "Modelling of churn-annular foam flows," *9th ICMF*, 2016.

[27] A. M. Aliyu, L. Lao, H. Yeung, and A. A. Almabrok, "A comparative analysis of interfacial friction factor correlations for adiabatic co - current gas – liquid annular two - phase flow in large diameter pipes," *Proc. World Congr. Mech. Chem. Mater. Eng. (MCM 2015)*, no. 280, pp. 280-1–9, 2015.

[28] L. B. Fore, S. G. Beus, and R. C. Bauer, "Interfacial friction in gas-liquid annular flow: Analogies to full and transition roughness," *Int. J. Multiph. Flow*, vol. 26, no. 11, pp. 1755–1769, 2000.

[29] J. M. Peden, "SPE 16692 Flow of drilling fluids through eccentric annuli," pp. 389–396, 1987.

[30] W. W. Clark, "Liquid film thickness measurement," *Multiph. Sci. Technol.*, vol. 14, no. 1, p. 74, 2002.

[31] C. Vuik, F. J. Vermolen, M. B. van Gijzen, and M. J. Vuik, *Numerical methods for ordinary differential equations*. .

[32] IRENA, *Global Energy Transformation - A roadmap to 2050*. 2018.

[33] O. Shoham, "Mechanistic modeling of gas liquid two phase flow in pipes," pp. 240–250, 2005.

Appendix A: Sub-model for film thickness ratio

Caetano et al. [11] have modelled the annular flow in annuli using the mass and momentum balances. The modelling in our report was also developed by using similar concepts. Although there are some important differences between the two, the attempt made by Caetano et al. to form a closure for the film thickness ratio, T, will be discussed in this appendix.

Caetano et al. have focussed on producing a model for predicting a fully developed flow. As such, the initial throughputs would become insignificant because of entrainment, atomization and deposition. That is, the liquid flow rates along the inner and outer walls will change significantly in a fully developed section when compared to the inlet flow rates. Therefore, for a fully developed flow the flow rates along the walls, and thereby the film thickness ratio, was

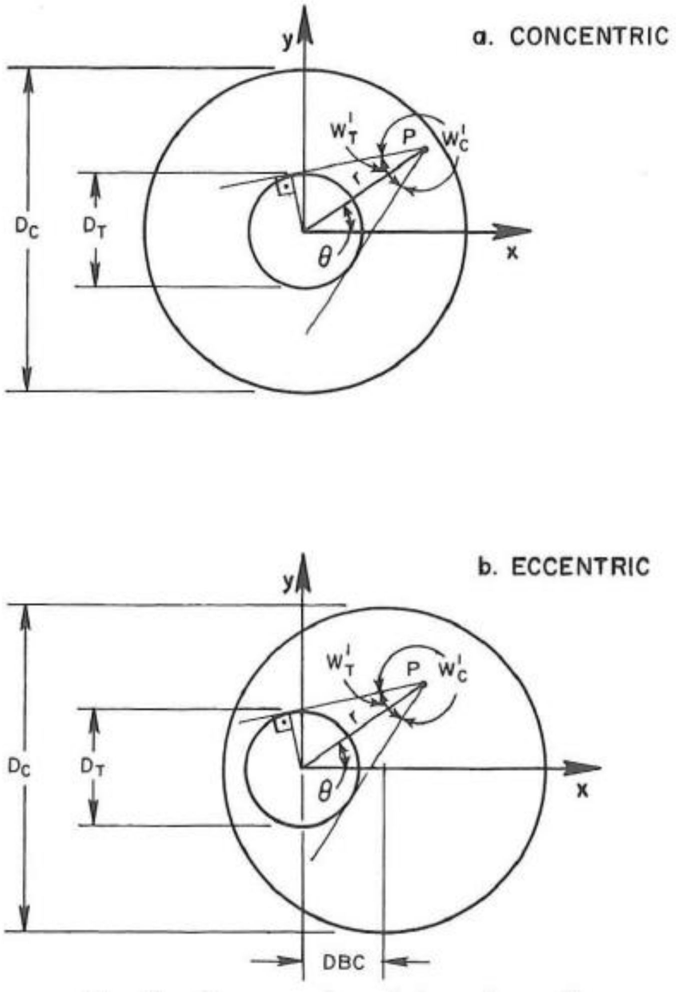

Figure 39: Planar angles of view for an annulus [11]. *The film thickness ratio as a function of the eccentricity and of the diameter ratio was derived.*

derived as a function of the eccentricity, e, and of the diameter ratio, K, based on the principles of entrainment, atomisation and deposition. The authors have described this as follows:

> *"A prediction for the ratio between the tubing (inner) film thickness and casing (outer) film thickness is developed by assuming equilibrium between the entrainment and deposition rates of liquid droplets. In this development it is also assumed that an isotropic scattering mechanism applies for the liquid droplets in the core. The droplets can travel in any direction in the core, remaining entrained or depositing in one of the two liquid films. (Figure 39,* [11]*)"*

Consider Figure 39. The deposition of a liquid particle at point P at either the inner or outer tube was considered to be proportional to the planar angle at which it is exposed. In addition to this, the atomisation from the film was taken proportional to its thickness and to the projected surface are on the wall. The final relation between the film thickness ratio, eccentricity and diameter ratio was derived and is depicted in Figure 40.

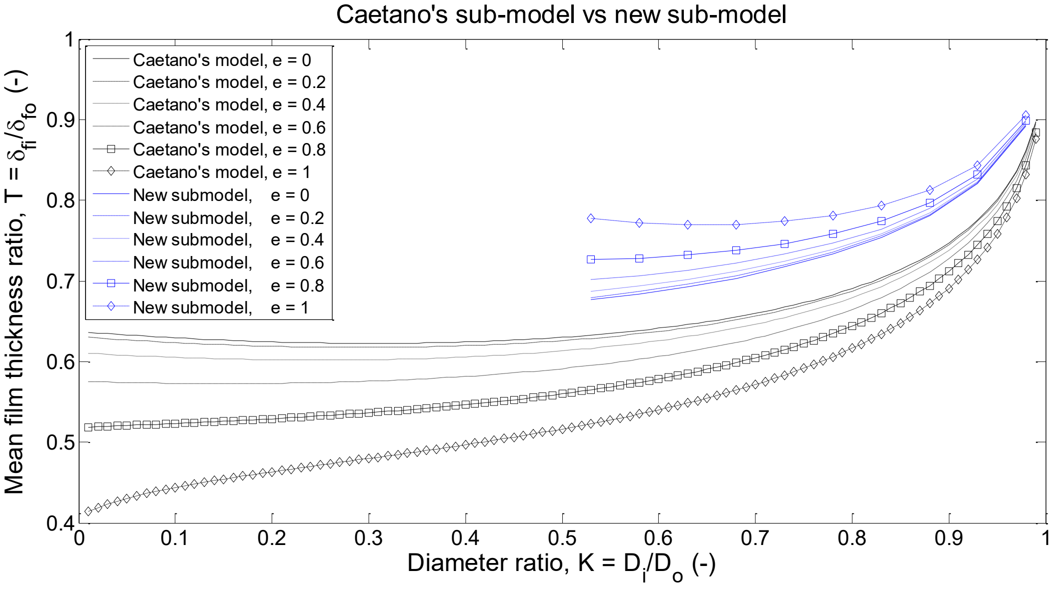

Figure 40: The mean film thickness ratio versus the diameter ratio is derived as a function of the eccentricity. The sub-model for the film thickness ratio as proposed by Caetano et al. is given as black curves. The new sub-model discussed here is shown in blue. Clearly the range and the trend of the film thickness ratio is different in both sub-models.

A different sub-model for the film thickness was also tried as part of the present project. A numerical approach was taken which considered the following points:

- The entrainment is zero.
- The atomisation occurs from both the inner and outer films throughout its circumference. The droplets injected from the films are atomized in all directions within the annulus.
- The atomised droplet is injected ballistically. The path of the droplet is assumed to be in a straight line considering the short distances within the annulus.

- The atomised droplet is deposited ‘immediately’ either on the inner film or on the outer film depending on which pipe lies in its ‘field of view’.
- Atomisation and deposition contribute to the increase and decrease of the film thicknesses respectively, and they occur without any loss of mass.

The new sub-model simulated the atomisation and the deposition and the films. A film thickness ratio of 0.5 was given at the start of the numerical model solver. Each iteration consisted of atomisation from the circumferences of both the films and subsequent deposition and local change of film thicknesses based on the assumptions discussed above. The final relation is independent of the atomisation rate. However, lower rates of atomisation provide better accuracy but can lead to more numerical iterations.

The results of the new model are shown as blue lines in Figure 40. The range of the film thicknesses are far above the ones predicted by Caetano et al. Also, for the predictions by Caetano et al., the film thickness ratio is reduced with increasing eccentricity. However, for the new model, the film thickness ratio increases with eccentricity. The results from the simulations are also summarized in Figure 41. The graphs in that figure show the variation of the film thicknesses, normalized with the thickness for a concentric case, along the circumferences. 0° and 360 ° correspond to the point at the widest gap of the annulus. And 180° corresponds to the point at the narrowest gap. The simulations convey that the films become thicker near this narrowest gap.

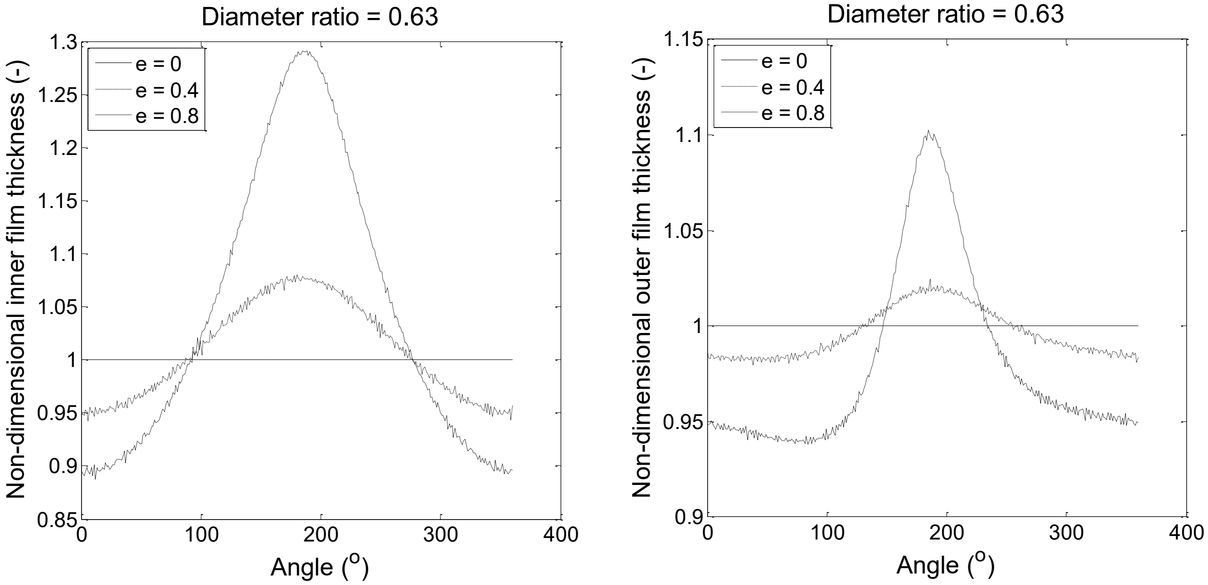

Figure 41: Results from the simulations for the new model. With eccentricity the film thickness becomes thicker near the narrow gap in an annulus.

The main observations of the new film variation sub-model as compared against the sub-model of Caetano et al. [11] are summarized below:

- The mean film thickness ratio, T, predicted by the new sub-model, as a function of diameter ratio, K, and eccentricity, e, is higher than the one obtained from the sub-model of Caetano et al. (Figure 40).

- The mean film thickness ratio, T, predicted by the new sub-model, increases with diameter ratio, K, just like in the sub-model of Caetano et al. (Figure 40).
- The mean film thickness ratio, T, predicted by the new sub-model, increases with eccentricity, e, unlike the sub-model of Caetano et al., which decreases with e (Figure 40).
- The new sub-model predicts a film thickness variation around the circumference as a function of K and e. In general, the film becomes thicker near the narrow edge and becomes thinner near the wide edge creating a sine like ‘wave’ appearance (Figure 41). The wave distribution is sharper for the inner film than for the outer film. The wave also gets sharper with increasing eccentricity.

Appendix B: Secant method

The Newton-Raphson method is the most popular root-finding numerical method for a nonlinear equation $f(x) = 0$ [31]. The algorithm is,

$$x_{n+1} = x_n - \frac{f(x_n)}{f'(x_n)} \tag{23}$$

where x_1 is the first assumed value which should be reasonably close to the expected root. x_1 would give the next closer value to the root x_2, which would give an even closer value x_3, and so on. The iterations can be done until the solution is reached within a pre-defined tolerance.

A drawback of the Newton-Raphson method is the difficulty in finding the derivative of $f(x)$, when the function becomes too complex. This is where the secant method can be handy, in which the derivative is replaced by a (forward) finite-difference equation.

$$x_{n+1} = x_n - f(x_n)\frac{(x_n - x_{n-1})}{f(x_n) - f(x_{n-1})} \tag{24}$$

In relation to Appendix B: Secant method the secant method can be described as:

If $f\left(\delta_{fo/i}\right) = U_{SL}$,

$$\delta_{fo/i_{n+1}} = \delta_{fo/i_n} - \left[f\left(\delta_{fo/i_n}\right) - U_{SL}\right]\frac{\delta_{fo/i_n} - \delta_{fo/i_{n-1}}}{f\left(\delta_{fo/i_n}\right) - f\left(\delta_{fo/i_{n-1}}\right)} \tag{25}$$

where $f\left(\delta_{fo/i_n}\right)$ is $U_{SL,o/i\_model}$ in Figure 57.

Appendix C: Holdup versus gas velocity

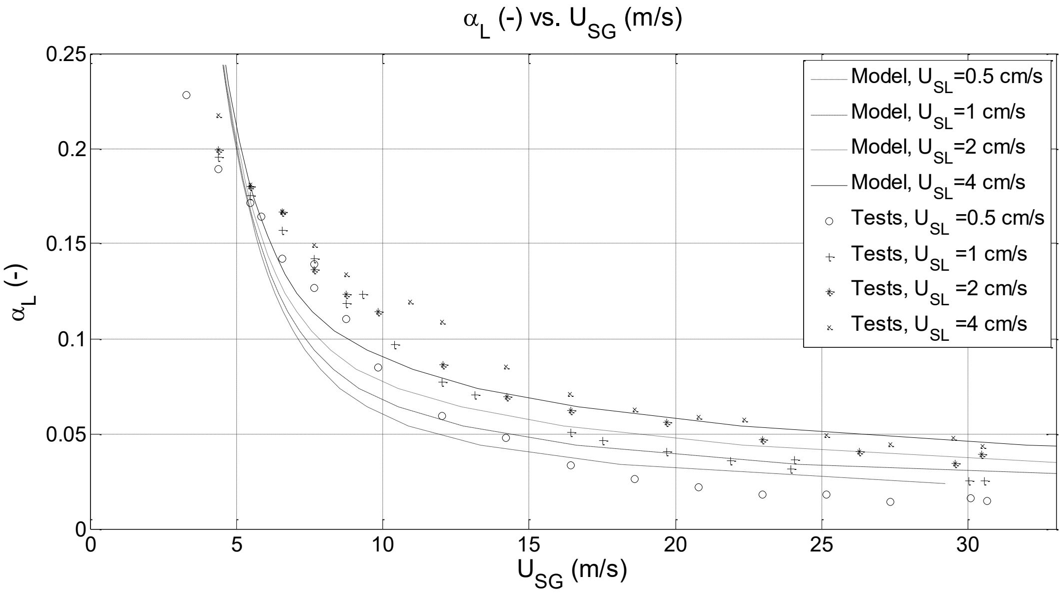

Figure 42: Holdup versus superficial gas velocity for different superficial liquid velocities.

Appendix D: Modified Wallis cor.

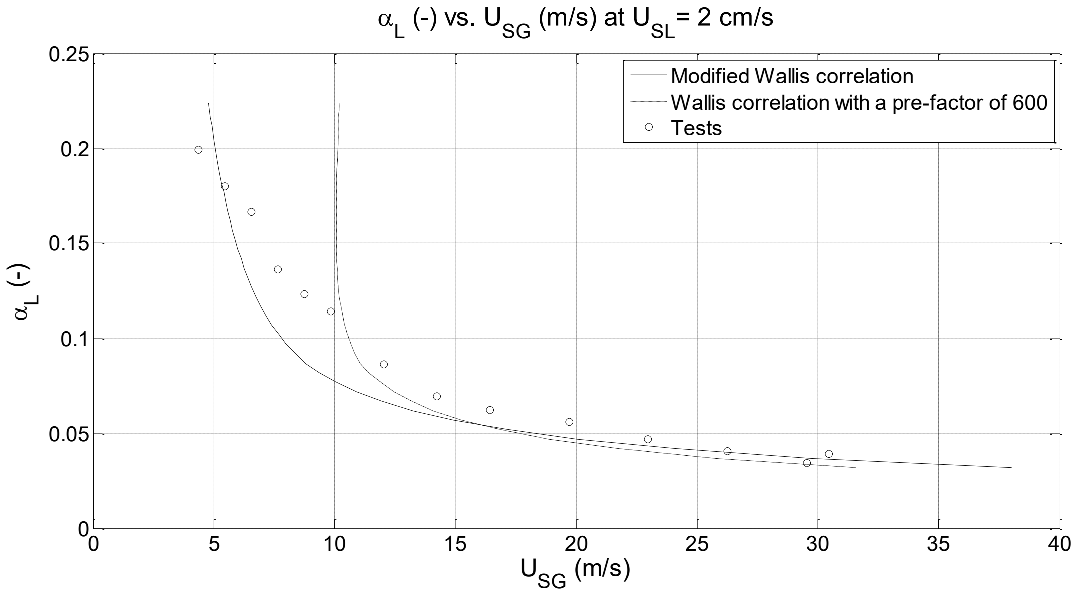

Figure 43: Holdup versus superficial gas velocity for different interfacial friction factors. The Wallis correlation responds sharply near the churn regime. The modified Wallis correlation gives a better match with the experimental results.

Figure 44 compares the Wallis correlation with a pre-factor of 600 (eq. (17)) and the modified Wallis correlation (eq. (18)). On the left of the minima, i.e. near the churn regime, the pressure gradient increases sharply with an increasing superficial gas velocity for eq. (17). Therefore, to

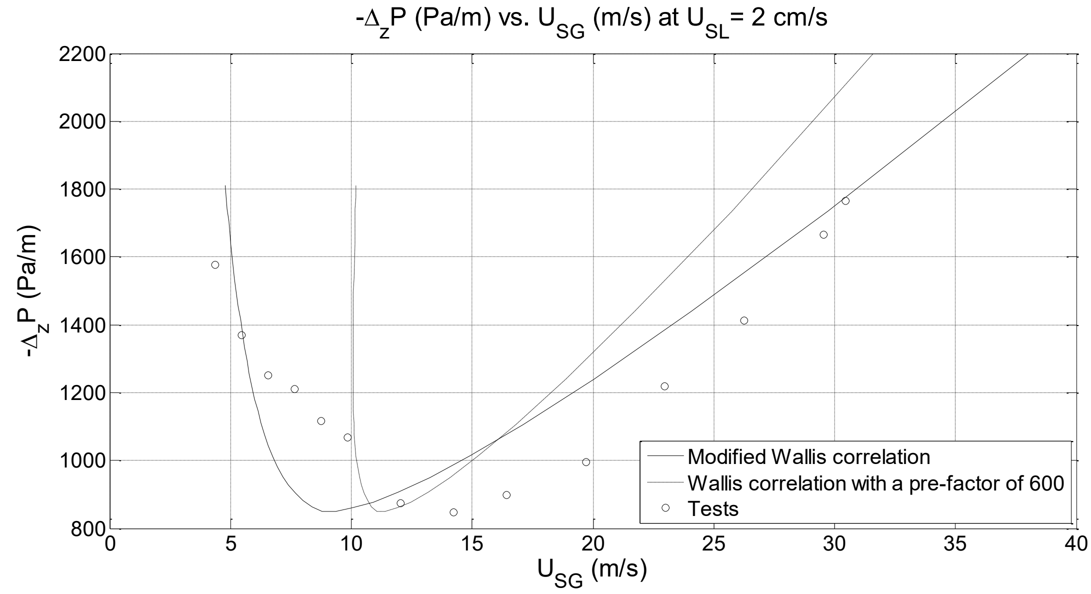

Figure 44: Pressure gradient versus the superficial gas velocity for different interfacial friction factors. The Wallis correlation responds sharply on the left side of the minima. The modified Wallis correlation gives a better match with the experimental results.

suit the experiments better, eq. (18) was used throughout this report, unless mentioned otherwise. Figure 43 confirms the effectiveness of the modified Wallis correlation.

Appendix E: Film distribution

The film distribution at a superficial gas velocity of 14 m/s is shown in Figure 45 and in Figure 46. Since mixing between the films is accelerated at lower gas velocities a ‘plateau’ is expected in the graphs, as the initial liquid distribution is lost due to mixing, instead of a ‘trend’ or a ‘curve’ for high gas velocities (Figure 27 and Figure 28). For comparison, the results at a superficial gas velocity of 21 m/s are shown in Figure 47 and Figure 48.

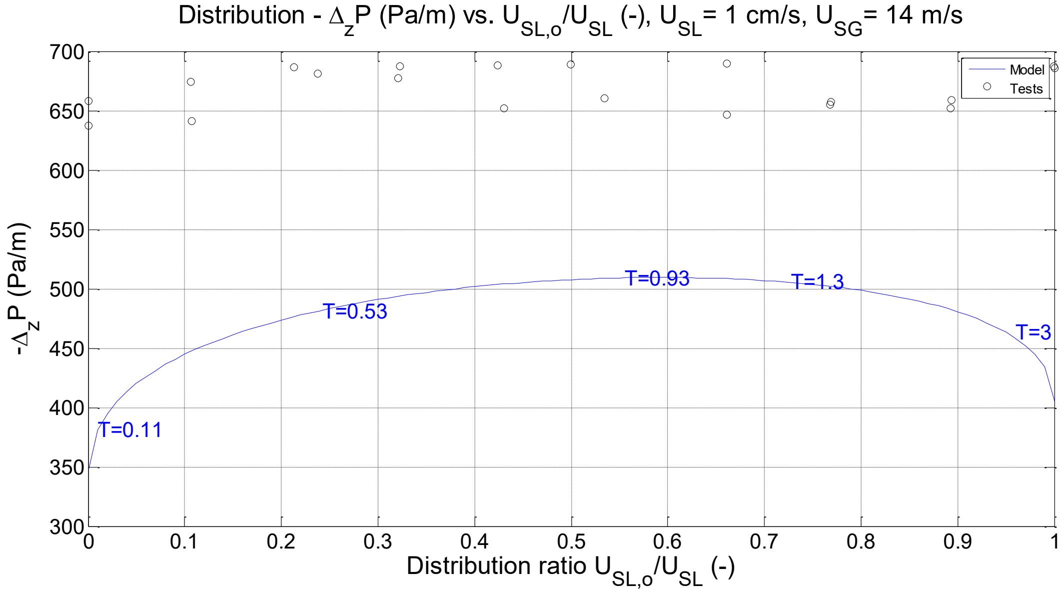

Figure 45: Pressure gradient versus the distribution ratio for the model predictions and for the experiments, at $U_{SL} = 1\ cm/s$ and $U_{SG} = 14\ m/s$.

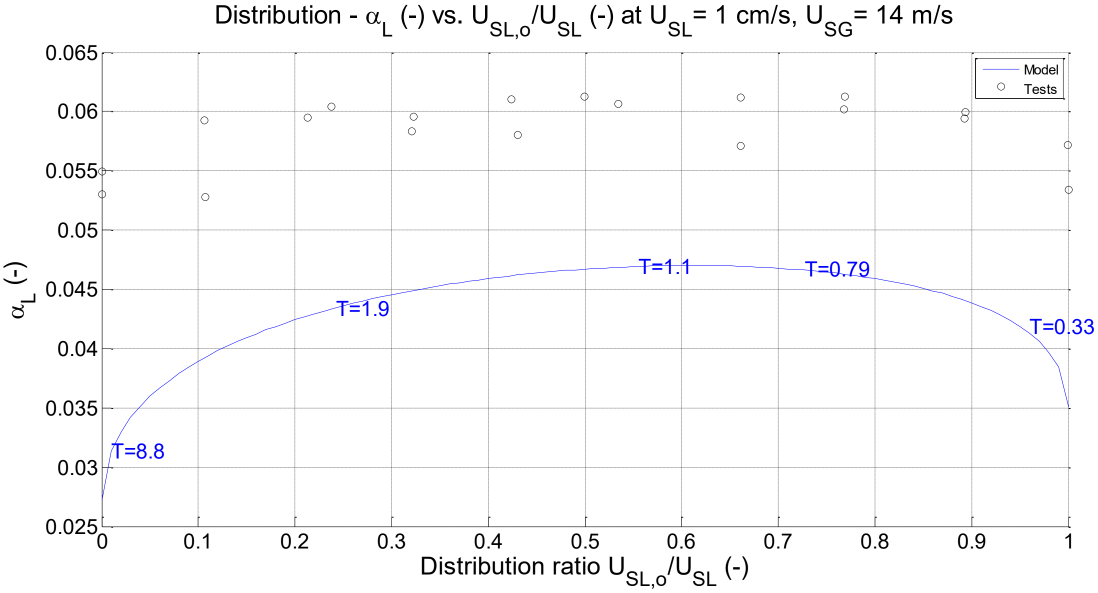

Figure 46: Holdup versus the distribution ratio for the model predictions and for the experiments, at $U_{SL} = 1\ cm/s$ and $U_{SG} = 14\ m/s$.

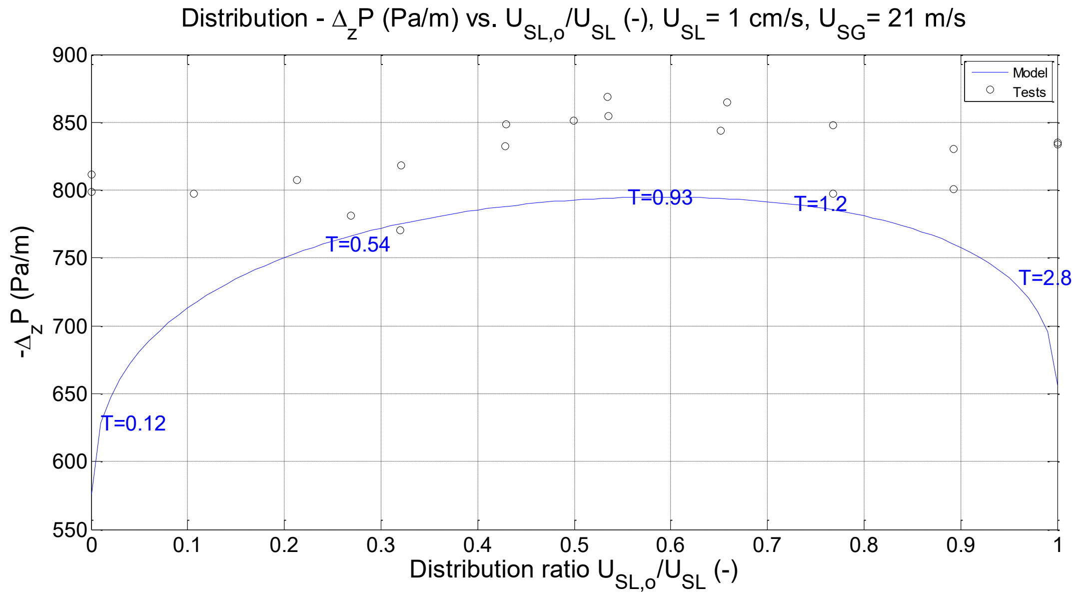

Figure 47: Pressure gradient versus the distribution ratio for the model predictions and for the experiments, at $U_{SL} = 1\ cm/s$ and $U_{SG} = 21\ m/s$.

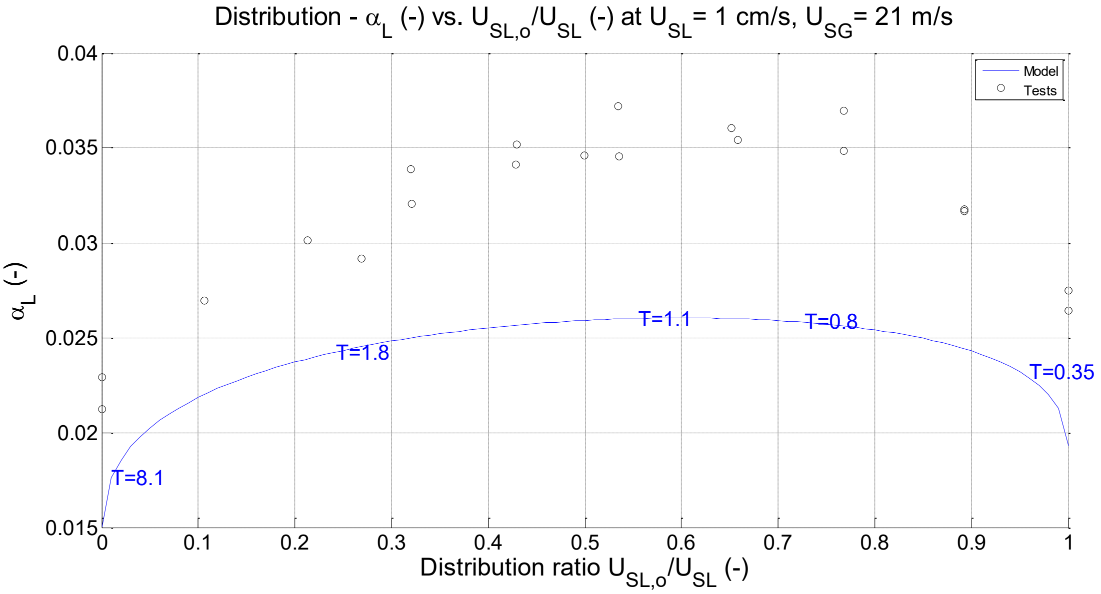

Figure 48: Holdup versus the distribution ratio for the model predictions and for the experiments, at $U_{SL} = 1\ cm/s$ and $U_{SG} = 21\ m/s$.

Appendix F: Fully eccentric flows

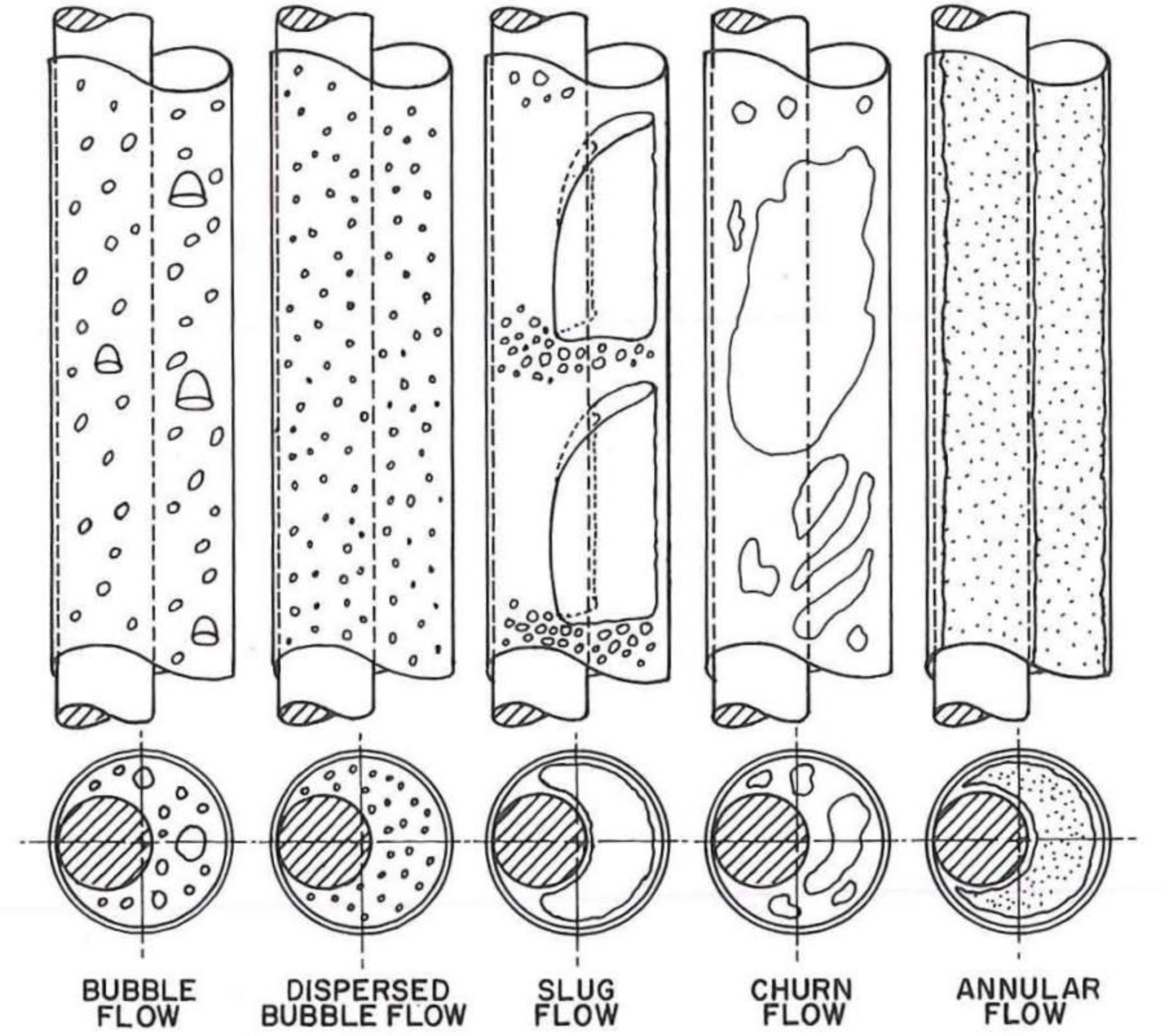

Figure 49: Flow patterns in upward vertical flow through a fully eccentric annulus [7].

Appendix G: Modelling of pipe flow

The objective of this project is to understand certain regimes of the multiphase flow in a vertical annulus. However, in this appendix the modelling of annular flow in a circular pipe will be explained, as a precursor to obtain a better understanding of the modelling of gas-liquid annular flows in annuli.

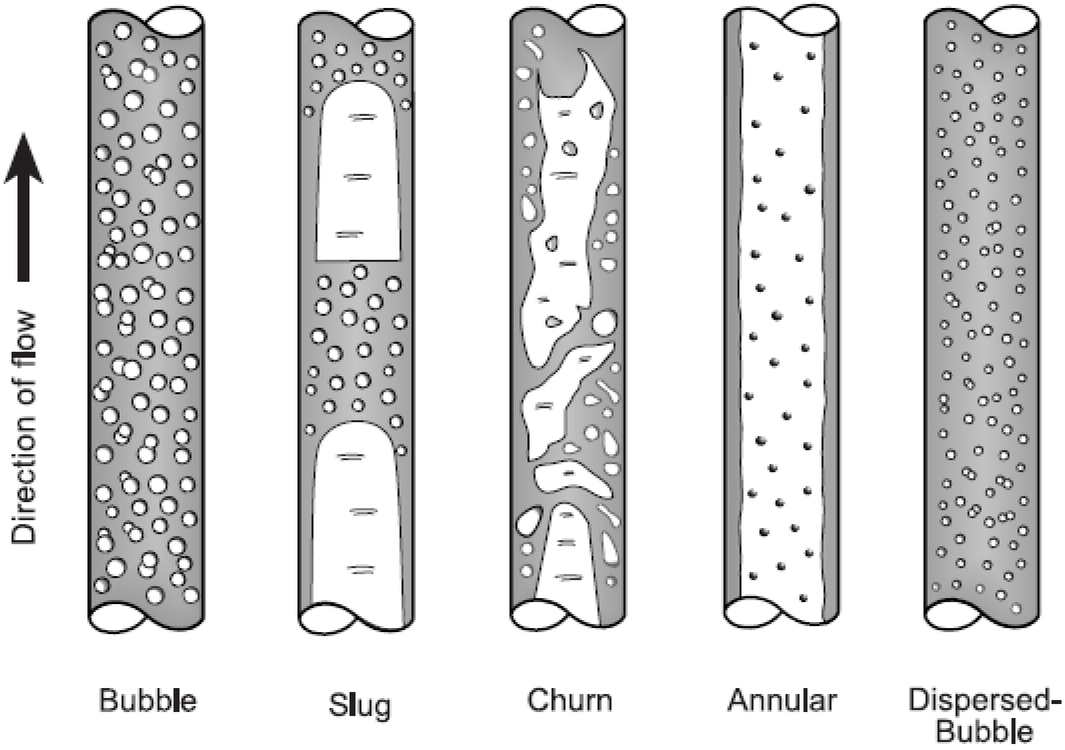

Figure 50: Flow regimes in a pipe. The second from the right is the annular flow pattern which happens at the highest gas velocities. [33]

Figure 50 shows the various flow patterns which can occur in a cylindrical pipe. The annular flow, which is going to be modelled here, is characterized by an annular liquid film which moves up along with the gas. The gas core is shown on the right side in Figure 52. A momentum balance for the gas core can be considered, which includes the pressure, gravity and interfacial shear stresses. The control volume is bounded by the two film surfaces within a differential element dz.

$$-\tau_i dz \times S_i + (-dP) \times A_c - \rho_G g dz \times A_c = 0$$

In which the interfacial perimeter is $S_i = \pi(D - \delta_f)$ and the core area is $A_c = \frac{\pi}{4}(D - \delta_f)^2$.

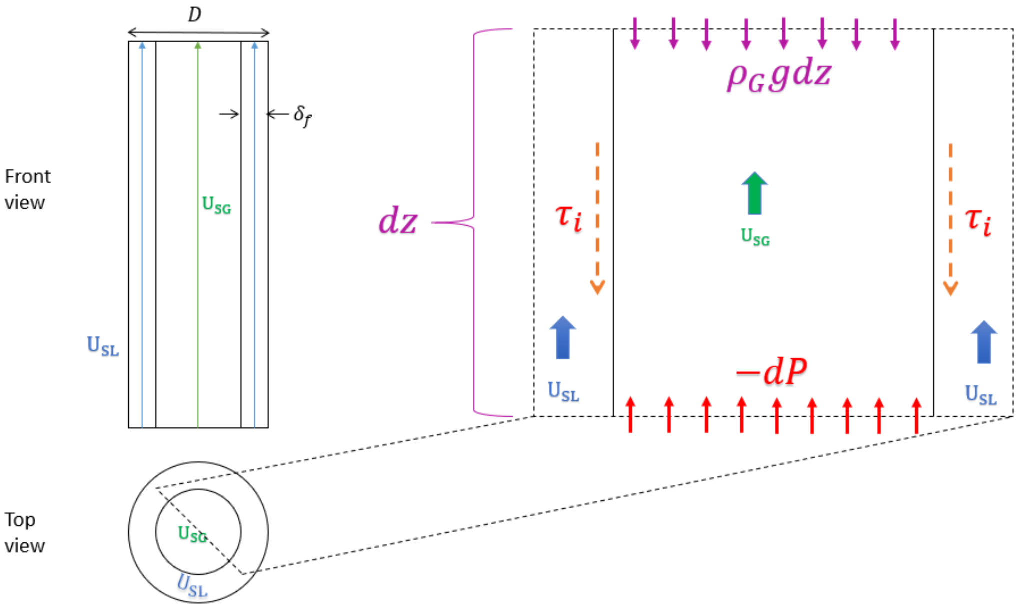

Figure 52: The location of the gas core and the forces acting on it. A momentum balance on the core is derived, which includes the pressure, gravity and interfacial shear stress.

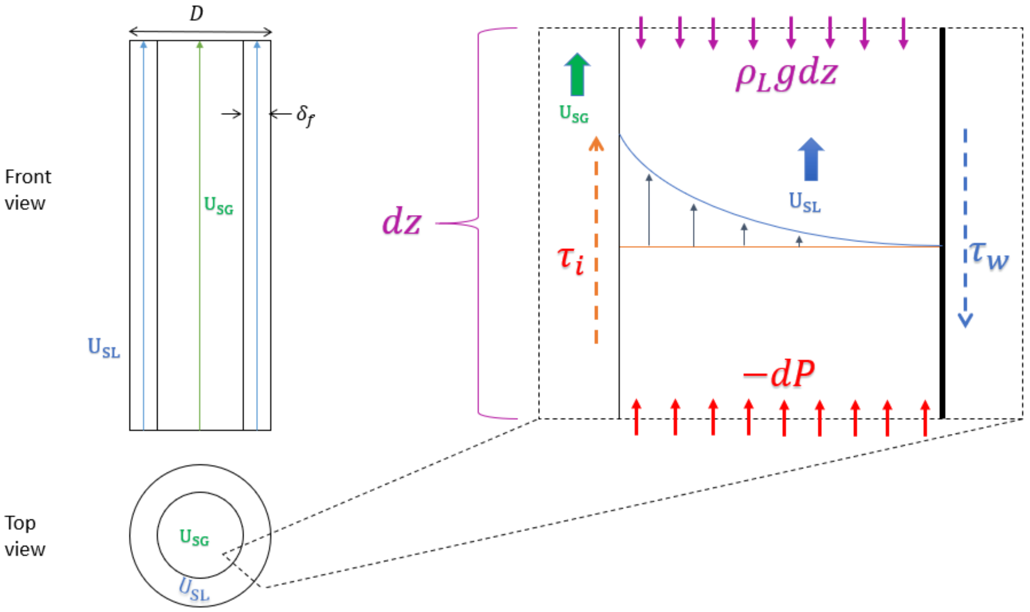

Figure 51: The location of the liquid film and the forces acting on it. A momentum balance on the film is derived, which includes the pressure, gravity, interfacial and wall shear stresses.

The interfacial shear stress is given by:

$$\tau_i = \frac{\left(\left[-\frac{dP}{dz}\right] - \rho_G g\right) A_c}{S_i} \tag{26}$$

The liquid film is shown on the right side in Figure 51. A momentum balance for the film is derived, which includes the pressure, gravity, interfacial and wall shear stresses. The control volume is bounded by the film surface and by the wall surface within a differential element dz.

$$\tau_i dz \times S_i - \tau_w dz \times S_w + (-dP) \times A_f - \rho_L g dz \times A_f = 0$$

In which the wall perimeter is $S_w = \pi D$ and the film area is $A_f = \frac{\pi}{4}[D^2 - (D - \delta_f)^2]$.

The wall shear stress is given by

$$\tau_w = \frac{\left[\left(\left[-\frac{dP}{dz}\right] - \rho_L g\right) A_f + \tau_i S_i\right]}{S_w} \tag{27}$$

The shear stress can be derived for any point at a distance y from the wall in a similar way.

$$\tau_y = \frac{\left[\left(\left[-\frac{dP}{dz}\right] - \rho_L g\right) A_y + \tau_i S_i\right]}{S_y} \tag{28}$$

where the variables with the subscript y correspond to the variables given in eq. (27).

Now since the shear stress at each point is known, the velocity gradient can also be given at each point within the film as specified below, using Newton's law of viscosity,

$$\frac{du}{dy} = \frac{\tau_y}{\mu_{eff}} \tag{29}$$

It is worthwhile to note that in eq. (29) we have the effective viscosity $\mu_{eff} = \mu_L$, assuming a laminar flow within the films [13]. With appropriate boundary conditions the velocity distribution can be calculated and hence the superficial liquid velocity, U_{SL} at a given pressure gradient, $\left[-\frac{dP}{dz}\right]$, and the holdup, α_L which is a function of film thickness, δ_f.

The part of the modelling so far, which will be referred to as the **Liquid sub-model**, can be summarized as below:

$$\left[-\frac{dP}{dz}\right] = f_1(U_{SL}, \alpha_L) \tag{30}$$

The superficial gas velocity, U_{SG}, can be derived and expressed in terms of $\left[-\frac{dP}{dz}\right]$ as follows:

$$\left[-\frac{dP}{dz}\right] = 4 f_i \frac{\frac{1}{2}\rho_G U_{SG}^2}{D_h}$$

$$U_{SG} = \sqrt{\frac{\left[-\frac{dP}{dz}\right] D_h}{4 f_i \frac{1}{2}\rho_G}} \tag{31}$$

Where D_h is the hydraulic diameter, which is equal to D for a pipe, f_i is the interfacial friction factor for which many correlations are available, which will be discussed in the modelling for annuli (sec. 6.6.2), and f_i is a function of the film thickness, δ_f, and of the diameter D_h.

Eq. (31) can now be summarized as follows, and is referred to as the **Gas sub-model:**

$$\left[-\frac{dP}{dz}\right] = f_2(\alpha_\mathrm{L}, U_{SG}) \tag{32}$$

In essence, the pressure gradient can be calculated if the superficial gas (**Gas sub-model**) or liquid (**Liquid sub-model**) velocity is given along with the holdup. The **Liquid sub-model** gives the pressure gradient at a specified U_{SL} and α_L. The **Gas sub-model** can provide U_{SG} at the then calculated pressure gradient and α_L. Therefore, the **Liquid sub-model** and the **Gas sub-model** can be combined to the **Full Model**:

$$\left[-\frac{dP}{dz}\right] = f_3(U_{SL}, \alpha_\mathrm{L}, U_{SG}) \tag{33}$$

The modelling for annuli (sec. 6) is just an extension of the modelling for the pipe. Table 4 summarizes the comparison between the two models.

Table 4: Summary of sub-models used for a pipe and an annulus. An additional closure is required for the annulus for the film thickness ratio between the inner and outer films.

	Pipe	**Annulus**
Liquid sub-model	$\left[-\frac{dP}{dz}\right] = f_1(U_{SL}, \alpha_\mathrm{L})$	$\left[-\frac{dP}{dz}\right] = f_1(U_{SL,o}, U_{SL,i}, \alpha_\mathrm{L,o}, \alpha_\mathrm{L,i})$
Gas sub-model	$\left[-\frac{dP}{dz}\right] = f_2(\alpha_\mathrm{L}, U_{SG})$	$\left[-\frac{dP}{dz}\right] = f_2(\alpha_\mathrm{L,o}, \alpha_\mathrm{L,i}, U_{SG})$
Full model	$\left[-\frac{dP}{dz}\right] = f_3(U_{SL}, \alpha_\mathrm{L}, U_{SG})$	$\left[-\frac{dP}{dz}\right] = f_3(U_{SL,o}, U_{SL,i}, \alpha_\mathrm{L,o}, \alpha_\mathrm{L,i}, U_{SG})$
Turbulence/laminar sub-model	Yes	Yes
Interfacial friction factor	Yes	Yes
Other closures	No	Film thickness ratio - T (sec. 6.5)

Appendix H: Force balance for annulus

The different shear stresses acting on the liquid films are shown in Figure 53.

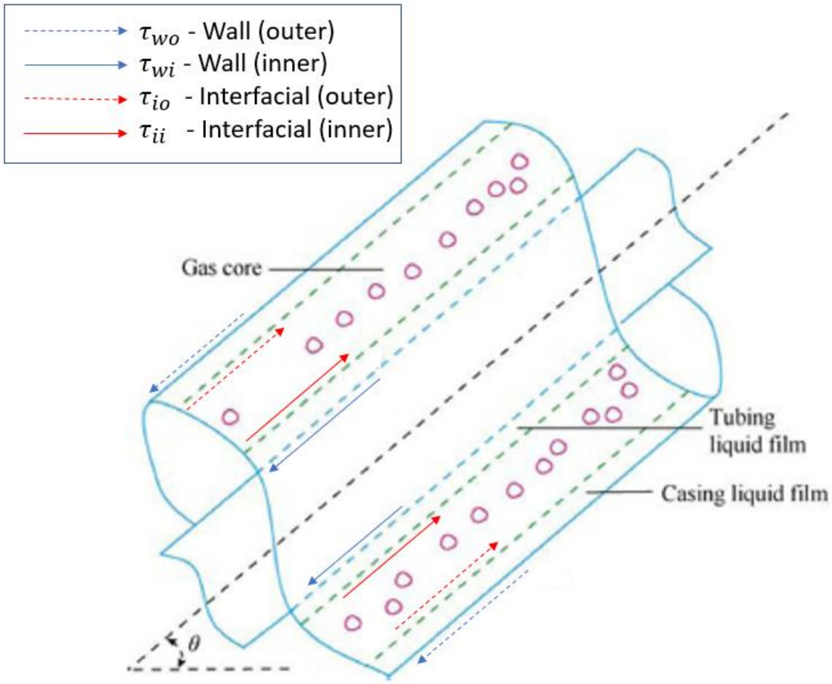

Figure 53: Shear stresses on the liquid films in an annular flow [22]. *For some flow conditions the wall shear stress can also be directed in the direction of the flow, and this is visible in Figure 22.*

A second model parameter, K_0, is defined as

$$K_0 = \frac{\tau_{io}}{\tau_{ii}} \tag{34}$$

The interfacial shears are given by,

$$\tau_{io/i} = f_{io/i}\frac{1}{2}\rho_G\left(U_G - u_{io/i}\right)^2 \tag{35}$$

where, U_G is the gas velocity, which can be expressed as $U_G = U_{SG}\frac{A}{A_c}$, and $u_{io/i}$ is the interfacial liquid velocity. Furthermore, the interfacial friction factor can be expressed as

$$f_{io/i} = I f_{SG} \tag{36}$$

In which the dimensionless interfacial friction factor parameter I requires a closure (sec. 6.6.2). The superficial gas-phase friction factor is calculated by using the Blasius equation:

$$f_{SG} = 0.0791 Re_{SG}^{-0.25} = 0.0791\left(\frac{\rho_G U_{SG} D_h}{\mu_G}\right)^{-0.25} \tag{37}$$

In which the hydraulic diameter can be expressed as $D_h = D_o - D_i$ for an annulus.

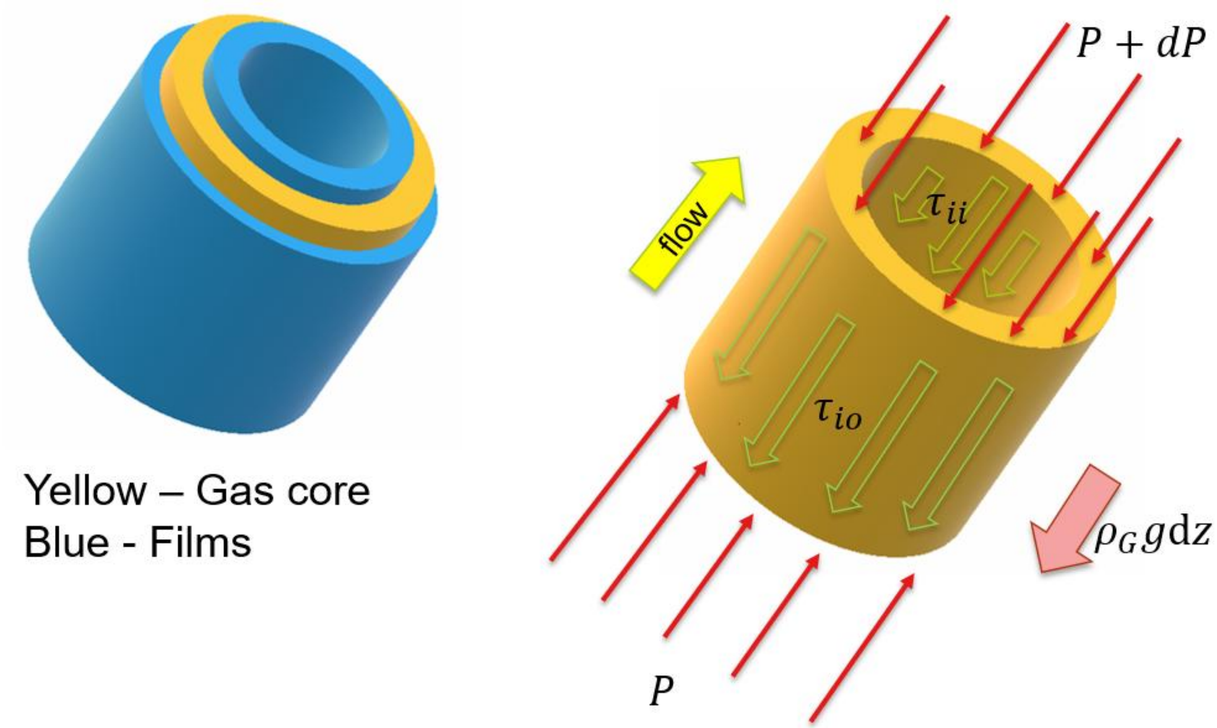

Figure 54: The gas core force balance is depicted in the right graph. The arrow shows the direction of the forces. In the left graph the blue concentric cylinders represent the liquid films and the yellow concentric cylinder represents the gas core.

Eq. (34) can be rewritten as

$$K_0 = \frac{\tau_{io}}{\tau_{ii}}$$

$$K_0 = \frac{f_{io}\frac{1}{2}\rho_G U_G^2}{f_{ii}\frac{1}{2}\rho_G U_G^2}$$

$$K_0 \sim \frac{f_{io}}{f_{ii}} \tag{38}$$

The shear stresses acting on the system can be derived using the force balances for the films and the gas core. From the gas core force balance (Figure 54) and the model parameter, K_0 (34), the interfacial shear stress on the inner pipe can be derived as

$$PA_c - (P + dP)A_c - \tau_{ii}S_{ii}dz - \tau_{io}S_{io}dz - \rho_G g A_c dz = 0$$

$$-\frac{dP}{dz}A_c - \tau_{ii}S_{ii} - \tau_{io}S_{io} - \rho_G g A_c = 0$$

$$\tau_{ii} = \frac{\left(\left[-\frac{dP}{dz}\right] - \rho_G g\right)A_c}{\mathrm{K}_0 S_{io} + S_{ii}} \tag{39}$$

And for the interfacial shear stress for the outer pipe we have

$$\tau_{\mathrm{io}} = \mathrm{K}_0 \tau_{ii} \tag{40}$$

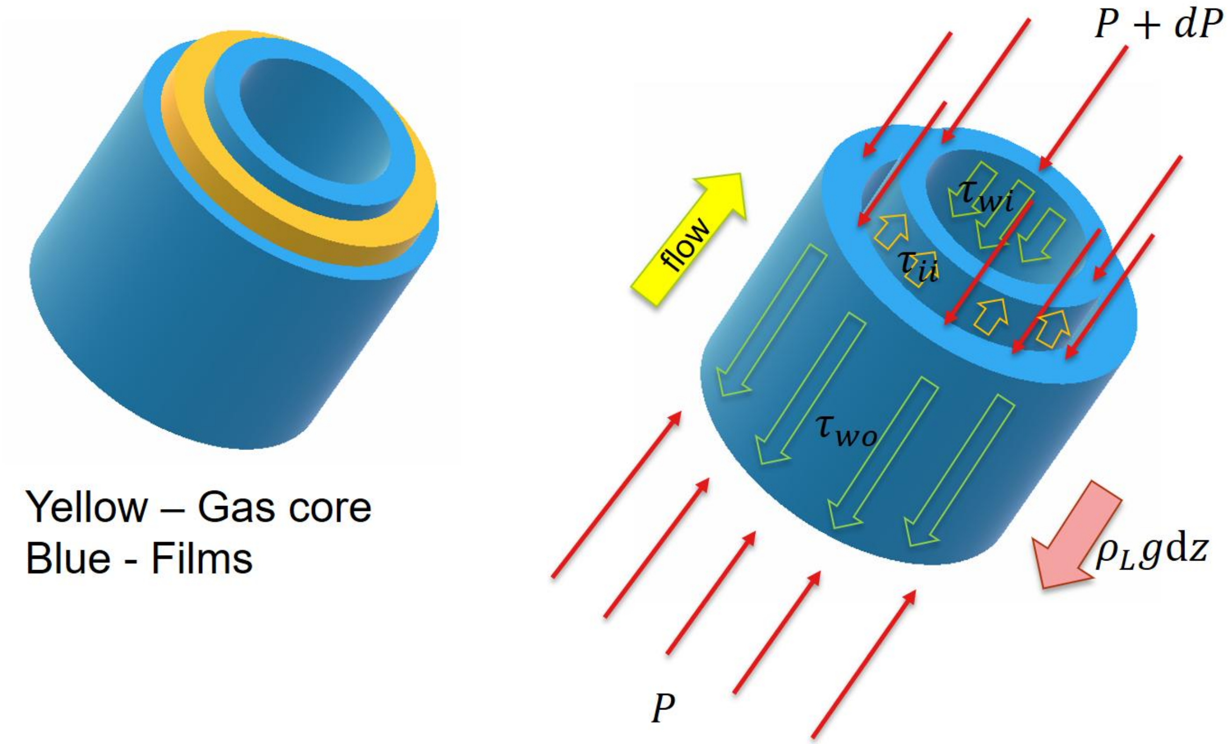

Figure 55: The force balance for the liquid films is depicted in the right graph. The arrow shows the direction of the forces. In the left graph the blue concentric cylinders represent the liquid films and the yellow concentric cylinder represents the gas core.

Consider now the outer film (Figure 55) with a differential height of dz:

$$P A_{fo} - (P + dP) A_{fo} - \tau_{wo} S_{wo} dz + \tau_{io} S_{io} dz - \rho_L g A_{fo} dz = 0$$

$$-\frac{dP}{dz} A_{fo} - \tau_{wo} S_{wo} + \tau_{io} S_{io} - \rho_L g A_{fo} = 0$$

$$\tau_{wo} = \frac{\left(\left[-\frac{dP}{dz}\right] - \rho_L g\right) A_{fo} + \tau_{io} S_{io}}{S_{wo}} \tag{41}$$

In which τ_{wo} is wall shear stress on the outer film. Similarly, for the inner film we have

$$\tau_{wi} = \frac{\left[\left(\left[-\frac{dP}{dz}\right] - \rho_L g\right) A_{fi} + \tau_{ii} S_{ii}\right]}{S_{wi}} \tag{42}$$

In which τ_{wi} is wall shear stress on the inner film.

The shear stress at any point (Figure 56) within the film can be calculated in the same way as has been done for the wall shear stresses. The *TNO report* describes this as follows [24]:

> *"The equations used to compute τ_{wi} and τ_{wo} can be adapted to calculate the shear stress in the liquid film at any distance y from the wall, τ_{yi} and τ_{yo}, when A_{fi}, A_{fo}, S_{wi} and S_{wo} are replaced by A_{yi}, A_{yo}, S_{yi} and S_{yo}"*

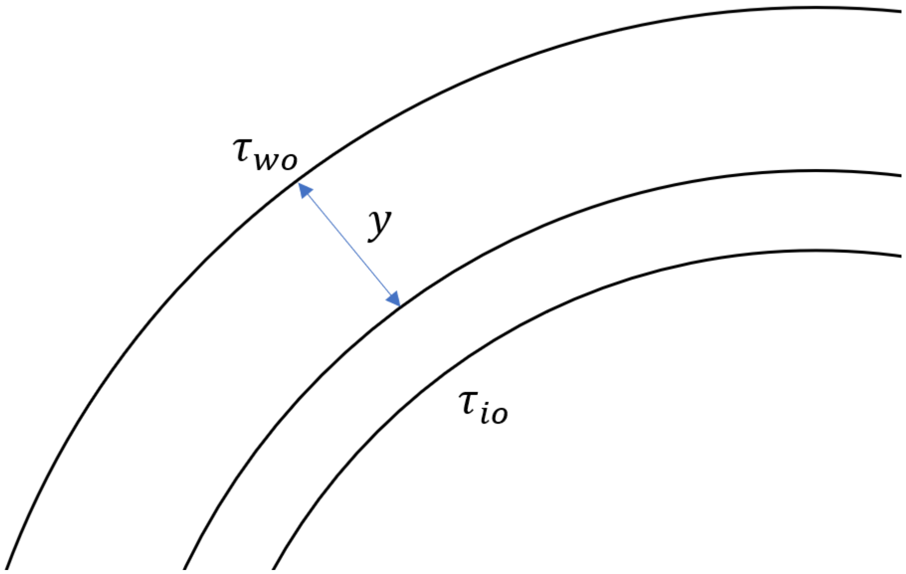

Figure 56: The shear stresses are calculated at a distance y from the wall. In the figure the outer film is depicted.

At a distance y from the wall for the outer film we have:

$$D_{yo} = D_o - 2y \tag{43}$$

$$S_{yo} = \pi D_{yo} \tag{44}$$

$$A_{yo} = \frac{\pi}{4}[\left(D_o - 2\delta_{fo}\right)^2 - D_{yo}] \tag{45}$$

Similarly, at a distance y from the wall for the inner film we have:

$$D_{yi} = D_i + 2y \tag{46}$$

$$S_{yi} = \pi D_{yi} \tag{47}$$

$$A_{yi} = \frac{\pi}{4}[\left(D_o + 2\delta_{fi}\right)^2 - D_{yi}] \tag{48}$$

Appendix I: Flow chart/programming

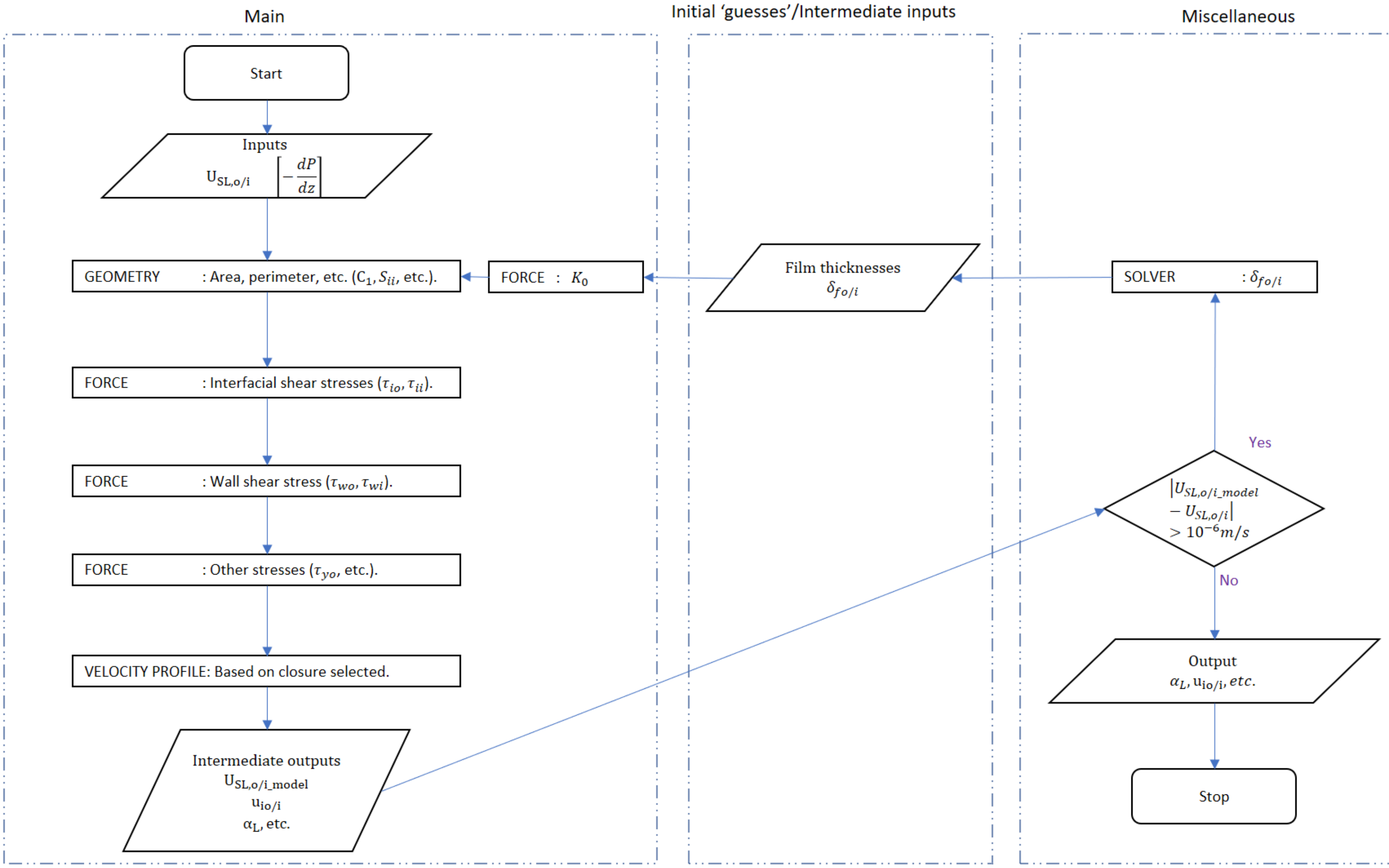

Figure 57: Flowchart for the model. The desired outputs for a set of inputs are generated through an iterative procedure.

The sequence of the liquid sub-modelling is explained in Figure 57.

Main: The program starts with the liquid throughputs and pressure gradient as inputs (sec. 6.4). The GEOMETRY (sec. 6.5), FORCE (Appendix H: Force balance for annulus) and VELOCITY PROFILE (sec. 6.6.1) is then calculated to provide the output (initial/intermediate).

Initial and intermediate inputs: The GEOMETRY requires film thicknesses ($\delta_{fo/i}$) as inputs. However, one of the aims of the modelling is to calculate the thicknesses, as an output, for the given inputs. For such a situation an initial value or a reasonable guess for the thicknesses can be assumed and a corresponding $U_{SLo/i,model}$ could be calculated. To match the $U_{SLo/i,model}$ closer to the $U_{SLo/i}$ the thicknesses are better 'guessed' with the help of a solver. Such better 'guesses' are fed as intermediate inputs again to the program until $U_{SLo/i,model}$ becomes close enough to $U_{SLo/i}$. The solver used is the Secant method, which has been explained in Appendix B: Secant method.